OFDM COMMUNICATIONS OVER PEAK-LIMITED CHANNELS

A Thesis
Presented to
The Academic Faculty

by

Robert J. Baxley

In Partial Fulfillment
of the Requirements for the Degree
Doctor of Philosophy in the
School of Electrical & Computer Engineering

Georgia Institute of Technology
August 2008

OFDM COMMUNICATIONS OVER PEAK-LIMITED CHANNELS

Approved by:

Professor G. Tong Zhou, Advisor
School of Electrical & Computer
Engineering
Georgia Institute of Technology

Professor J. Stevenson Kenney
School of Electrical & Computer
Engineering
Georgia Institute of Technology

Professor Xiaoli Ma
School of Electrical & Computer
Engineering
Georgia Institute of Technology

Professor Ye (Geoffrey) Li
School of Electrical & Computer
Engineering
Georgia Institute of Technology

Professor Ellis Johnson
School of Industrial & Systems
Engineering
Georgia Institute of Technology

Date Approved:

To my mom and dad.

ACKNOWLEDGEMENTS

I would like to express my sincerest thanks to my advisor Professor Tong Zhou for her complete support and guidance. Throughout my graduate career she has continuously supported my research and been available at any time to discuss our collaborations. I consider myself extremely lucky to be one of her students.

I would also like to thank my committee members, Professor J. Stevenson Kenney, Professor Xiaoli Ma, Professor Ye (Geoffrey) Li and Professor Ellis Johnson for serving on my committee and for helping to improve my dissertation with their thoughtful critiques my work. Additionally, I would like to thank my group members, Dr. Lei Ding, Dr. Raviv Raich, Dr. Ning Chen, Dr. Hua Qian, Dr. Chunpeng Xiao, Dr. Chunming Zhao, Vince Emanuele, Thao Tran, Qijia Liu and Kun Shi, who have provided not only fruitful research perspectives but, more importantly, their support and friendship. I also want to thank John Kleider for his collaborations and for introducing me to new and interesting topics.

Finally, I want thank my family and friends for their unconditional love and support.

TABLE OF CONTENTS

LIST OF TABLES

LIST OF FIGURES

SUMMARY

Orthogonal frequency division multiplexing (OFDM) has become a popular modulation method in high-speed wireless communications. By partitioning a wideband fading channel into flat narrowband channels, OFDM is able to mitigate the detrimental effects of multipath fading using a simple one-tap equalizer. However, in the time domain OFDM signals suffer from large envelope variations, which are often characterized by the peak-to-average ratio (PAR). High PAR signals, like OFDM, require that transmission amplifiers operate at very low power efficiencies to avoid clipping.

In this dissertation, we explore the problems associated with transmitted OFDM signals through peak limited channels. A large part of this work deals with analyzing different distortion metrics and determining which metrics are most useful. We find that the signal-to-noise-plus-distortion ratio (SNDR) is one of the most important metrics in assessing distortion in nonlinear channels. As part of this analysis, we compare sample-based SNDR and symbol-based SNDR and find that using the more comprehensive symbol-based metric as the objective in SNDR maximization algorithms leads to only marginal SNDR improvements.

The SNDR perspective is also applied to existing PAR-reduction techniques to compare existing schemes and proposed new schemes. Part of this work involves deriving a SNDR maximizing adaptation of the popular PAR-reduction scheme, selected mapping (SLM). We also compare another popular PAR-reduction method, partial transmit sequence (PTS), to SLM through a variety of metrics including SNDR and found that for any given amount of complexity or side information SLM provided better performance.

The next major piece of work in this dissertation addresses synchronization and channel estimation in peak-limited channels for OFDM. We build off of existing work that shows that embedded synchronization energy is a more bandwidth efficient means of synchronization than preamble-base methods. With this, we demonstrate a method for generating embedded

sequences that have low PAR, and thus minimize the PAR of the combination OFDM symbol/embedded sequence among all embedded sequences. Next, we extend this work to sequences called joint synchronization-pilot sequences (JSPSs) by deriving the symbol-estimate mean squared error (MSE) pilot placements for the JSPSs and by showing how the JSPSs can be used with SLM for blind detection.

Finally, the dissertation concludes with a derivation of the SNDR-optimal transmitter/receiver pairs. Using functional analysis, we show that the SNDR-optimal receivers for peak-limited transmitters are not linear. Instead they follow non-linear functions that depend on the noise and signal distributions.

CHAPTER I

OFDM, PEAK-LIMITED CHANNELS AND PAR REDUCTION

1.1 Introduction

High-speed wireless communications are becoming an integral part of our society. Once exotic applications such as internet browsing and streaming video on mobile handsets are becoming the standard. A plethora of signal processing and engineering breakthroughs made this evolution possible including advanced error control coding techniques, fast micro processors and long-lasting batteries.

Increasingly the modulation format of choice in next-generation wireless communications systems is orthogonal frequency division multiplexing (OFDM). OFDM possesses several main advantages over the alternatives. The most prominent advantage of OFDM is that it is a block-based transmission scheme, which allows for a simple channel equalization structure. Single carrier transmission systems that transmit a constant stream of data require very complicated channel equalization structures to correct multipath channel effects. These single carrier equalizers are essentially constantly updated infinite-impulse response filters, which are relatively complex to implement. Conversely, because OFDM is transmitted in self-contained blocks that are preceding by a guard-prefix, OFDM equalization can be achieved with a simple multiplication operation for each subcarrier.

Said another way, OFDM transforms large-bandwidth multipath fading channels into multiple orthogonal narrow-bandwidth flat fading channels. In addition to low-complexity equalization, this channel separation also allows for frequency-domain bit loading and simple orthogonal user allocation.

Despite these promising features, OFDM is not immune to synchronization issues that can plague any communications system, namely carrier frequency offsets and timing offsets. However, there is a rich body of research that describes schemes for resolving these issues. In addition to these impediments, OFDM also presents an additional draw back that is not

present in single-carrier communications system: a large time-domain signal dynamic range. That is, OFDM symbols in the time domain possess large power fluctuations over each symbol period. These symbol fluctuations are difficult for transmitting power amplifiers (PAs) to accommodate. The result is that OFDM systems operate at very low power efficiencies.

The power envelope fluctuations in OFDM signals are often quantified by the peak-to-average power ratio (PAR). The PAR of the signal entering the PA is an important metric because there is a one-to-one relationship between the moments of the PAR distribution and the PA power efficiency. The precise relationship depends on the type of PA, but the relationships are well-known and can be analytically derived. Also, most physical PAs do not exhibit a soft-limiter characteristic. Instead, it is common for a PA to exhibit a gradual compression characteristic even in the "linear" region where large inputs have less gain than smaller inputs. The PAR is not a sufficient metric to quantify the distortion effect of the this compression PA characteristic. However, if predistortion techniques, which have been thoroughly studied in the literature, are applied, then it is possible to realize the ideal soft-limiting characteristic in the concatenated predistortion/PA system. Thus, for the following discussion it is assumed that predistortion is used and that the peak-limiting characteristic is an ideal soft limiter. In this case, the PAR is sufficient to characterize all of the effects of the concatenated predistortion/PA system.

Thus, it seems straightforward that the problem of transmitting OFDM over peak-limited (e.g. PA) channels, is one of simply reducing the PAR. However, it is not possible to reduce the PAR of a signal without sacrificing something else. The "something else" can be a reduction in the data rate, an increase in constellation distortion, or a receiver modification and almost always includes a significant increase in complexity. Thus, despite its ubiquity and its straightforward relationship to the power efficiency, the PAR should not be the only metric considered when examining system performance of an OFDM system in peak-limited channels. However, PAR is one very important piece of the equation. In the following, we refer to any scheme that attempts to mitigate the detrimental effects of peak-limited channels as a *PAR-reduction* scheme.

Other metrics by which a PAR-reduction scheme can be measured include the signal-to-noise-plus-distortion ratio (SNDR), the capacity, the complexity, and the out-of-band distortion. The SNDR takes into account any distortion that results from PAR reduction and it also takes into account the PAR itself. Furthermore, when the SNDR is measured in the in-band frequencies, there is a one-to-one relationship between the SNDR and the BER that can be derived (or determined numerically) for any given coding scheme and constellation type. The drawback is that the SNDR does not take in to account the rate loss that may result from PAR reduction. On the other hand, the capacity, encompasses the SNDR and the data rate, but may not be achievable.

The out-of-band distortion is not necessarily quantified by either the capacity or the SNDR. When the SNDR is measured in the time domain the SNDR includes both in-band and out-of-band distortion. However, this time-domain SNDR may not be an accurate indicator of the BER. Also, many practical systems do not require that the out-of-band distortion be minimized, only that it be held to a level that is below a defined threshold, which is usually referred to as the spectral mask.

Complicating the matter of quantifying the usefulness of PAR-reduction schemes further, is the fact that some PAR-reduction schemes synergistically incorporate existing parts of the communications system for PAR-reduction purposes. For instance, there are several methods that take advantage of coding that is already used in the system to decrease the PAR. In this case, it would not be fair to penalize the PAR reduction method for all of the redundancy required by the code, as this redundancy would exist even without the PAR reduction. Extracting the overhead of just the PAR reduction part of the scheme to make a meaningful comparison to other schemes can be challenging. Other methods may take advantage of subcarriers that would not otherwise be used to transmit data. Still other methods, including one presented in this proposal, modify part of the synchronization signal to realize a PAR reduction.

In the following thesis, we will examine and compare existing PAR-reduction schemes in light of these more all-encompassing metrics. Additionally, we will present novel PAR-reduction techniques and modifications to existing techniques that have advantages in light

of the more comprehensive metrics.

1.2 OFDM

OFDM was first introduced in the mid-1960s [26] and later patented in 1970 [27]. Early on, OFDM's main appeal was that high-complexity equalization was not necessary because data was sent in parallel on different subcarriers. OFDM was also touted for its ability to fully use the available bandwidth, combat impulsive noise and mitigate the effects of multipath fading.

In 1971 Weinstein and Ebert introduced the idea of using the discrete Fourier transform in the modulation/demodulation process [119]. Prior to this breakthrough, OFDM systems were prohibitively complex because arrays of sinusoidal generators and coherent demodulators were necessary in the implementation. With special-purpose fast Fourier transform (FFT) chips, the entire OFDM system could be implemented digitally.

More recently, OFDM has been implemented in mobile wideband data transmission (IEEE 802.11a, Hiperlan II), high-bit-rate digital subscriber lines (HDSL), asymmetric digital subscriber lines (ADSL), very high-speed digital subscriber lines (VHDSL), digital audio broadcasting (DAB), digital television and high-definition television (HDTV) [129]. It is also the implemented for the IEEE 802.16 WiMAX [1] standard and its predecessor multicarrier multipoint distribution service (MMDS).

1.2.1 System Definition

In an OFDM system, data is modulated in the frequency domain to N adjacent subcarriers. These N subcarriers span a bandwidth of B Hz and are separated by a spacing of $\Delta f = B/N$. The continuous-time baseband representation of this is

$$y(t) = \frac{1}{\sqrt{N}} \sum_{k=\mathcal{I}} X_k \, e^{j2\pi\Delta fkt/T}, \quad t \in [0, T], \tag{1.1}$$

where $T = 1/\Delta f$ is the symbol period, $\{X_k\}_{k=0}^{N-1}$ are the data symbols drawn from a finite constellation and $\mathcal{I}$ are the data subcarrier indices. A shaping window or filter may also be applied to the OFDM system in practical systems. After symbol creation, the symbol are concatenated and transmitted serially in time.

Because all modern communications systems are processed digitally and only made continuous right before transmission it is often convenient to work with in the oversampled discrete time OFDM symbol, defined by

$$y_{n/L} = \frac{1}{\sqrt{LN}} \sum_{k=\mathcal{I}} X_k \, e^{\frac{j2\pi kn}{NL}} \quad n \in \{0, 1, ..., NL - 1\}, \tag{1.2}$$

where L is the oversampling factor.

Another key component of OFDM systems is that, when properly designed, they are immune to inter-symbol interference (ISI). The immunity comes from the cyclic prefix that is appended to the beginning of each OFDM symbol,

$$y_n^{(\text{cp})} = \begin{cases} y_{n+N}, & n \in \{-P, -P+1, ..., -1\} \\ y_n, & n \in \{0, 1, ..., N-1]\}, \end{cases} \tag{1.3}$$

where P is the length of the cyclic prefix and should be chosen such that $P \geq N_\tau$ with N_τ defined as the maximum delay spread of the discretized channel impulse response function $\{h_n\}_{n=0}^{N_\tau-1}$. At the receiver the cyclic prefix is ignored and the resulting symbol is equalized in the frequency domain.

It may be convenient to describe OFDM in terms of matrix equations. Define the discrete Fourier transform matrix to be

$$[\mathbf{Q}]_{k,n} = (LN)^{-1/2} \exp(-j2\pi(n-1)(k-1)/LN), \ 1 \leq k, n \leq LN, \tag{1.4}$$

where $[\mathbf{Q}]_{i,k}$ denotes entry in the ith row and the kth column of matrix $\mathbf{Q}$ and the cyclic prefix matrix to be

$$\mathbf{C} = \left[\begin{array}{c} \mathbf{0}_{PxLN-P} \mid \mathbf{I}_P \\ \hline \mathbf{I}_{LN} \end{array} \right] \in \mathbb{R}^{LN+P \text{ x } LN}. \tag{1.5}$$

Finally, the vector version of $x_{\text{cp}}[n]$ can be written as

$$\mathbf{y} = \begin{bmatrix} y_{-P}^{(\text{cp})} \\ y_{-P+1}^{(\text{cp})} \\ \vdots \\ y_{LN-1}^{(\text{cp})} \end{bmatrix} = \mathbf{C}\mathbf{Q}^{\mathcal{H}}\mathbf{x}, \tag{1.6}$$

where $\cdot^{\mathcal{H}}$ is the Hermitian transpose of a matrix. A block diagram of the OFDM system is presented in Fig. 1.1
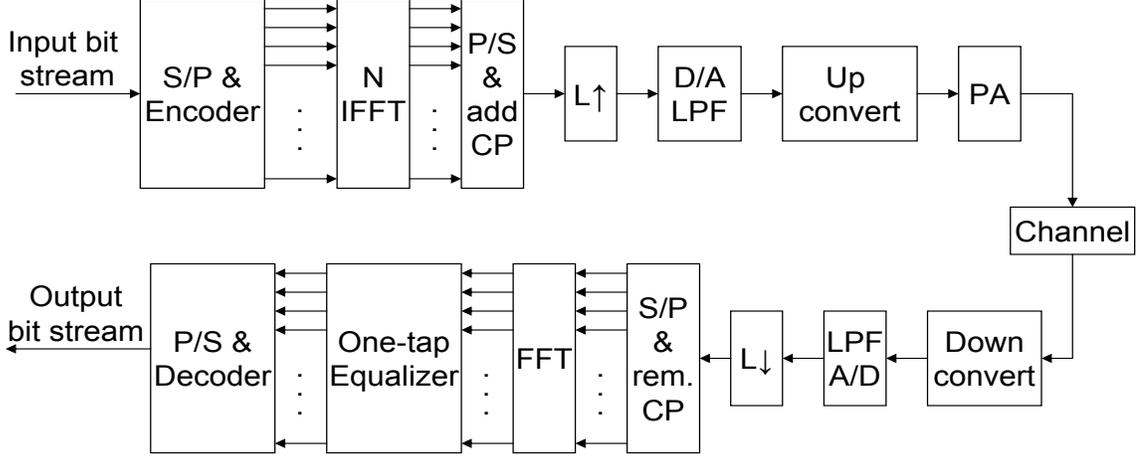
Figure 1.1: OFDM block diagram.

1.2.2 Challenges

Despite the widespread acceptance of OFDM, it has its drawbacks. One drawback is that OFDM systems are not robust again carrier frequency estimation errors. Even small carrier offsets destroy the orthogonality causing inter-carrier interference (ICI) between the sub-carriers causing drastic error rate increases [87, 98, 5, 72]. Specifically, in [72] an bound on the signal-to-noise ratio (SNR) after ICI was calculated to be

$$SNR_{ICI} = \frac{\sigma_x^2 \left(\frac{\sin(\pi\epsilon)}{\pi\epsilon} \right)}{0.5947\sigma_x^2 \sin^2(\pi\epsilon) + \sigma_v^2}, \tag{1.7}$$

where σ_x^2 is the signal power, σ_v^2 is the noise power and ϵ is the fraction of a subcarrier width that frequency is offset by. A plot of the SNR versus ϵ for various starting SNR values (i.e. σ_x^2/σ_v^2) is plotted in Fig. 1.2.

The other main drawback of OFDM systems is that the time-domain OFDM signals exhibit large power fluctuations in very short periods of time. Such large fluctuations are due the Complex Gaussian distribution of the time domain OFDM samples, which follows from the Central Limit Theorem (CLT). That is, because the time-domain samples are a linear combination of a large number (N) of independent complex random variables (the values of X_k), the CLT states that they will follow a Complex Gaussian distribution. Thus, envelope peaks require a system to accommodate an instantaneous signal power that is larger than the signal average power, necessitating either low operating power efficiencies

6
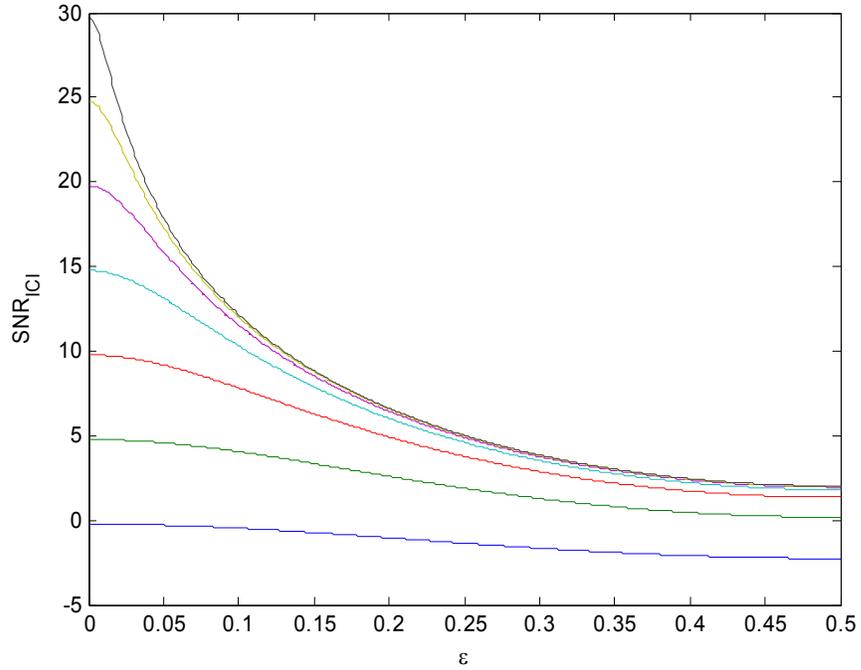
Figure 1.2: Plot of SNR versus ICI for various input SNRs (dB scale).

or power amplifier (PA) saturation. To illustrate, one realization of an OFDM symbol is plotted in Fig. 1.3. It is clear that the peaks of the signal have much larger magnitudes that the average signal power. Mitigating the detrimental effects of these envelope variations is the main topic of this thesis.
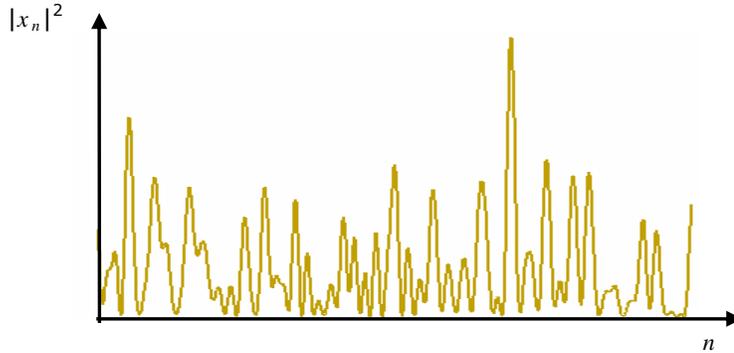
Figure 1.3: Power profile of one OFDM symbol realization.

1.3   Peak-Limited Channels

Peak-power-limited channels provide a more challenging design problem over classically considered average-power-limited channels. Here we consider a simple time-invariant peak-limited channel is defined with the function

$$g(x) = \begin{cases} Ax, & |x| \leq 1 \\ Ae^{j\angle x}, & |x| > 1, \end{cases} \tag{1.8}$$

where A is the peak magnitude limit allowed. Several interesting information theoretic analysis of this type of channel have been discussed in the literature. Notably, Shannon in [104] first provided a lower bound on the peak-limited capacity

$$C(A) \geq \frac{1}{2} \log_2 \left(\frac{2A^2}{\pi e^3 \sigma_v^2} \right). \tag{1.9}$$

More recently, it has been shown that the capacity achieving distribution for peak-limited channels is actually discrete for the real case in [105] and for the complex case in [103]. More concise closed form bounds on the peak-limited capacity are provided in [69]. These interesting information-theoretic results illustrate two important points, i) the capacity-achieving symbol distribution is very nearly the Gaussian distribution truncated to a peak value of A and ii) there is a non-negligible capacity loss by imposing a peak-limited constraint. In the following we will examine the detrimental effects on OFDM symbols in peak-limited channels.

8

1.3.1 SER Degradation

Because the clipping non-linearity $g(\cdot)$ causes distortion, there will be an increase in the number of bit errors in a peak-limited channel. Several formulations have been derived to quantify this degradation. A simple approximation of the distortion noise based on the assumption that x_n is Gaussian distributed was derived in [71]. In that work, the distorted signal was written as $g(y_n) = y_n + d_n$. Thus, the variance in d_n is

$$\sigma_d^2 = \frac{2}{\sqrt{2\pi\sigma_y^2}} \int_A^\infty (x-A)^2 e^{-x^2/2\sigma_y^2} dx. \tag{1.10}$$

Then, assuming that this distortion is uncorrelated with y and that it is Gaussian (both of which do not hold), the symbol error rate (SER) can be calculated according to

$$SER = 1 - \left[1 - 2\left(1 - \frac{1}{\sqrt{M}}\right) Q\left(\sqrt{\frac{3\sigma_x^2}{(\sigma_d^2 + \sigma_v^2)M - 1}}\right)\right]^2, \tag{1.11}$$

where M is the QAM constellation size [88] and σ_v^2 is the additive Gaussian channel noise.

A refined SER approximation is presented in [109]. There, the clipping noise is treated as impulsive noise and the distortion noise is conditioned on the probability that a sample experiences clipping according to

$$\sigma_d^2 = E[(x - g(x))^2 ||y| > A] \underbrace{Pr(|y| > A)}_{2Q(\sqrt{PSNR})} + \underbrace{E[(x - g(x))^2 ||y| < A]}_{0} \underbrace{Pr(|y| < A)}_{1-2Q(\sqrt{PSNR})} \tag{1.12}$$

where $PSNR = A^2/\sigma_y^2$ and where

$$E[(x - g(x))^2 ||y| > A] = \frac{1}{Q(\sqrt{PSNR})\sqrt{2\pi\sigma_y^2}} \int_A^\infty (x-A)^2 e^{-x^2/2\sigma_y^2} dx. \tag{1.13}$$

Now the probability that k samples are clipped is

$$Pr(k) = \binom{N}{k} \left(1 - 2Q(\sqrt{PSNR})\right)^k \left(2Q(\sqrt{PSNR})\right)^{N-k}, \tag{1.14}$$

thus,

$$SER = 1 - \sum_{k=0}^N Pr(k) \left[1 - 2\left(1 - \frac{1}{\sqrt{M}}\right) Q\left(\sqrt{\frac{3\sigma_x^2}{\left(\frac{k}{N2Q(\sqrt{PSNR})}\sigma_d^2 + \sigma_v^2\right)M - 1}}\right)\right]^2. \tag{1.15}$$

This approximation still assumes that d and y are uncorrelated, which is not strictly true. However, the approximation is still very good as can be seen in Fig. 1.4.
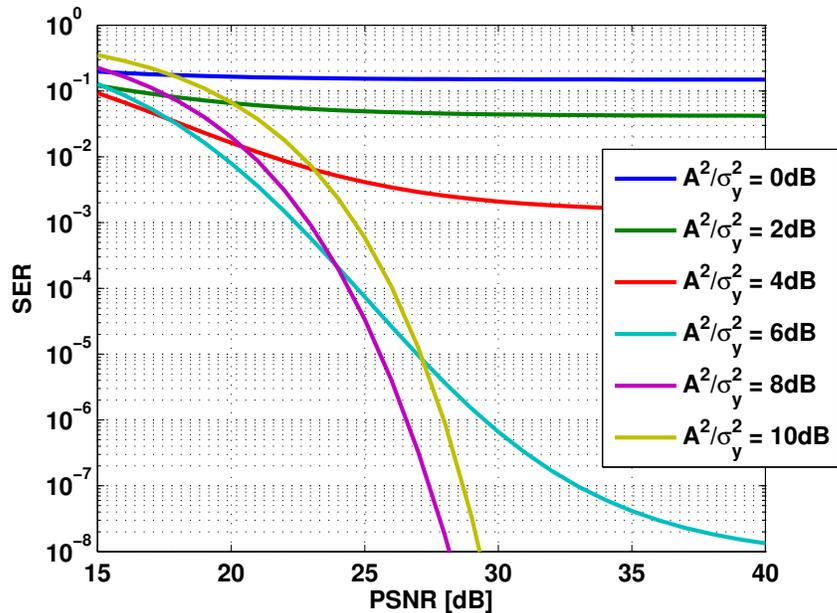
Figure 1.4: SER approximation for a Gaussian signal with various clipping ratios with 16QAM constellation.

1.3.2 Spectral Splatter

Another unfortunate side effect of peak-limiting a signal is that the spectrum expands. Such spectral expansion, or splatter in OFDM can cause unwanted distortions on other users. If we express the nonlinearity $g(\cdot)$ as a complex baseband polynomial

$$z = g(y) = \sum_{k=0}^{K} a_{2k+1}|y|^{2k}y, \tag{1.16}$$

and the input y is Gaussian, then it is straightforward to show [91] that the spectrum of z has the form

$$S_{zz}(f) = \sum_{k=0}^{K} |a_{2k+1}|^2 \left(\bigotimes_{l=0}^{k+1} S_{yy}(f) \right) \left(\bigotimes_{l=0}^{k} S_{yy}(-f) \right), \tag{1.17}$$

where $\bigotimes$ is the multiple convolution operator.

For example, if $y(t)$ is a symmetric band-limited Gaussian, process with low-pass bandwidth B, then we can write

$$S_{zz}(f) = \sum_{k=0}^{K} |a_{2k+1}|^2 \left(\bigotimes_{l=0}^{k+1} S_{yy}(f) \right) \left(\bigotimes_{l=0}^{k} S_{yy}(-f) \right) \qquad (1.18)$$

$$= \sum_{k=0}^{K} |a_{2k+1}|^2 \left(\bigotimes_{l=0}^{2k+1} S_{yy}(f) \right) \qquad (1.19)$$

$$= \sum_{k=0}^{K} |a_{2k+1}|^2 FT \left\{ \left(\frac{\sin(Bx/2)}{Bx/2} \right)^{2k+1} \right\} \qquad (1.20)$$

where

$$U(x) = \begin{cases} 0, & x < 0 \\ 1, & x \geq 0 \end{cases} \qquad (1.21)$$

and the Fourier Transform w.r.t. w of the Nth order Sinc function is

$$FT_w \left\{ \left(\frac{\sin(ax)}{ax} \right)^N \right\} = \frac{1}{(N-1)!2^{N+1}} \sum_{n=0}^{N} \binom{N}{n} ((2n-N)a+w)^{N-1} U((2n-N)a+w). \qquad (1.22)$$

Using this formulation, the spectral regrowth of a bandlimited Gaussian signal can easily be calculated. One example is plotted in Fig. 1.5. The plot uses the same parameters that were used in the SER plot in Fig. 1.4. Frequently, signals need to have 50dB of clearance two bandwidths out. It is obvious from Fig. 1.5 that to achieve spectral suppression of 50dB at two bandwidths more than 10dB of signal scaling would be necessary. From Fig. 1.4, it is apparent that $A^2/\sigma_y^2 = 10$dB does not have the best SER performance. Accordingly, it is desirable to find a way to transmit this Gaussian signal through a peak limited channel such that the spectral splatter constraints are met and without giving up too much in terms of SER performance.
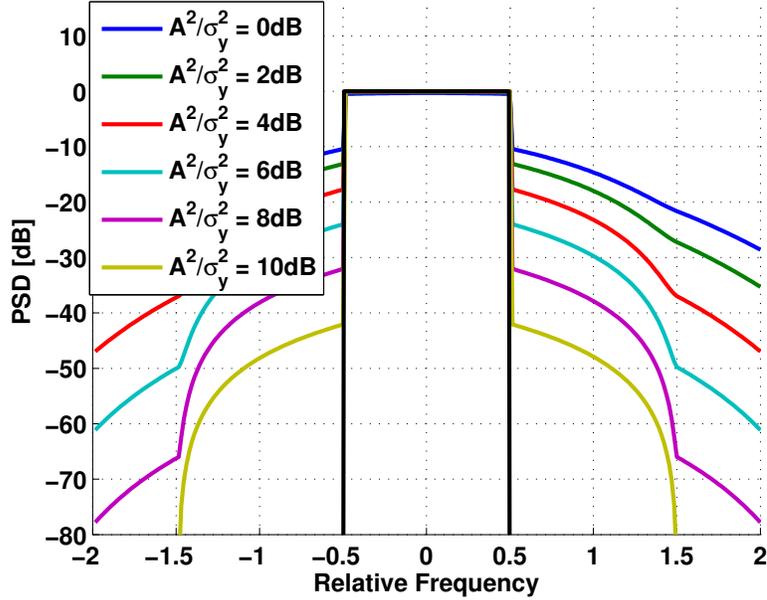
Figure 1.5: Spectral splatter various clipping ratios. The nonlinearity is chosen to have $K = 6$ coefficients with values $\{0.4111, 0.1133, 0.0524, 0.0285, 0.0170, 0.0107\}$. The PSD is plotted so that the in band power is equal to one.

1.4   Envelope Variation Metrics

There are several different metrics that quantify the dynamic range of signals. While these dynamic range metrics are important, they are only a proxy measurement of the truly important system metrics like power efficiency, SER, spectral splatter and error vector magnitude (EVM). However, a significant amount of research has related various dynamic range metrics to these performance metrics.

1.4.1   Instantaneous-to-Average-Power Ratio

The instantaneous-to-average power ratio (IAR) is a straightforward quantification of the signal power distribution and is defined by

$$IAR = \frac{|y_n|^2}{\sigma_y^2}. \tag{1.23}$$

The IAR is a random variable so it is often quantified through its complementary cumulative distribution function (CCDF). In OFDM, when N is large, y_n is Complex Gaussian
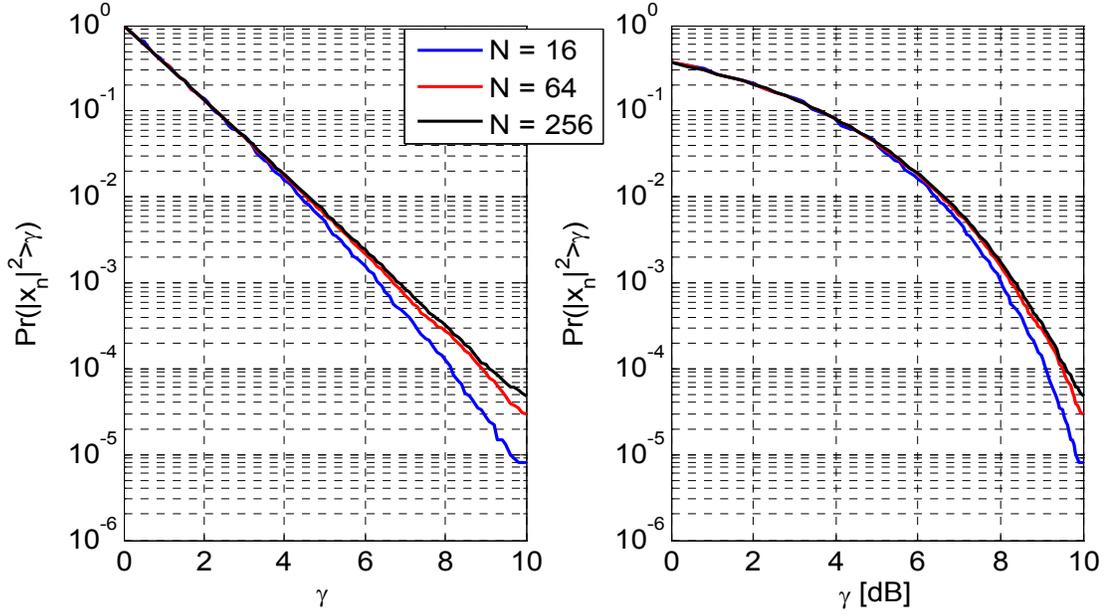
Figure 1.6: The IAR CCDF in both linear and dB scale.

distributed, and IAR follows an Exponential distribution so that the IAR CCDF is

$$CCDF_{IAR}(\gamma) = Pr(IAR > \gamma) = e^{-\gamma}. \tag{1.24}$$

Fig. 1.6 is a plot of the IAR CCDF. The plot demonstrates how the IAR varies as N changes. Unlike the peak-to-average power ratio (PAR) that will be discussed in the next section, the IAR is largely insensitive to the value of N. The variations only occur when N is very small (i.e. $N < 64$) because the samples are not quite Complex Gaussian. However, for practical values of N, the IAR CCDF does not change with N. The peak nature of OFDM can also be observed from Figure 1.6. For instance at the 0.01% level, the IAR is nearly 9.5dB. That is one out of every ten thousand samples exceeds 9.5dB in power. In practical systems, this 0.01% level is often employed to determine power backoff required by the PA. The larger the 0.01% CCDF value, the more backoff is required, which lead to lower power efficiencies.

1.4.2 Peak-to-Average-Power Ratio

The most popular quantification metric of envelope variation is the peak-to-average ratio (PAR)[1]. The use of PAR in communications signals is a result of the use of PAR in radar applications. A radar system shares certain similarities with a communications system; namely, they both have to transmit an amplified radio signal of a certain spectrum. For radar, the spectrum shape is often the only signal constraint, which makes waveform shaping that minimizes peaks a relatively straightforward problem. However, in an OFDM communication system there is the additional constraint that each subcarrier (Fourier coefficient of the spectrum) is modulated with an information bearing complex number. This additional degree of constraint significantly complicates the problem.

Define the PAR of an OFDM signal, x to be

$$PAR\{x\} = \frac{\max|x|^2}{E[|x|^2]},\tag{1.25}$$

where x and be any signal representation (critically sampled baseband, oversampled baseband, continuous-time passband, etc.) defined over one symbol period. Because the denominator of (1.25) is an expected value and, strictly speaking, not an "average," it is true that the term PAR is a bit of a misnomer. Despite this slight technical inaccuracy, PAR is the most widely used term and we will keep with convention here. Also, note that the ensemble average power and the expectation in the denominator of (1.25) only differs for non-constant modulus constellations. Figure 1.7 is a plot of the PAR of $x[n]$ for different N. It is obvious that at all probability levels the PAR increases with N

In the discrete-time case, where only the Nyquist sampled analog signal is examined, the cumulative distribution function (CDF) can be easily derived if certain assumptions are made. First we assume that N, the number of subcarriers, is large enough so that the discrete-time domain signal has an approximate complex Gaussian distribution [22]. It then follows that the instantaneous power of the discrete-time domain samples is Chi-Squared distributed. Therefore, for a given $n = n_o$, $|x_{n_o}|^2$ is χ^2 distributed with two degrees of

---

[1]PAR is alternately referred to as the PAPR (peak-to-average power ratio) and PMEPR (peak to mean envelope power ratio). PAR is also directly related to the crest factor (CF) of a signal where $CF = \sqrt{PAR}$.
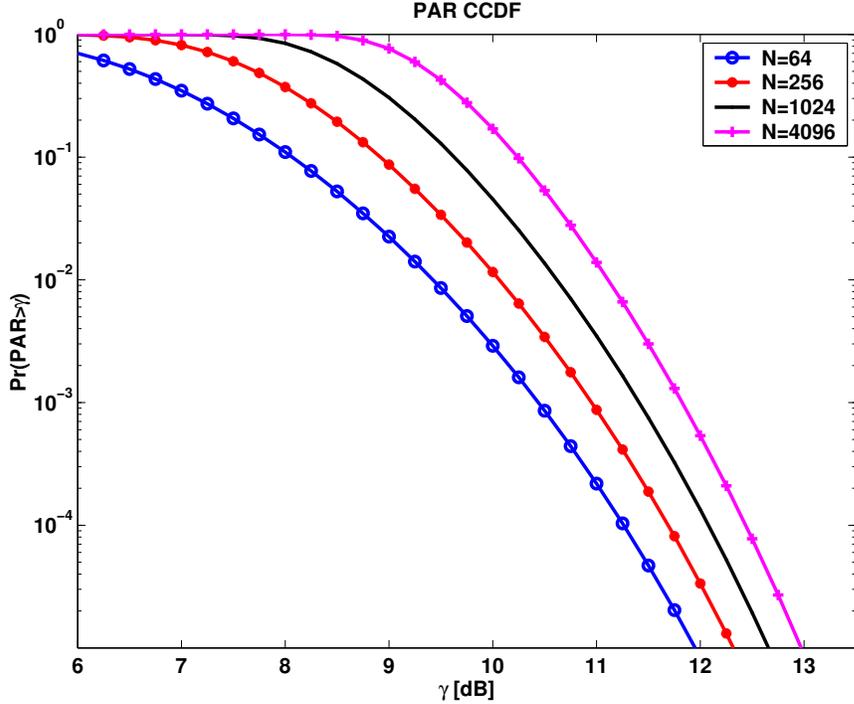
Figure 1.7: CCDF of the discrete-time PAR for various values of N.

freedom. So $Pr[|x_{n_o}|^2 < \gamma] = 1 - e^{-\sigma_x^2 \gamma}$. Furthermore, according to Theorem 4.4.1 of [22], after the IFFT each discrete time sample can be treated as independent of all other samples. With these two approximations, the probability that the power of at least one $x[n]$ out of N samples is above a given level, γ, is

$$\Pr\left[\max_{0 \leq n < N} |x_n|^2 < \gamma\right] = (1 - e^{-\sigma_x^2 \gamma})^N. \tag{1.26}$$

Finally, if $E\left[|x_n|^2\right]$ is normalized to unity, then the CCDF of the PAR is

$$\Pr\left[PAR\{x_n\} > \gamma\right] = 1 - (1 - e^{-\gamma})^N. \tag{1.27}$$

Equation 1.27 is a very good approximation to the PAR distribution of x_n, but differs but as much as one dB from the PAR distribution of $x(t)$. There have been several attempts to determine the distribution of $x(t)$. The first came from [114], where is was claimed that

$$\Pr\left[PAR\{x(t)\} > \gamma\right] \approx 1 - (1 - e^{-\gamma})^{2.8N}, \tag{1.28}$$

which is just a intuitive modification to the CCDF that resulted from the Gaussian approximation in (1.27). Later in [35], a more theoretical analysis of the problem was done based

15

on level crossing probabilities of $x(t)$, where the ratio f_c/B was taken into account as well as the power distribution of X_k. They concluded that for $f_c >> B$ and a constant modulus power distribution that

$$\Pr\left[PAR\{x(t)\} > \gamma\right] \leq N\sqrt{\frac{\pi}{3}}\gamma e^{-\gamma}. \tag{1.29}$$

In [81], the authors present the approximation

$$\Pr\left[PAR\{x(t)\} > \gamma\right] \approx \begin{cases} \left(1 - \frac{\sqrt{\gamma}e^{-\gamma}}{\sqrt{\bar{r}}e^{-\bar{r}}}\right)^{N\sqrt{\frac{\pi}{3}\bar{r}}e^{-\bar{r}}}, & \gamma > \bar{r}; \\ 0, & \gamma \leq \bar{r}, \end{cases} \tag{1.30}$$

where $\bar{r} = \sqrt{\pi}$, based on the level crossing rates of $x(t)$. The authors further refine (1.30) for large γ to

$$\Pr\left[PAR\{x(t)\} > \gamma\right] \approx e^{N\sqrt{\frac{\pi}{3}\gamma}e^{-\gamma}}. \tag{1.31}$$

In order to test these approximations it is necessary to resort to digital signal theory where it is known that as $L \to \infty$, $x_{n/L} \to x(t)$. It follows that the PAR of $x_{n/L}$ approaches the PAR of $x(t)$ for large L. Thus we should be able to approximate $PAR\{x(t)\}$ by running simulations on the oversampled signal $x_{n/L}$.

Figure 1.8 is a plot of each approximation to the PAR of $x(t)$ as well as the PAR of $x_{n/L}$ for $L \in \{1, 2, 4, 8\}$. From the plot we can see that the oversampled PAR is only slightly larger than the Nyquist-sampled PAR. Additionally, the PAR for $L = 4$ is very close to the $L = 8$ case, which is indistinguishable from larger Ls (not plotted). The approximations to the continuous-time PAR are fairly tight, but they all appear to be upper bounds.
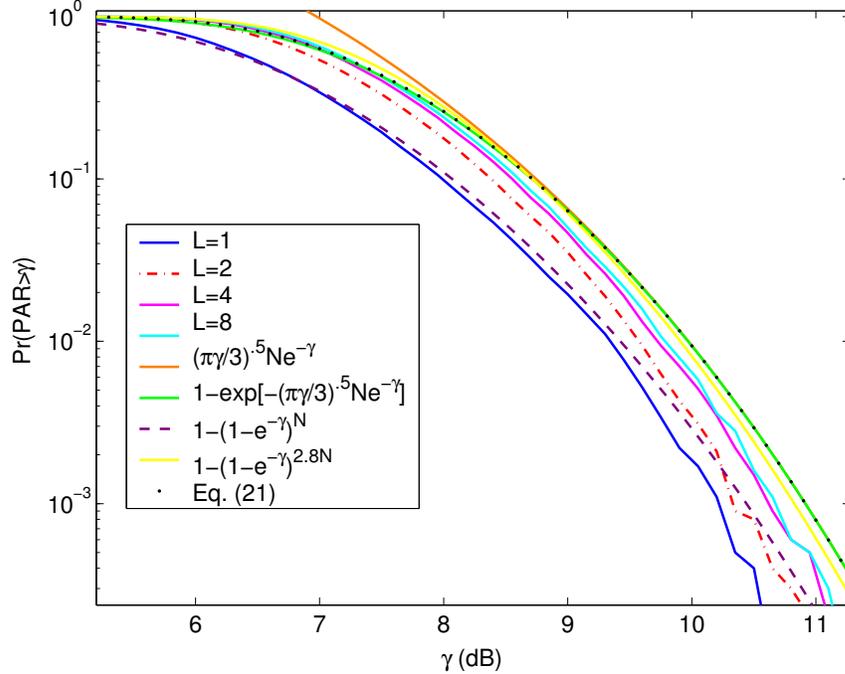
Figure 1.8: CCDF of the PAR for $L \in \{1, 2, 4, 8\}$, $N = 64$ and the approximations in (1.27), (1.28), (1.29), (1.30) and (1.31).

1.5 Accommodating OFDM in Peak-Limited Channels

When designing a communications system it is important to consider the effects of nonlinearities contained in the system. Specifically, to maximize performance it may be necessary to modify the signals prior to the nonlinearity. In the following section we provide an outline of the three types of signal modifications: scaling, predistortion, and PAR reduction. At the receiver, depending on the PAR-reduction method used, receiver cooperation may be necessary too. An idealized system would implement all four of these modifications in an optimal way to maximize performance. The block diagram of such a system is plot in Fig. 1.9.

1.5.1 Predistortion

Digital predistortion (DPD) is the process which corrects the power amplifier nonlinearity digitally by applying a nonlinear function to the to-be-transmitted signal before it passed through the PA nonlinearity. Ideally, the concatenation of the DPD nonlinearity and the PA nonlinearity will result in a linear response function. In [92], the optimal DPD/PA
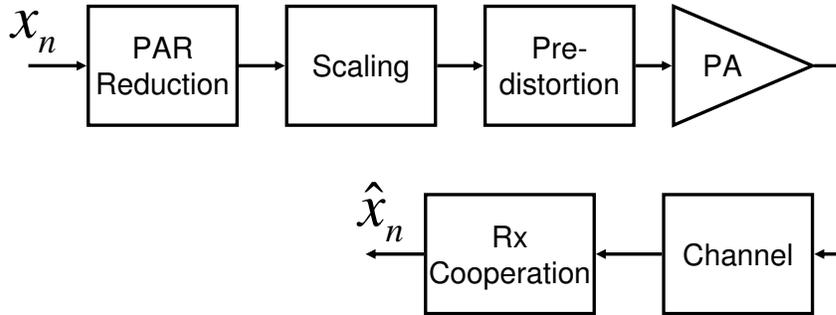
Figure 1.9: Block of signal modifications used to mitigate peak limitations in an OFDM system.

concatenation function was derived and shown to be soft limiting with gain. Thus, the DPD function needs to be chosen to be the exact inverse of the PA response up to the saturation point.

With the result from [92], the general idea of DPD is straightforward but implementation can be complicated in several ways. For instance, it is possible of the PA to have a time-varying nonlinear characteristic, which necessitates that the DPD function include a time dependency. In this case, a more general time-varying function is necessary to characterize the PA such as a Volterra series [40]. A further complication is that inverting the PA characteristic may involve a matrix inverse operation, which is computationally expensive and highly sensitive to round off errors. Accordingly ,orthogonal polynomial PA models [91] have been proposed to mitigate round off errors and look-up table inversion [74] implementations have been proposed to alleviate some of the computational strain. Overall the DPD research has indicated that DPD is capable of reducing spectral leakage, lowering BERs and increasing power efficiency. All of these points present a strong argument for inclusion of DPD into OFDM systems. Using this logic, most authors who consider PAR reduction methods assume a soft limiter PA characteristic. As demonstrated in [92], any other PA characteristic should be predistorted so that the overall system results in a soft limiter (with gain) characteristic.

1.5.2 Symbol Scaling

Scaling techniques adjust the amount of signal power by using a linear scaling factor. Because the scaling operation is linear scaling techniques do not affect the PAR of the signal. However, the concatenation of the scaling technique and the PA does cause a PAR reduction. For the purposes of this thesis, such a concatenation will be view as a type of clipping technique. The difference is that clipping techniques are performed digitally, prior to the PA. Then the clipped signal is sent through the PA where it may experience additional distortion. The following two sub-sections outline static scaling (or backoff) and piece-wise backoff, respectively.

1.5.2.1 Static Backoff

In a static backoff system the input symbol is backoffed by a scaling factor β, which is constant for all symbols. Thus, the resulting symbol is βx_n. The power efficiency can be calculated according to

$$\eta_{sbo} = \frac{\int_{D(|x|)} p_{|x|}(z)q(\beta z)^2 dz}{P_{DC}}.$$

(1.32)

where $q(\cdot)$ is the nonlinear response of the PA. As a simple example, the Class A PA power efficiency is plotted versus the backoff amount in Figure 1.10. While different classes of PAs can achieve higher power efficiencies than the Class A curves plotted, the Figure still accurately demonstrates how power efficiency is decreasing in the amount of power backoff.

1.5.2.2 Piecewise Linear Scaling

Piecewise linear scaling (PWLS) is a scaling method that takes advantage of the symbol structure of OFDM [79]. In all practical implementations of OFDM, pilot tones are transmitted along with the data tones so that the receiver can estimate and then compensate for channel variations. With this structure in place, it is possible to scale every symbol with a different factor. Then, the receiver can use the pilot tones to detect the scaling factor. In PWLS, the transmitted signal $\beta_n x_n$, where the scaling factor is block dependent such that

$$\beta_n = \frac{A}{\max_n |x_n|}.$$

(1.33)
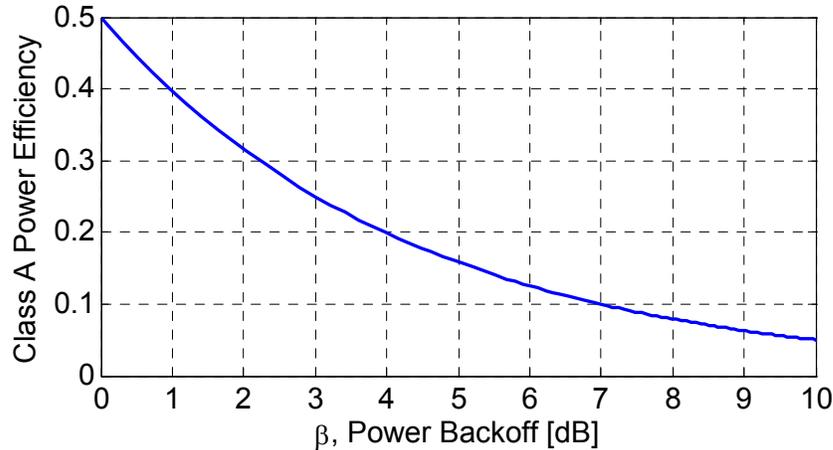
Figure 1.10: Class A power efficiency versus power backoff.

Since the denominator is a function of the peak value of the symbol, it is intuitive that there is a relationship between the PAR and the power efficiency in PWLS, which is

$$\eta_{pwls} = E\left[\frac{1}{2PAR}\right] \qquad (1.34)$$

for Class A PAs. This is in contrast to the static backoff case in 1.32 where there is no relationship between the PAR and the power efficiency. The point is that the PAR is a very important metric to measure the performance of PWLS systems, whereas the IAR is more pertinent for static backoff systems. Figure 1.11 is a plot of the PWLS power efficiency versus the number of subcarriers. The plot illustrates that the more subcarriers are present, the lower the power efficiency will be.

1.5.3 PAR Reduction

The final component of an OFDM transceiver that needs to be considered is PAR reduction. So far, we have discussed scaling techniques whereby a linear scaling factor is applied to the incoming signal to mitigate distortion and DPD techniques which modify incoming signals so that after they pass through the PA the will have been linearly amplified. PAR reduction is fundamentally different from these first two components. Unlike scaling and DPD, PAR reduction techniques attempt to reduce that peak power for the same average power. As we have seen in Fig. 1.11, the power efficiency is closely related to the PAR, so lowering the PAR by making it less common for OFDM symbols to posses a high PAR, will increase
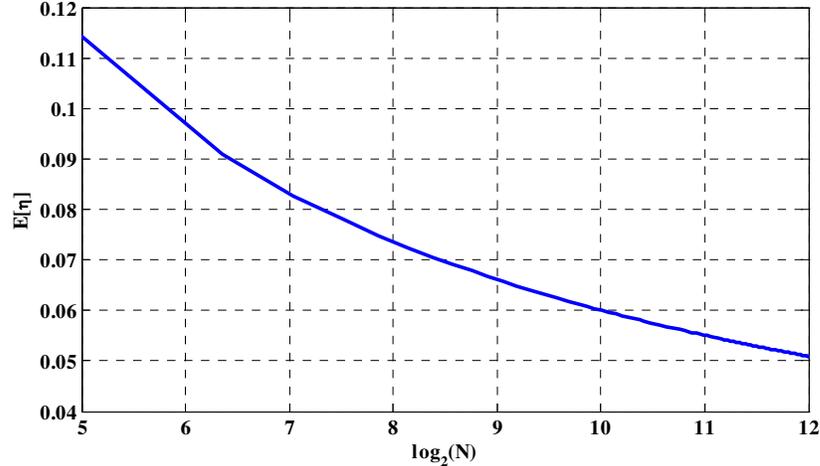
Figure 1.11: Plot of the PWLS power efficiency versus the number of subcarriers.

power efficiency. We have also seen that, under certain system configurations, the power efficiency is related to a statistic of the IAR distribution. While reducing the PAR at all probability levels does not necessarily lead to an IAR reduction at all probability levels, it is safe to say that all practical PAR reduction algorithms will also produce a desired IAR reduction.

PAR reduction methods can be broken into two main groups: distortion methods and distortionless methods. Distortion methods allow some level of distortion to be incurred during the PAR reduction operation. Distortion methods spread out the incurred distortion in the frequency domain so that the constraints of the method are met. Conversely, distortionless methods incur only reversible distortion to reduce the PAR. At the receiver, a reverse operation is performed to recover the original signal. The tradeoff for distortionless methods is increased computational complexity and required receiver-side cooperation. Receiver-side cooperation is particularly undesirable for open loop systems where different manufactures produce the mobile and the base stations.

On the other hand, distortionless algorithms can achieve large PAR reductions without any distortion, so it may behoove future standards to incorporate provisions for distortionless algorithms in order to maximize power efficiency. Distortion-based algorithms come at the expense of another set of tradeoffs. The most obvious of which is distortion. Most distortion algorithms control how the distortion is allocated so that the required constraints
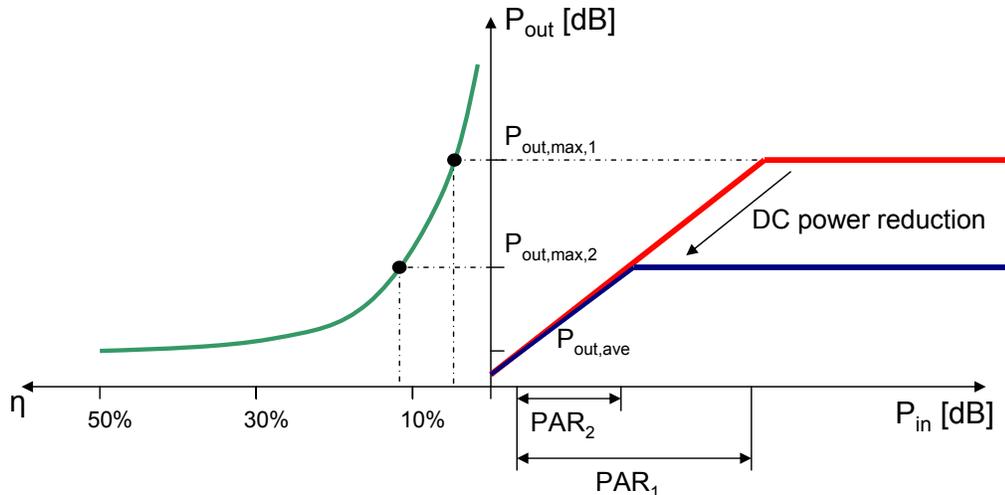
Figure 1.12: Illustration of the efficiency improvement that can be realized by PAR reduction.

can be met, but even controlled distortion may not be desirable in certain scenarios. The other two main tradeoffs in distortion algorithms are computational complexity and latency. Depending on how precise of a solution is required for each transmit symbol, extremely complicated optimization algorithms may be called for. In that case, the complexity of a distortion algorithm could be unacceptably high for most practical systems.

Fig. 1.12 illustrates the effect of PAR of the power efficiency. On the right is a PA response for a signal with a high PAR (PAR1) and for a signal with a low PAR (PAR2). Both responses produce the same average output power, but the lower PAR signal achieves this output power with a lower saturation level and hence, a lower bias point. Assuming the PAs are Class A, the power efficiency is plotted on the left. Based on the plot, it can be demonstrated that the power efficiency goes from 5% to 11% in this hypothetical example. Such power efficiency improvements can be realized with only a 3dB PAR reduction. In economic terms, a double in power efficiency leads to a halving in the power costs, so such improvements can be extremely lucrative if implemented.

1.6   Thesis Organization

In the following thesis the topics concerning the problem of transmitting OFDM signals through peak-limited channels are analyzed. We start in Chapter 2 by examining the

effect of using signal-to-noise-plus-distortion ratio (SNDR) as a metric for peak-limited systems. As part of that chapter, we also provide a comprehensive analysis of the difference possibilities for scaling signals prior to the peak limitation. In Chapter 3 we use the findings in Chapter 2 and modify a popular PAR reduction algorithm known as selected mapping (SLM) such that SNDR is maximized. In Chapter 4 SLM is compared to another popular PAR reduction scheme known as partial transmit sequence (PTS). The findings show that SLM is preferred over SLM under all metrics tested. As part of comparing SLM and PTS, the computationally complexity of pruned FFTs had to be determined. In Chapter 5 we provide a derivation of the pruned FFT complexity based on a Markov model analysis of the FFT butterfly structure. In Chapter 6 magnitude SLM is introduced as a blind SLM technique. In Chapter 7 a method for generating low-PAR joint pilot and synchronization sequences (JSPSs) is developed. In Chapter 8 the JSPSs are exploited as part of an SLM-like OFDM scheme to enable harsh channel synchronization and equalization while achieving low PAR symbols. In Chapter 9 the design of JSPSs is extended further by optimizing the pilot spacing so that the symbol estimation MSE is minimized. In Chapter 10, we formulate the SNDR-optimal receivers for peak-limited transmitters. Finally, in Chapter 11 we provide a summary of the results presented throughout the thesis.

CHAPTER II

A COMPARISON OF SNDR MAXIMIZATION TECHNIQUES FOR OFDM

When an orthogonal frequency division multiplexing (OFDM) signal is transmitted through a peak-power limited device, system designers must choose from several options to deal with the large dynamic range problem of OFDM. In this chapter, we are interested in comparing i) clipping with gain, ii) modified piece-wise linear scaling (MPWLS) and iii) piecewise optimized clipping (PWOC) techniques in terms of the signal-to-noise-plus-distortion ratio (SNDR) metric. Existing work has shown that on a per-sample basis, clipping with a judiciously chosen gain and clipping ratio, dubbed uniform optimized clipping (UOC), can maximize the SNDR. Here, we are interested in comparing the performance of UOC with MPWLS and PWOC, two methods that allow for symbol-wise SNDR maximization. Through comparison, we show that the symbol-wise methods provide a slightly higher SNDR compared to UOC. However, this increase in performance comes at the expense of higher complexity.

2.1 Introduction

Orthogonal frequency division multiplexing (OFDM) is an attractive multi-carrier transmission method because of its simple equalizer structure[1]. It has been adopted by several communications standards, such as digital audio broadcasting, digital video broadcasting, wireless LAN and wireless MAN. However, one major problem associated with OFDM is its high peak-to-average power ratio (PAR) or crest factor (CF). When a high-PAR signal, such as OFDM, passes through a power amplifier (PA), the PA may be pushed to saturation, causing both in-band and out-of-band distortion. Hence, it is desirable to reduce the PAR

---

[1]Part of this chapter was presented in R. J. Baxley and G. T. Zhou, "A comparison of SNDR maximization techniques for OFDM," *Proc. IEEE Statistical Signal Processing Workshop*, pp. 423-427, Madison, WI, August 2007. Reference [19].

of the input signal in order to maintain a reasonable level of power efficiency or to avoid excessive nonlinear distortion.

In this chapter, three distortion-based PAR-reduction methods will be compared. Clipping is a simple method and has been well studied in the literature. Three previous works are particularly pertinent to the work in this chapter as they present analysis on optimizing clipping in terms of the signal-to-noise-plus-distortion ratio (SNDR) [82, 92, 89]. In fact, in [92] it was proven that the soft clipping transfer function with carefully chosen gain and clipping ratio is SNDR-optimal among all peak-limited functions, when signals are operated on *one sample at a time*. Throughout the remainder of the chapter we refer to this scheme as uniform optimized clipping (UOC).

In this work we will propose two novel distortion-based PAR-reduction methods and compare them with UOC. These methods have an additional degree of freedom compared with UOC in that they operate on signals from block-transmission schemes (e.g. OFDM), *one block at a time*. The first method presented is a generalization of piecewise linear scaling (PWLS) [79] that allows the SNDR to be optimized for any peak-signal-to-noise ratio (PSNR). The second method, dubbed piecewise optimized clipping (PWOC), preforms block-wise optimization to determine the highest SNDR transmitted signal.

2.2 System Model

In OFDM, individual subcarriers in the frequency-domain are modulated with constellation points, transformed to the time-domain and transmitted with a cyclic prefix. For PAR analysis, the cyclic prefix can be ignored since it has no effect on the symbol PAR. Let the frequency-domain vector of constellation points be $\mathbf{x} = [x_1, x_2, ..., x_{N-1}, x_N]^T$, where x_k is drawn from a finite constellation. Using the inverse discrete Fourier transform, the time-domain symbol is

$$\mathbf{y} = \mathbf{Q}\mathbf{x}, \tag{2.1}$$

where $\mathbf{Q}$ is the inverse discrete Fourier transform matrix. For Nyquist sampling, $[\mathbf{Q}]_{k,n} = N^{-1/2}\exp(j2\pi(n-1)(k-1)/N)$. In general, this matrix model can be extended to the

oversampling case by properly choosing the columns of $\mathbf{Q}$ to represent the baseband over-sampled frequencies. In fact, the analysis in this chapter can be extended to any block transmission scheme by choosing the appropriate matrix $\mathbf{Q}$ (e.g. code division multiple access (CDMA) can be analyzed by setting $\mathbf{Q}$ to the Hadamard matrix).

The PAR of the signal $\mathbf{y}$ is defined by

$$PAR(\mathbf{y}) = \frac{\|\mathbf{y}\|_\infty^2}{\sigma_y^2}, \tag{2.2}$$

where σ_y^2 is the power in each element of $\mathbf{y}$ (the elements of $\mathbf{y}$ are assumed to have the same variance). For transmission through a peak-power limited device it is desirable to carry out crest factor reduction for high PAR (or crest factor) signals.

The device in this chapter is assumed memoryless and peak-power limited to a maximum power of A. The transfer function of the peak-limited device is

$$c(z) = \begin{cases} \sqrt{A}z, & |z| \leq 1 \\ \sqrt{A}\, e^{j\angle z}, & |z| > 1 \end{cases}, \tag{2.3}$$

where z is the signal before the peak-limiting process, and $\angle z$ is its angle. Thus, $|c(z)|^2 \leq A$. In the linear region, the power gain of this device is A. By generalizing $c(\cdot)$ to a vector function $c(\mathbf{z}) : \mathbb{C}^{N \times 1} \to \mathbb{C}^{N \times 1}$, the overall channel becomes $c(\mathbf{z}) + \mathbf{w}$, where $\mathbf{w}$ is additive white Gaussian noise (AWGN).

Three schemes for generating $\mathbf{z} = g(\mathbf{y})$ $(g(\mathbf{y}) : \mathbb{C}^{N \times 1} \to \mathbb{C}^{N \times 1})$, where $\mathbf{y}$ is the time-domain OFDM symbol given in (2.1), are compared in this chapter. The resulting $\mathbf{z}$ is then passed through $c(\mathbf{z})$ defined in (2.3). The metric used to quantify the performance of each scheme is the signal-to-noise-plus- distortion ratio (SNDR). Notice that $\mathbf{r} = c(\mathbf{z})$ can be written as the sum of a scaled version of $\mathbf{y}$ and an uncorrelated distortion term, i.e. $\mathbf{r} = c \circ g(\mathbf{y}) = \alpha\mathbf{y} + \mathbf{d}$, where α is chosen so that $E[\mathbf{y}^{\mathcal{H}}\mathbf{d}] = 0$ [92]. Assuming that the AWGN channel noise $\mathbf{w}$ is uncorrelated with $\mathbf{y}$ and $\mathbf{d}$, i.e. $E[\mathbf{y}^{\mathcal{H}}\mathbf{w}] = E[\mathbf{d}^{\mathcal{H}}\mathbf{w}] = 0$, then the SNDR is defined as

$$SNDR = \frac{|\alpha|^2 E[\mathbf{y}^{\mathcal{H}}\mathbf{y}]}{E[\mathbf{d}^{\mathcal{H}}\mathbf{d}] + E[\mathbf{w}^{\mathcal{H}}\mathbf{w}]}. \tag{2.4}$$

By inferring that $\alpha = E[\mathbf{y}^{\mathcal{H}}\mathbf{r}]/(N\sigma_y^2)$ and that $E[\mathbf{d}^{\mathcal{H}}\mathbf{d}] = E[\mathbf{r}^{\mathcal{H}}\mathbf{r}] - |E[\mathbf{y}^{\mathcal{H}}\mathbf{r}]|^2/(N\sigma_y^2)$, (2.4)

can be rewritten as

$$SNDR = \frac{|\mathrm{E}[\mathbf{y}^{\mathcal{H}}\mathbf{r}]|^2}{\mathrm{E}[\mathbf{r}^{\mathcal{H}}\mathbf{r}]N\sigma_y^2 - |\mathrm{E}[\mathbf{y}^{\mathcal{H}}\mathbf{r}]|^2 + N^2\sigma_w^2\sigma_y^2}, \tag{2.5}$$

where σ_w^2 is the noise power. The objective is to design the function $g(\mathbf{y})$ so that after the peak-limiting device, the resulting process, $c \circ g(\mathbf{y}) + \mathbf{w}$ has a higher SNDR than $c(\mathbf{y}) + \mathbf{w}$.

2.3 Uniform Optimized Clipping (UOC)

In the UOC scheme

$$\mathbf{z} = g(\mathbf{y}) = \frac{\mathbf{y}}{\eta\sigma_y}, \tag{2.6}$$

where η is a scaling factor that is sample-independent (i.e. uniform for all samples). In [92], the authors provided a proof that the composition $c \circ g(\cdot)$, with $c(\cdot)$ from (2.3) and an η properly chosen for the $g(\cdot)$ in (2.6), maximizes the SNDR among all memoryless nonlinear mappings with a peak-power limit A. For Gaussian samples $\mathbf{y}$, the SNDR-optimal η can be calculated using $\eta^\star = T^{-1}(A/\sigma_w^2)$, where

$$T(\eta) = \frac{2\eta}{\sqrt{\pi}\mathrm{erfc}(\eta)}. \tag{2.7}$$

The above claim from [92] assumes that every sample of $\mathbf{y}$ is scaled by the same factor $1/(\eta\sigma_y)$. However, in block transmission schemes like OFDM, there is some flexibility w.r.t. the scaling factor. Since each block is equalized separately and inter-symbol interference is avoided with the use of a cyclic prefix, it is possible to use different scaling factors (or clipping levels) for different blocks. The following two sections present two alternative block-scaling methods that take advantage of this extra degree of freedom that block transmission affords.

2.4 (Modified) Piecewise Linear Scaling ((M)PWLS)

PWLS was presented and analyzed in [79]. The idea behind PWLS, is to scale the signal prior to transmission so that no part of the signal would be clipped. Thus, the signal is scaled by a factor of $1/\|\mathbf{y}\|_\infty$ so that

$$\mathbf{z} = g(\mathbf{y}) = \frac{\mathbf{y}}{\|\mathbf{y}\|_\infty}. \tag{2.8}$$

27
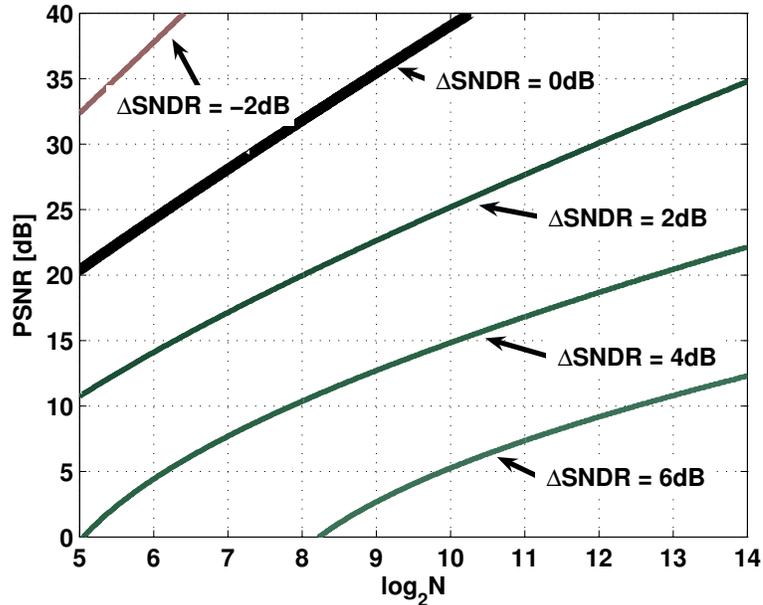
Figure 2.1: Level curves of the SNDR differential between UOC and PWLS. To the top left of the bold line, PWLS outperforms UOC, to the bottom right of the bold line, UOC outperforms PWLS.

Here $|\mathbf{z}|^2 \leq 1$ so $\mathbf{z}$ is scaled linearly without clipping when passing through the $c(\cdot)$ in (2.3). Unlike UOC, the scaling factor in PWLS changes every block based on the peak amplitude of $\mathbf{y}$.

Fig. 2.1 is a plot of the level curves for ΔSNDR, which is the difference (in dB) between the UOC SNDR and the PWLS SNDR. The plot demonstrates that, despite UOC being SNDR-optimal on a per-sample basis, PWLS can outperform clipping for certain values of N and PSNR, where $PSNR = A/\sigma_w^2$. Specifically, when N is small or when the PSNR is high, PWLS is preferable.

Despite better performance in some regions of the N-PSNR plane, PWLS is at a disadvantage to UOC in other regions of the plane. This is attributed to PWLS being too "conservative" in trying to avoid any clipping and thus not delivering sufficient signal power. In [89], it was pointed out that deliberately introduced non-linearity can lead to SNDR improvements. Based on this observation, as a modification to improve the performance of
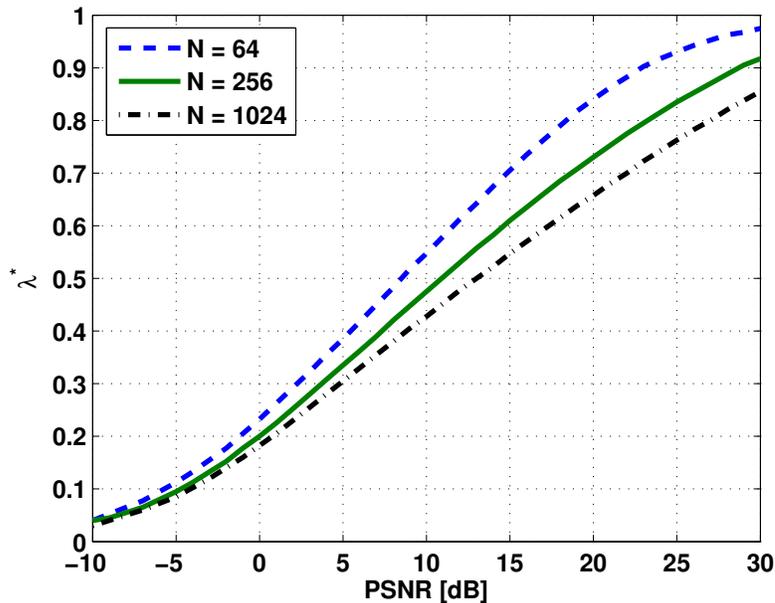
Figure 2.2: SNDR-optimal values for λ.

PWLS, we propose that the scaling factor be parameterized with a PSNR-dependent variable λ so that

$$\mathbf{z} = g(\mathbf{y}) = \frac{\mathbf{y}}{\sqrt{\lambda}\|\mathbf{y}\|_\infty}. \qquad (2.9)$$

We call this modified PWLS (MPWLS). Notice that $\lambda \in (0,1]$. For the special case when $\lambda = 1$, MPLWS will be identical to PWLS. For $\lambda \in (0,1)$, $\mathbf{z}$ in (2.9) will necessarily experience some clipping distortion when it is passed through $c(\cdot)$. However, some distortion maybe a desirable tradeoff for the increase in signal power so the end result may be a larger SNDR. Thus, it is necessary to optimize λ in terms of the PSNR and the number of subcarriers N.

Through Monte Carlo simulations we are able to determine the SNDR optimizing values for λ, $\lambda^\star$. Fig. 2.2 is a plot of $\lambda^\star$ versus the PSNR. Interestingly, the trend shows that for high PSNR, larger values of λ are required so that less clipping is incurred. Conversely, in the low-PSNR regime, λ is relatively smaller which results in relatively more clipping distortion but also more transmitted signal power. A similar trend is reported in the clipping scheme [92] for the optimal back-off values, η, from (2.6).

Fig. 2.3 is a plot of the level curves for ΔSNDR, which is the difference (in dB) between
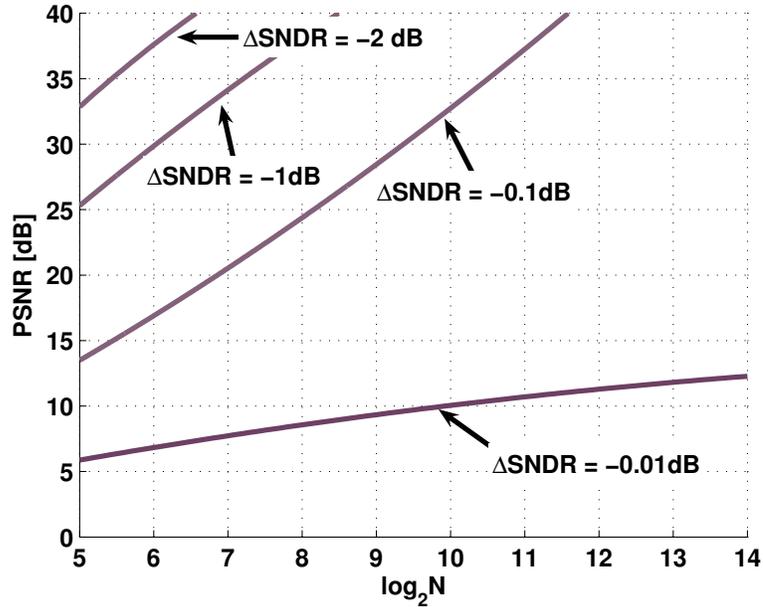
Figure 2.3: Level curves of the SNDR differential between UOC and MPWLS. Negative values for ΔSNDR indicate that MPWLS outperforms UOC.

the UOC SNDR and the MPWLS SNDR. As expected, MPWLS always outperforms UOC. However, in certain regions of the N-PSNR plane the performance gap is relatively small. Comparing Fig. 2.3 and Fig. 2.1, we see that MPWLS is an improvement over PWLS.

2.5 Piecewise Optimized Clipping (PWOC)

In UOC, the scaling factor is block-independent and in MPWLS, the scaling factor is related to the block PAR, which can outperform UOC. However, MPWLS is not SNDR-optimal among all possible peak-limiting signal modifications that operate in a block-wise fashion. Instead, the global SNDR-optimal solution can be found by maximizing the instantaneous SNDR of each block defined by

$$\overline{SNDR}(\mathbf{y}, \mathbf{r}) = \frac{|\mathbf{y}^{\mathcal{H}}\mathbf{r}|^2}{\|\mathbf{y}\|_2^2\|\mathbf{r}\|_2^2 - |\mathbf{y}^{\mathcal{H}}\mathbf{r}|^2 + N\|\mathbf{y}\|_2^2\sigma_w^2}. \tag{2.10}$$

Notice that this definition is ambivalent to the sign of $\mathbf{r}$, which means that $\overline{SNDR}(\mathbf{y}, \mathbf{r}) = \overline{SNDR}(\mathbf{y}, -\mathbf{r})$. To alleviate this ambiguity and make the problem concave, the $\mathbf{r}$ chosen is the one most in the direction of $\mathbf{y}$. Thus, for each symbol an optimization problem needs to be solved in order to maximize the SNDR. Define $\mathbf{z} = g(\mathbf{y})$ for PWOC to be the function

30

that solves

$$\text{maximize} \quad \overline{SNDR}(\mathbf{y}, \sqrt{A}\mathbf{z})$$
$$\text{subject to} \quad \|\mathbf{z}\|_\infty \leq 1,$$
$$\Re(\mathbf{y}^{\mathcal{H}}\mathbf{z}) \geq 0. \tag{2.11}$$

Note that since $\|\mathbf{z}\|_\infty \leq 1$, $\mathbf{r} = c(\mathbf{z}) = \sqrt{A}\mathbf{z}$. It is straightforward to show that this is a concave problem that can be solved using interior point methods (see [21]). In fact, the gradient of $\overline{SNDR}(\mathbf{y}, \sqrt{A}\mathbf{z})$ is

$$\nabla_{\mathbf{z}}\overline{SNDR}(\mathbf{y}, \sqrt{A}\mathbf{z}) = \mathbf{y}^{\mathcal{H}}\mathbf{z} \left[(\|\mathbf{z}\|_2^2 + N\sigma_w^2/A)\mathbf{y} - (\mathbf{z}^{\mathcal{H}}\mathbf{y})\mathbf{z} \right], \tag{2.12}$$

which can be used in conjunction with the boundary constraint, $\|\mathbf{z}\|_\infty \leq 1$ to perform a gradient ascent search [21] for the SNDR-optimizing vector $\mathbf{z}$. The gradient ascent search (descent search for convex problems), is basically an iterative search technique that finds the optimizing vector by moving in the direction of the gradient in each successive iteration.

To simplify the problem, without loss of generality, assume that in the first iteration, $\mathbf{z}$ is initialized with $\mathbf{y}$. Even after applying the boundary constraints, which do not effect the phase of $\nabla_{\mathbf{z}}\overline{SNDR}$, both $\mathbf{y}^{\mathcal{H}}\mathbf{z}$ and, trivially, $\mathbf{z}^{\mathcal{H}}\mathbf{y}$ are real numbers. Thus, the gradient always searches in the direction of $\mathbf{y}$ subject to $\|\mathbf{z}\|_\infty^2 \leq 1$. Based on this, the optimization problem in (2.11) can be simplified from an N-variate problem to a single-variate problem. Specifically, the optimization problem in (2.11) is equivalent to

$$\text{maximize} \quad \overline{SNDR}(\mathbf{y}, c(\rho\mathbf{y}))$$
$$\text{subject to} \quad \rho > 0, \tag{2.13}$$

where $c(\cdot)$ is the function defined in (2.3), $c(\rho^{\star}\mathbf{y}) = \sqrt{A}\mathbf{z}$, and $\rho^{\star}$ is the optimizing value of ρ. Notice that the problem in (2.13) can be solved with a simple grid search, which has convergence that is geometric in the iteration number, i.e. $\|c(\rho^{\star}\mathbf{y}) - c(\rho^{(i)}\mathbf{y})\|_2^2 \propto 10^{-i}$, where $\rho^{(i)}$ is the value of ρ after i iterations [126]. Because PWOC maximizes the instantaneous symbol SNDR, $\overline{SNDR}$, it is obvious that the scheme also maximizes the SNDR, which is $E[\overline{SNDR}]$. Thus, the PWOC SNDR will be the upper-bound SNDR under the peak-limited channel constraint for block-wise signaling schemes.

2.6 Comparisons

To re-cap, we have considered two methods that will incur clipping distortion: UOC and MPWLS. We emphasize that the clipping notion that we are referring to here differs from the simple slipping technique in [80, 60, 55], where the clipped signal is

$$\tilde{c}(y) = \begin{cases} y, & |y| \leq \sqrt{A} \\ \sqrt{A}\, e^{j\angle y}, & |y| > \sqrt{A} \end{cases}. \tag{2.14}$$

No gain is applied in (2.14), and (2.14) is not SNDR-optimal even on a per-sample basis. In UOC and MPWLS, $\mathbf{y}$ is judiciously scaled to $\mathbf{z}$ via $\mathbf{z} = g(\mathbf{y})$ and the $c(\cdot)$ function in (2.3) is then applied to $\mathbf{z}$. The key to designing $g(\cdot)$ is to ensure that the average power increase due to scaling dominates any increase in the clipping distortion power.

For the two other methods discussed in this chapter, namely PWLS and PWOC, the $g(\cdot)$ functions are designed such that $|\mathbf{z}| < 1$ and thus $c(\mathbf{z}) = \sqrt{A}\mathbf{z}$ and no clipping distortion is encountered. As we will see, PWLS is too "timid", whereas PWOC performs the best since it maximizes the instantaneous SNDR for each block.

In this section, we will evaluate the complexity and SNDR performance of each of the discussed schemes: UOC, MPWLS and PWOC. First, in terms of complexity, UOC is the simplest scheme to implement with a complexity of $O(N)$ as only a multiplication with $1/\eta$ is necessary for each sample. Next, MPWLS requires determining the peak values of each symbol and the multiplication of each sample by $1/\sqrt{\lambda}$, which is more than twice as complex. However, the complexity is still linear in N so MPWLS also has complexity $O(N)$. Finally, using the modified objective function in (2.13), each of the iterations of the grid search has a complexity linear in N so for I iterations, the complexity is $O(NI)$.

Fig. 2.4 is a plot of the SNDR for the three schemes versus the relevant parameters. The plot demonstrates the importance of proper parameter selection in both UOC and MPWLS. Notice that for $\lambda = 1$, MPWLS becomes PWLS. The plot shows that for the PSNRs plotted, the $\lambda = 1$ case has a significant SNDR disadvantage compared to the optimal λ case. The plot also demonstrates that MPWLS has an SNDR that is near the upper-bound PWOC SNDR.
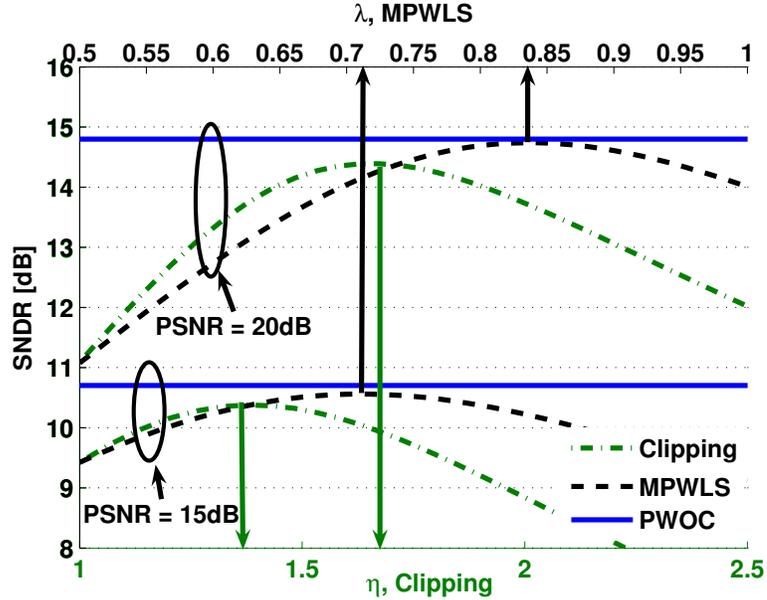
Figure 2.4: Plot of the three methods versus η for UOC on the bottom x-axis and versus λ for MPWLS corresponding to the top x-axis; $N = 64$. In the plot vertical arrows indicate which axis each line is read to.

Fig. 2.5 is a plot of the difference between PSNR and SNDR, which confirms that the SNDR performance of MPWLS is very close to the PWOC SNDR bound. In the plot, the UOC and PWLS performances are also evaluated. UOC has an impressive performance in the low-PSNR region compared to the other schemes considering that it has the lowest complexity. Conversely, PWLS is meaningful only at high PSNR values. However, PWLS is the only scheme that does not require any transmitter-side knowledge about the channel noise level. Also, it should be noted that distortionless PAR-reduction techniques such as those discussed in [8] may improve the performance of PWLS and narrow its SNDR performance gap with the other schemes.

Fig. 2.6 demonstrates the SNDR gains that can be realized by using a PAR-reduction technique. For the plot, selected mapping (SLM) [7] was used with 16 phase mappings, which corresponds to 4 bits of side information. That is, the signal $\mathbf{y}$ that is modified by the three schemes is the lowest-PAR signal among 16 alternative signal mappings (including the original OFDM signal). The SNDR savings relative to UOC (compared with Fig. 2.5) is evident across all the curves plotted.
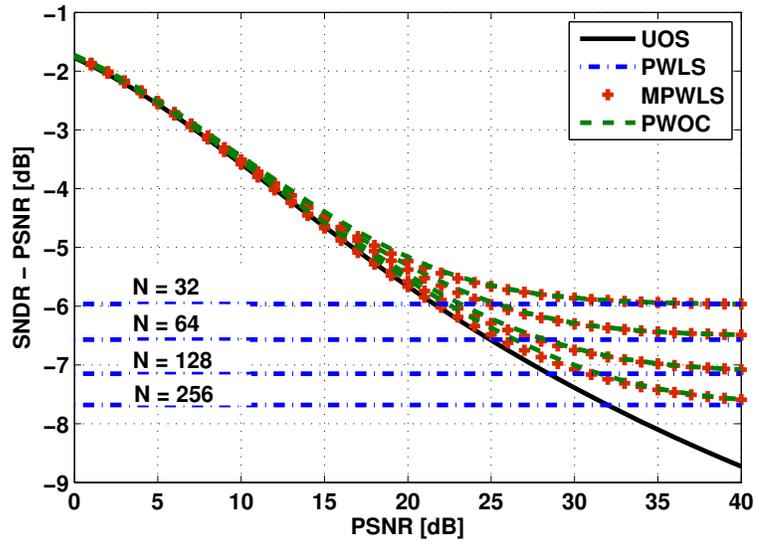
Figure 2.5: Plot of the difference $SNDR - PSNR$ in dB scale.
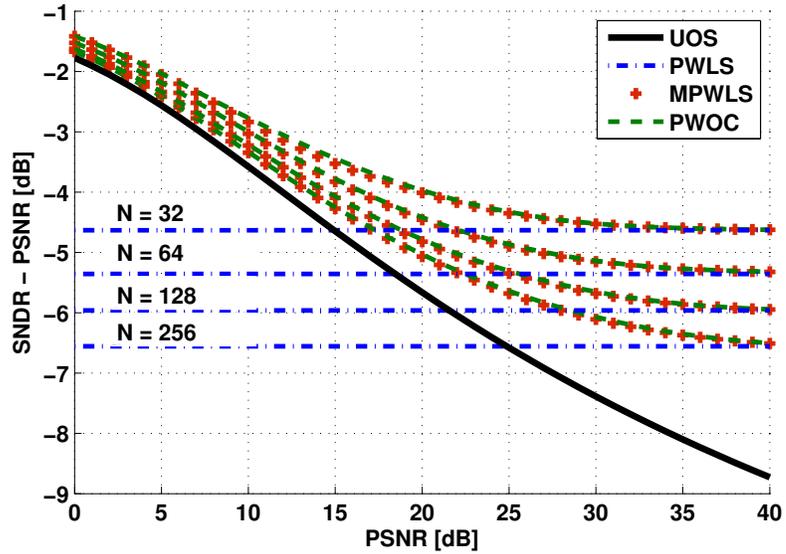
Figure 2.6: Plot of the difference $SNDR - PSNR$ in dB scale, where 16 mappings are used in the selected mapping (SLM) PAR-reduction technique.

2.7 Conclusions

In this chapter we have presented a comparison of three SNDR optimization schemes: UOC, MPWLS and PWOC. Both MPWLS and PWOC are new schemes proposed in this chapter that are designed to operate upon block-wise communications signals such as OFDM. Specifically, we demonstrated that PWOC will create signals that have the upper-bound SNDR. Using this upper bound, we also demonstrated that the significantly less complex technique, MPWLS, results in signals that have SNDR values very near the upper bound. Additionally, we showed that the proposed techniques can be combined with distortionless PAR-reduction algorithms such as SLM to increase the SNDR. Future research will focus on determining the SNDR-optimal scaling factor in UOC and MPWLS for the case when there is limited knowledge of the channel noise and the case where there is a spectral mask constraint.

CHAPTER III

SNDR CONSIDERATIONS FOR THE MINIMUM CLIPPING
POWER LOSS SCHEME

Orthogonal frequency division multiplexing (OFDM) is a robust wireless communications scheme but has the disadvantage that the symbols have a large dynamic range. Many proposals have been presented for suppressing the large peaks of an OFDM symbol so that higher power efficiencies can be achieved. In this chapter, we will examine the recently proposed partial-transmit-sequence-based minimum clipping power loss scheme (MCPLS) and show how it can be generalized to apply to selected mapping (SLM) as well. Additionally, we will relate the clipping power metric in MPCLS to the signal to noise plus distortion ratio (SNDR) that is more commonly used to quantify clipping distortion. Finally, we will derive the SNDR-maximizing parameters that should be used in the new SLM-MPCLS scheme.

3.1   Introduction

Orthogonal frequency division multiplexing (OFDM) is a popular physical layer modulation format that is being widely adopted by a variety of wireless communications standards[1]. OFDM has the advantage of a simple equalizer structure and due to the frequency division nature of OFDM, it is also easy to allocate different channels to different users. However, OFDM has the draw back that it does not perform well in peak-limited channels. Unlike single carrier signals, OFDM signals have a large dynamic range which is difficult for peak-limited devices like digital-to-analog converters and power amplifiers to accommodate. Thus, it is desirable to find methods to reduce the dynamic range of OFDM signals so that they can pass through peak limited devices without incurring too much unwanted distortion. Typically, the nonlinear distortion manifests itself as a bit error rate (BER) degradation

---

[1]Part of this chapter was presented in R. J. Baxley and G. T. Zhou, "SNDR considerations for the minimum clipping power loss scheme," *Proc. IEEE Military Communications Conference*, Orlando, FL, October 2007. Reference [20].

and as out-of-band spectral distortion.

It is common in the literature to find the peak distribution of OFDM signals quantified through the peak-to-average power ratio (PAR). Accordingly, many researchers have proposed PAR reduction methods, which effectively reduced the high peaks of an OFDM signal. One popular method is known as selected mapping (SLM) [7]. In SLM, multiple signal realizations are created and the lowest-PAR realization is transmitted. Another method that can be viewed as a generalization of SLM is called partial transmit sequence (PTS) [76] which was proposed as a low-complexity alternative to SLM. However, in [17], it was demonstrated that SLM actually outperforms PTS in terms of PAR reduction (and distortion reduction) per unit of complexity.

In addition to all of the promising PAR-reduction research, it has been argued that other peak-distribution metrics, besides PAR, can be useful when considering OFDM transmission through peak-limited channels. In [59], it was suggested that, by using PTS where the minimum clipping distortion realization is selected for transmission instead of the minimum-PAR realization, the BER can be improved. In [97] a similar argument was made showing that the intermodulation distortion should be used instead of the PAR.

In this chapter, we will provide a theoretical analysis of the minimum clipping power loss scheme (MCPLS) presented in [59]. Specifically, we will show how the clipping power is related to the signal-to-noise-plus-distortion ratio (SNDR). Ideally, the SNDR should be maximized in order to minimize the BER. With the link to SNDR established, we will then extend the MCPLS method to the SLM. Finally, we will derive the SNDR-optimal parameters that should be used with SLM-MCPLS.

3.2 *OFDM and SLM-MCPLS*

For the purposes of examining the OFDM in peak limited channels, we can adopt a baseband OFDM model where the baseband OFDM symbol $\{x_{n/L}\}_{n=0}^{NL-1}$ is an oversampled IFFT output of the data vector $\{X_k\}_{k=0}^{N-1}$, a sequence of (complex) numbers drawn from a finite

constellation. That is,

$$
\begin{aligned}
x_{n/L} &= \frac{1}{\sqrt{LN}}\left(\sum_{k=0}^{N/2-1} X_k e^{\frac{j2\pi kn}{LN}} + \sum_{k=N/2}^{N-1} X_k e^{\frac{j2\pi(k-N)n}{LN}} \right) \\
&= \text{IFFT}\{X_k\},
\end{aligned} \tag{3.1}
$$

where L is the oversampling factor, N is the number of subcarriers, and IFFT$\{\cdot\}$ is NL-point oversampled IFFT indexed by n/L, where $n \in \{0, 1, ..., LN - 1\}$. In [81] the authors demonstrated that when $L \geq 4$ the envelope of $x_{n/L}$ approximates the envelope of the continuous-time signal.

In SLM, M alternative signal mappings are created by phasing the constellation points with M N-length phase sequences, $\phi_k^{(M)}$, where $k \in \{0, 1, ..., N - 1\}$ and $m \in \{1, 2, ..., M\}$. The resulting mappings

$$
X_k^{(m)} = X_k e^{j\phi_k^{(m)}}, \tag{3.2}
$$

can be used to create the time-domain mappings

$$
x_{n/L}^{(m)} = \text{IFFT}\{X_k^{(m)}\}. \tag{3.3}
$$

In the original SLM [7], the transmitted signal is selected to be the lowest-PAR mapping. Contrastingly, in SLM-MCPLS, it is assumed that the channel is peak-limited by a time-invariant nonlinear function

$$
g(x) = \begin{cases} Ax, & |x| \leq 1 \\ Ae^{j\angle x}, & |x| > 1, \end{cases} \tag{3.4}
$$

where A is the peak-limiting value[2]. Additionally, as system designers we have the opportunity to digitally scale the OFDM samples $x_{n/L}$ by a time-invariant factor $1/\eta$, so that $x_{n/L}/\eta$ is sent through the peak-limiting function $g(\cdot)$. In [92], it was proven that such a scaling soft-limiter function is SNDR-optimal among all possible peak-limited functions. Define the distortion noise at each sample to be

$$
B_{n/L}^{(m)} = \left| \frac{Ax_{n/L}^{(m)}}{\eta} - g\left(\frac{x_{n/L}^{(m)}}{\eta} \right) \right|^2. \tag{3.5}
$$

---

[2]Digital predistortion can be applied to any monotonic peak-limiting nonlinear function to realize the soft-limiting channel characteristic in (3.4)

Then, the index of transmitted signal is chosen according to

$$\widetilde{m} = \underset{m \in \{1,2,...,M\}}{\arg\min} \sum_{n=0}^{NL-1} B_{n/L}^{(m)}, \tag{3.6}$$

which means that $x_{n/L}^{(\widetilde{m})}$ is transmitted. At the receiver, $\widetilde{m}$ needs to be recovered so that the transmitter-side phasing can be undone. Many proposals have been made for receiver-side recovery of $\widetilde{m}$ in traditional SLM [51, 15, 28]. Since the structure of SLM and SLM-MCPLS are the same except for the selection metric, any phase sequence recovery method suggested for SLM will also work for SLM-MCPLS.

In the subsequent sections we will define the SNDR and derive expressions that relate the SNDR to η. Once the relationship is established, we will determine the optimizing η, $\bar{\eta}$, in terms of the number of mappings M, such that the SNDR is maximized.

3.3 Signal-to-Noise-Plus-Distortion Ratio

Using Bussgang's Theorem, any memoryless nonlinearity can be decomposed into a sum of two uncorrelated parts according to

$$g(x) = \frac{A}{\eta}(\alpha x + d), \tag{3.7}$$

where α is chosen so that $E[x^*d] = E[d^*x] = 0$ and the indices m and n/L have been dropped from x for clarity.

In [92], it was demonstrated that, given σ_x^2, $E[x^*g(x)]$ and $E[|g(x)|^2]$, the SNDR, Ψ, can be written

$$\Psi \triangleq \frac{\alpha^2 \sigma_x^2}{\sigma_d^2 + \frac{\eta^2}{A^2}\sigma_w^2} \tag{3.8}$$

$$= \frac{|E[x^*g(x)]|^2}{\sigma_x^2 E[|g(x)|^2] - |E[x^*g(x)]|^2 + \sigma_x^2\sigma_w^2}, \tag{3.9}$$

where σ_w^2 is the additive white Gaussian noise (AWGN) power. Alternatively, we can rewrite (3.5) as

$$B_{n/L}^{(m)} = \frac{A^2}{\eta^2} \left| q_{n/L}^{(m)} \right|^2, \tag{3.10}$$

where $q_{n/L}^{(m)} = (|x_{n/L}^{(m)}| - \eta)I(x_{n/L}^{(m)})$ and

$$I(x) = \begin{cases} 0, & |x| \le \eta \\ 1, & |x| > \eta. \end{cases} \tag{3.11}$$

39

so that the expression

$$\frac{\sigma_x^2}{E\left[\left|q_{n/L}^{(\widetilde{m})}\right|^2\right] + \frac{\eta^2}{A^2}\sigma_w^2} = \frac{\sigma_x^2}{(1-\alpha)^2\sigma_x^2 + \sigma_d^2 + \frac{\eta^2}{A^2}\sigma_w^2}. \tag{3.12}$$

can be used to approximate the SNDR. For clipping functions that are not too harsh, $g(\cdot)$ is approximately linear over the range of x. In this case, $\alpha \approx 1$, so the term $(1-\alpha)^2 \to 0$. Thus, as $\alpha \approx 1$, the SNDR of the $\widetilde{m}$th mapping can be approximated by (3.12). The validity of this approximation will be verified later in the simulations. With this approximation it is possible to describe the SNDR in terms of the mean of $\left|q_{n/L}^{(\widetilde{m})}\right|^2$.

3.4 SNDR Optimization

In this section we will outline the procedure for determining $\bar{\eta}$, for a given M, so that SNDR is maximized. To do this, the SNDR approximation in (3.12) needs to be expressed in terms of η, which involves determining an expression that relates $E\left[|q_{n/L}^{(\widetilde{m})}|^2\right]$ to η. Once the SNDR is expressed in terms of η, the SNDR-maximizing value $\bar{\eta}$ can be found with simple calculus.

When the system nonlinearity is of the soft-limiter form in (3.4), the pdf of $\left|q_{n/L}^{(m)}\right|^2$ can be expressed as

$$f_q(x) = \frac{\sqrt{x}+\eta}{\sigma_x^2\sqrt{x}}\exp\left(\frac{-(\sqrt{x}+\eta)^2}{\sigma_x^2}\right) + \delta(x)\left(1 - \exp\left(\frac{-\eta^2}{\sigma_x^2}\right)\right), \tag{3.13}$$

where $x \in [0,\infty)$. The form of this pdf makes finding a closed form for the pdf of $q_{n/L}^{(\widetilde{m})}$ difficult. Instead, define

$$C_L^{(m)} = \frac{1}{NL}\sum_{n=0}^{NL-1}\left|q_{n/L}^{(m)}\right|^2, \tag{3.14}$$

which is a scaled version of the metric used in (3.6), to determine the transmitted mapping index $\widetilde{m}$. Since $q_{n/L}$ and $q_{i/L}$ are correlated when $(i-n)/L \notin \mathbb{Z}$, here, the Nyquist total distortion $C_1^{(m)}$ is used to estimate the over-sampled total distortion $C_L^{(m)}$. Since $C_1^{(\widetilde{m})}$ is an unbiased estimator of $E\left[|q_{n/L}^{(\widetilde{m})}|^2\right]$, its mean is the same as $E\left[|q_{n/L}^{(\widetilde{m})}|^2\right]$. Accordingly, we will derive $E[C_1^{(\widetilde{m})}]$ and substitute it in to (3.12) for $E\left[|q_{n/L}^{(\widetilde{m})}|^2\right]$.

Next, we will find the distribution of $C_1^{(m)}$, which can be used to find the distribution of $C_1^{(\widetilde{m})}$, the minimizing $C_1^{(m)}$ among M trials. As an alternative to using multiple

convolutions of (3.13) to derive $C_1^{(m)}$, the central limit theorem can be evoked such that $C_1^{(m)} \sim \mathcal{N}(\mu_C, \sigma_C^2)$, where

$$\mu_C = e^{-\eta^2} - \eta\sqrt{\pi}\mathrm{erfc}(\eta), \tag{3.15}$$

$$\sigma_C^2 = 2e^{-\eta^2}(1 + \eta^2) - \eta\sqrt{\pi}(3 + 2\eta^2)\mathrm{erfc}(\eta) - \mu_C^2 \tag{3.16}$$

and $\mathrm{erfc}(x) \triangleq \frac{2}{\sqrt{\pi}}\int_x^\infty e^{-t^2}dt$.

Next, the distribution of $C_1^{(\widetilde{m})}$, which is the minimum $C_1^{(m)}$ among M trials, needs to be determined. The CDF of $C_1^{(m)}$ is

$$F_{C^{(m)}}(z) = \frac{1}{2}\left(2 - \mathrm{erfc}\left(\frac{z - \mu_C}{\sigma_C\sqrt{2}}\right)\right), \tag{3.17}$$

where μ_C and σ_C^2 are defined in (3.15) and (3.16). From this, it can be shown that the CDF of $C_1^{(\widetilde{m})}$ can be written as

$$F_{C^{(\bar{m})}}(z) = 1 - \frac{1}{2^M}\left(\mathrm{erfc}\left(\frac{z - \mu_C}{\sigma_C\sqrt{2}}\right)\right)^M. \tag{3.18}$$

Thus, the distribution of $C_1^{(\widetilde{m})}$, assuming that $C_1^{(m)} \,\forall\, m$ is Gaussian, is

$$f_{C^{(\bar{m})}}(x) = \frac{M2^{1-M}}{\sigma_C\pi\sqrt{2}}e^{-\frac{(x-\mu_C)^2}{2\sigma_C^2}}\left(\mathrm{erfc}\left(\frac{x - \mu_C}{\sigma_C\sqrt{2}}\right)\right)^{M-1} \tag{3.19}$$

Finally, the desired mean can be calculated numerically using

$$E[C_1^{(\widetilde{m})}] = E\left[|q_{n/L}^{(\widetilde{m})}|^2\right] = \int_0^\infty x f_{C^{(\bar{m})}}(x)dx. \tag{3.20}$$

As an alternative, we have found that for small values of M, it is possible to use the closed form approximation

$$E\left[|q_{n/L}^{(\widetilde{m})}|^2\right] \approx \sigma_C\sqrt{2N}\mathrm{erfc}^{-1}\left(2^{1-1/M}\right) + \mu_C, \tag{3.21}$$

which is the median of the $C_1^{(\widetilde{m})}$ distribution defined in (3.19). Finally, $\bar{\eta}$ can be found by solving

$$\frac{-1}{2\eta}\frac{\partial}{\partial\eta}E\left[|q_{n/L}^{(\widetilde{m})}|^2\right] = \frac{\sigma_w^2}{A^2} \tag{3.22}$$

for η, which can be done numerically.

3.5 Simulations

In this section, we will verify the approximations made in deriving $\bar{\eta}$ and show how $\bar{\eta}$ varies with other system variables. Fig. 3.1 is a plot of the SNDR versus η when no noise is present (i.e. the peak signal-to-noise power (PSNR), $\frac{A^2}{\sigma_w^2} \to \infty$). In the plot, the curve labelled 'exact' is the exact SNDR calculated using (3.9) with 10^5 Monte Carlo trials. There are also two approximations in the plot, the first, 'Approx 1' was plotted using (3.20) to calculate the $E\left[|q_{n/L}^{(\widetilde{m})}|^2\right]$, while 'Approx 2' was calculated using (3.21) to calculate the same mean value. The plot shows that both approximations are very close to the exact SNDR curve. Furthermore, the median approximation ('Approx 2') is a better estimate of the SNDR than 'Approx 1', which is convenient since (3.21) is easier to calculate than (3.20).
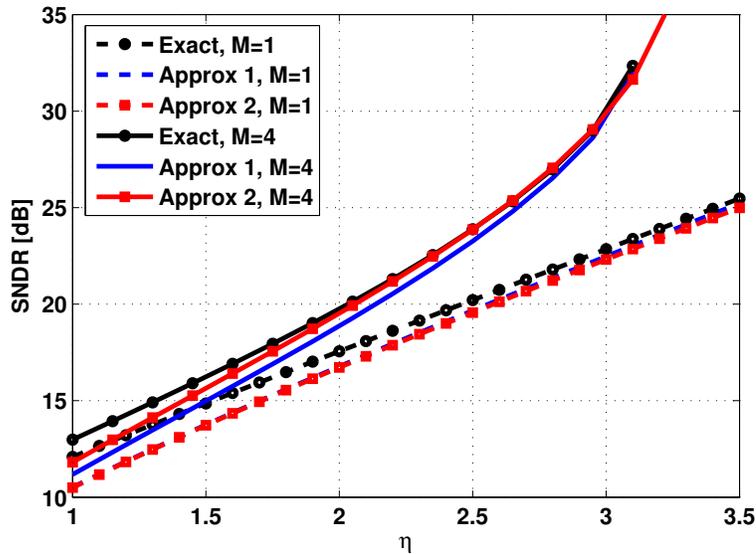
Figure 3.1: SNDR with $\frac{A^2}{\sigma_w^2} \to \infty$, $N = 128$ and $L = 4$.

Fig. 3.2 is a plot of the SNDR with the same parameters as Fig. 3.1 except that $\frac{A^2}{\sigma_w^2} = 25$dB. Again, the plot shows that the approximations are very close to the exact SNDR curve. Also, the plot shows that by incorrectly choosing η, a severe SNDR penalty of more than several dBs may be incurred. Furthermore, even when the maximizing η is used, the $M = 4$ mappings case can return a 1.5dB improvement over the non-SLM $M = 1$ case.
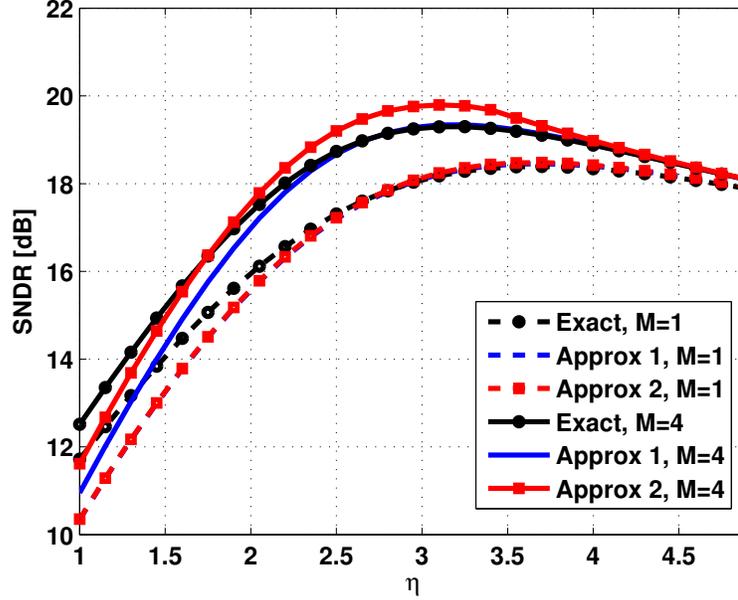
Figure 3.2: SNDR with $\frac{A^2}{\sigma_w^2} = 25$dB, $N = 128$ and $L = 4$.

Fig. 3.3 is a plot of the SNDR-maximizing $\bar{\eta}$ versus $\frac{A^2}{\sigma_w^2}$ for $M \in \{1, 2, 4, 8\}$. The plot was made using the exact SNDR equation in (3.9), but the curves for the two approximations were indistinguishable from the exact curves. The plot can be used by system designers to choose the appropriate $\bar{\eta}$ so that the SNDR is maximized.

Finally, Fig. 3.4 is a plot of the bit error rate (BER) for the proposed SLM-MCPLS for both QPSK and 16-QAM. For the plot, $N = 128$, $L = 4$ and perfect detection of $\widetilde{m}$ is assumed. Also in the plot is the BER of the traditional SLM scheme [7], where the minimum-PAR mapping is selected. For the simulation, the selected signal is scaled down by its PAR so that no part of the signal is clipped [79]. By optimizing the SNDR, SLM-MCPLS significantly outperforms traditional SLM for all scenarios plotted.
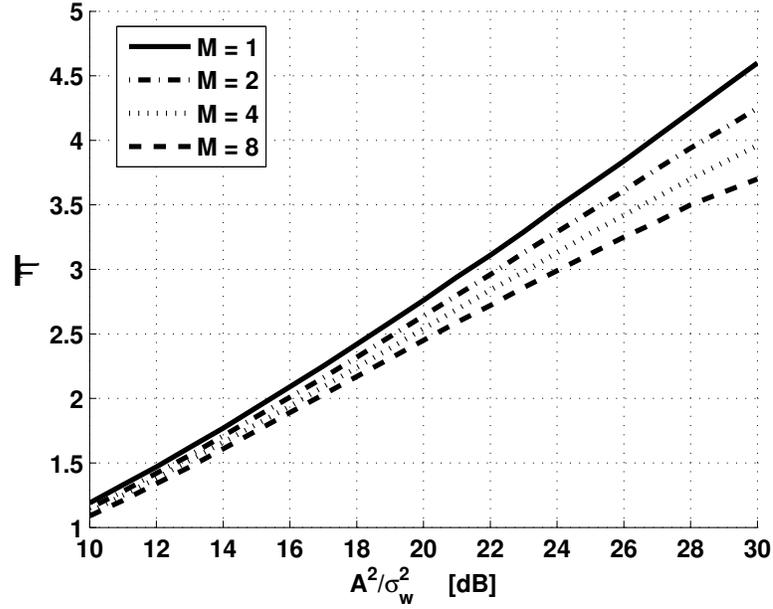
Figure 3.3: Plot of SNDR-optimizing $\bar{\eta}$ versus $\frac{A^2}{\sigma_w^2}$. Where $N = 128$, $L = 4$ and $M \in \{1, 2, 4, 8\}$.
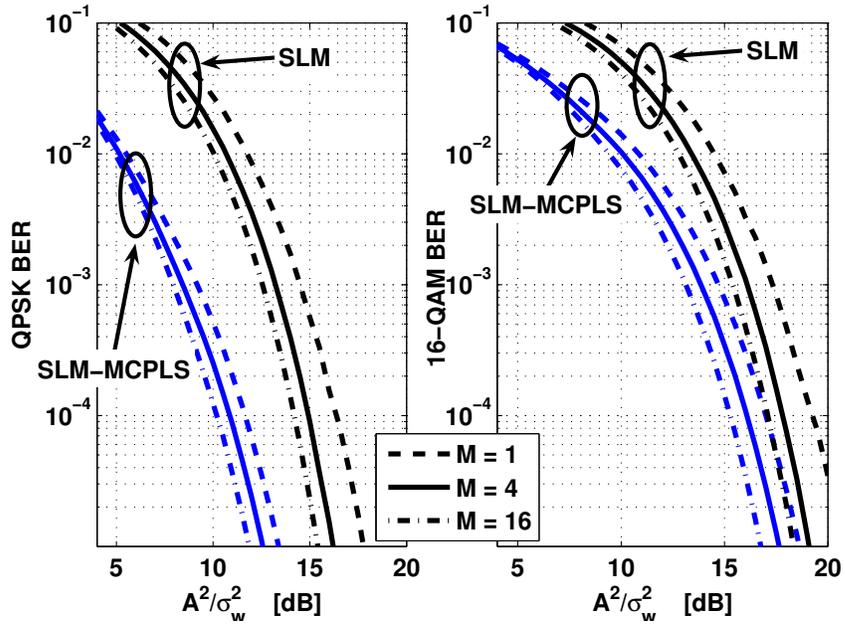
Figure 3.4: Plot of BER versus $\frac{A^2}{\sigma_w^2}$. Comparison of the proposed SLM-MCPLS scheme and traditional SLM.

3.6 Conclusions

In this chapter we have presented the SLM-MCPLS scheme, which is based on the MCPLS scheme presented in [59]. Additionally, we provided a theoretical framework for determining the SNDR in SLM-MCPLS. Using this framework, we demonstrated how the SLM-MCPLS parameters should be chosen so that the SNDR will be maximized. Finally, we compared SLM-MCPLS to traditional SLM in terms of BER and showed that SLM-MCPLS can achieve several dBs of PSNR improvement.

CHAPTER IV

COMPARING SELECTED MAPPING AND PARTIAL TRANSMIT SEQUENCE FOR PAR REDUCTION

Selected mapping (SLM) and partial transmit sequence (PTS) are two existing distortionless peak-to-average power ratio (PAR) reduction schemes that have been proposed for orthogonal frequency division multiplexing (OFDM). Previously, it was argued that SLM and PTS have comparable PAR reduction performance but that the latter has lower computational complexity because it uses fewer IFFTs. In this chapter, we show that the overall computational complexity of PTS is only lower than that of SLM in certain cases, and that SLM always has better PAR reduction performance. We compare the two schemes using three different performance metrics by assuming a given amount of computational complexity that can be afforded. Using the metrics, we show that SLM outperforms PTS for a given amount of complexity.

4.1 Introduction

OFDM is a popular modulation technique with many desirable qualities and has been proposed for the IEEE 802.11a, IEEE 802.11g, IEEE 802.16, the European digital audio broadcasting (DAB) and the European digital video broadcasting (DVB) standards[1]. The desirable attributes of OFDM come at the expense of large envelope variations. Such signal envelope or power variations can be difficult for practical power amplifiers (PAs) to accommodate, resulting in either low power efficiency or distortion-inducing signal clips. The dynamic range of a signal is usually quantified through the peak to average power ratio (PAR) or the crest factor (CF) where $PAR = CF^2$.

There has been a significant amount of research devoted to the development of PAR

---

[1]Part of this chapter was presented in R. J. Baxley and G. T. Zhou, "Comparing selected mapping and partial transmit sequence for PAR reduction," *IEEE Trans. on Broadcasting*, vol. 53, no. 4, pp. 797-803, Dec. 2007. Reference [18].

reduction algorithms for OFDM. An overview of the different approaches can be found in [109, 8, 44]. In this chapter, we are interested in comparing two distortionless PAR reduction algorithms. The first is selected mapping (SLM), which was first presented in [7]. The second algorithm is partial transmit sequence (PTS), which was proposed in [76] and can be viewed as a generalization of the SLM algorithm. Since the initial publication of the algorithms, many proposals have been made to refine the algorithms, including complexity reductions [115, 46, 43, 121, 62, 57], PTS phase optimization [53, 4, 30, 99, 47], techniques to obviate the transmission of side information [51, 16], SLM/PTS combination approaches [123], and extensions to MIMO-OFDM [6].

The objective of this chapter is to come up with some common ground metrics for comparing SLM and PTS. Comparisons of SLM and PTS were made in [75]. In [75], it was claimed that the computational complexity of PTS is lower than that of SLM, but that the two have comparable PAR reduction performance, which we will show is not necessarily true. Unlike [75], we will make quantifiable comparisons based on the PAR reduction per unit of complexity of the two schemes.

For the purposes of comparing SLM and PTS, we can use a simple OFDM model where the baseband OFDM symbol $\{x_{n/L}\}_{n=0}^{NL-1}$ is an oversampled IFFT output of the data vector $\{X_k\}_{k=0}^{N-1}$, a sequence of (complex) numbers drawn from a finite constellation. That is,

$$
\begin{aligned}
x_{n/L} &= \frac{1}{\sqrt{LN}} \left(\sum_{k=0}^{N/2-1} X_k e^{\frac{j2\pi kn}{LN}} + \sum_{k=N/2}^{N-1} X_k e^{\frac{j2\pi(k-N)n}{LN}} \right) \\
&= \text{IFFT}\{X_k\},
\end{aligned}
\tag{4.1}
$$

where L is the oversampling factor, N is the number of subcarriers, and IFFT$\{\cdot\}$ is NL-point oversampled IFFT indexed by n/L, where $n \in \{0, 1, ..., LN-1\}$. The baseband PAR is defined as

$$
\text{PAR}\left\{x_{n/L}\right\} = \frac{\max\limits_{0 \leq n \leq LN-1} |x_{n/L}|^2}{\text{E}[|x_{n/L}|^2]},
\tag{4.2}
$$

which is a random variable.

It is sufficient to examine only the baseband PAR as it is approximately one half of the passband PAR [109]. Also, the cyclic prefix attached to OFDM symbols to combat

inter-symbol interference can be ignored for the purposes of PAR analysis as the prefix will not produce a peak that is not already present in $x_{n/L}$. Finally, it has been shown in [81] that when $L \geq 4$ the envelope of $x_{n/L}$ approximates the continuous-time envelope.

In the next section, we will review SLM and PTS and investigate the relationship between the two schemes. Section III provides computational complexity analysis for both schemes. Section IV introduces three PAR reduction metrics and uses them to compare SLM and PTS. Finally our concluding remarks are provided in Section V.

4.2 Selected Mapping and Partial Transmit Sequence

Selected mapping (SLM): SLM was first described in [7] as a distortionless PAR reduction method. In SLM, D equivalent data sequences are created each by rotating the phases of the original sequence X_k by a distinct sequence $\phi_k^{(d)}$; i.e.,

$$X_k^{(d)} = X_k e^{j\phi_k^{(d)}}, \tag{4.3}$$

which is used to create

$$x_{n/L}^{(d)} = \text{IFFT}\{X_k^{(d)}\} \tag{4.4}$$

where $d \in \{0, 1, ..., D-1\}$. A total of D length-NL IFFTs are performed. From these D candidates, the transmitter selects the lowest PAR sequence, $x_{n/L}^{(\bar{d})}$, for transmission where

$$\bar{d} = \underset{0 \leq d \leq D-1}{\arg \min} \ \text{PAR}\left\{x_{n/L}^{(d)}\right\}. \tag{4.5}$$

It is assumed that the transmitter and the receiver have the table of D length-N phase sequences $\phi_k^{(d)}$. However, in order to recover the original data sequence X_k, the receiver must determine $\bar{d}$. To distinguish $\bar{d}$ from the D possibilities, $\log_2(D)$ bits are needed. Because side information transmission decreases the information throughput, several authors have proposed blind techniques for recovering $\bar{d}$ based only on the received data and the known phase table [51, 28, 15, 127, 83]. In the computational analyses in this chapter, we will assume that the blind maximum-likelihood side information recovery technique is employed, which implies that full complexity complex multiplications will be required to compute (4.3).

Partial transmit sequence (PTS): In a PTS system, $\{X_k\}_{k=0}^{N-1}$ is partitioned into V non-overlapping sub-blocks $\{X_{\mathcal{V}_v}\}_{v=0}^{V-1}$ with indices in the sets $\{\mathcal{V}_v\}_{v=0}^{V-1}$. That is

$$\bigcup_{v=0}^{V-1} \mathcal{V}_v = \{0, 1, ..., N-1\} \tag{4.6}$$

and

$$\sum_{v=0}^{V-1} X_{\mathcal{V}_v} = X_k, \ \forall \ k \in \{0, 1, ..., N-1\}. \tag{4.7}$$

To generate D PTS signal representations, each of the sub-blocks is scaled by a complex constant $e^{j\theta_v^{(d)}}$ and added together so that

$$\begin{aligned}
x_{n/L}^{(d)} &= \text{IFFT}\left\{\sum_{v=0}^{V-1} e^{j\theta_v^{(d)}} X_{\mathcal{V}_v}\right\} \\
&= \sum_{v=0}^{V-1} e^{j\theta_v^{(d)}} \underbrace{\text{IFFT}\{X_{\mathcal{V}_v}\}}_{x_{n/L,v}},
\end{aligned} \tag{4.8}$$

where $d \in \{0, 1, ..., D-1\}$. Finally, the transmitted signal $x_{n/L}^{(\bar{d})}$ is chosen according to (4.5) similar to the SLM method.

The PTS method originally described in [76] is a special case of the technique we have described here. In [76], it is assumed that the phase parameters take on values from a finite set, $\mathcal{P}$, so that $\theta_v^{(d)} \in \mathcal{P}$. Next, every possible set of phase combinations is tested to find the combination that produces that lowest PAR sequence. Thus, for traditional PTS, $D = V^{|\mathcal{P}|}$. The only modification we have made is to allow non-exhaustive searches over the phase sequence space so that $D \leq V^{|\mathcal{P}|}$. A similar development was used in [75] by the authors of [75].

In (4.8), a total of V length-NL IFFTs are performed, regardless of the size of D. The small number of IFFTs (V as opposed to D, assuming $V < D$) relative to SLM was one main justification for proposing PTS [76]. However, as we will show in Section IV, the number of IFFTs should not be the only complexity consideration since the length-NL multiplications and additions necessary to create $x_{n/L}^{d}$ in (4.8) can contribute significantly to the overall complexity of PTS.

From (4.8) it is apparent that SLM can be regarded as a special case of PTS where
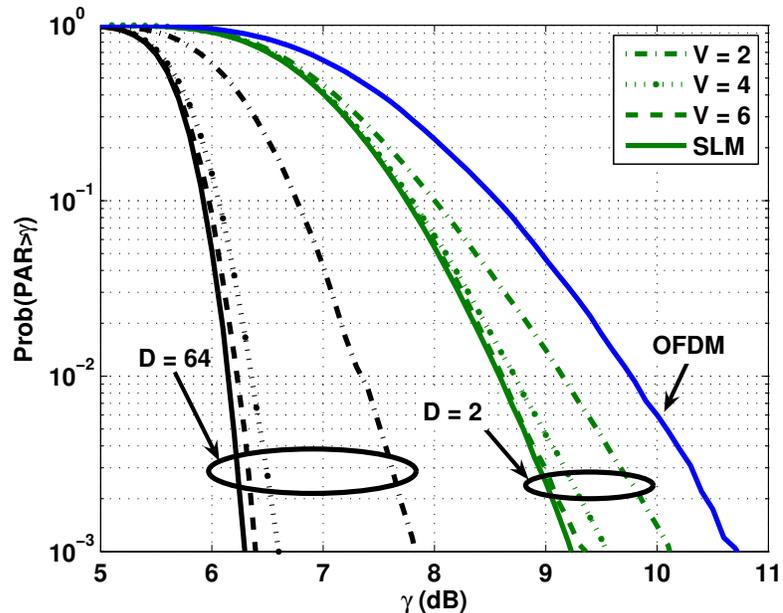
Figure 4.1: Plot of the CCDF of the PAR for SLM and PTS with $L = 4$.

each sub-block contains only one subcarrier (e.g. $\mathcal{V}_v = v|_{v \in [0, N-1]}$). In analyzing the PAR-minimizing values of $\theta_v^{(d)}$, it is convenient to view PTS as a special case of SLM where the SLM phases are constant over each sub-block, i.e. $\phi_{\mathcal{V}_v}^{(d)} = \theta_v^{(d)}$. Recall from [128] that if $\phi_k^{(d)}$ are realizations of an i.i.d. random variable Φ with $\mathrm{E}[e^{j\Phi}] = 0$, then the corresponding PAR CCDF curve will be minimized. In PTS, the i.i.d. condition is violated for $V < N$. So PTS with $V \neq N$ will not be able to achieve as much PAR reduction as SLM for a given D. In order words, the result from [128] can be applied to PTS to prove that PTS will have worse PAR reduction performance than SLM for a given amount of side information. A similar conclusion, based on simulation results, was reached in [75] by the original authors of PTS.

Fig. 4.1 is a plot of the PAR CCDF for PTS and SLM when the oversampling factor is $L = 4$. The plot illustrates the PAR reduction degradation that PTS suffers when V is small. However, with V = 6, the PTS CCDF is quite close to its lower bound which is the SLM CCDF, achievable when $V = N$.

In addition to reducing the number of IFFTs, the other main justification for PTS is that it may be possible to find $\theta_v^{(\bar{d})}$ without having to search all D possibilities, thus reducing the amount of computation [76]. Many optimization methods have been proposed

[30, 99, 47]. However, some of them are misguided because they do not take into account the large amount of side information required to convey the optimized parameters $\theta_v^{(\bar{d})}$ to the receiver. That is, they perform a sub-optimal discrete optimization over a very large set $\theta_v^{(d)}$, from which they have to convey $\theta_v^{(\bar{d})}$ to the receiver.

In this chapter, we are interested in determining the PAR reduction capability per unit of computational complexity of PTS and SLM under a side information constraint. In order for the conclusions to not depend on a particular optimization method, we opt to analyze PTS using a set of phase constants that are i.i.d. random, where the PAR-minimizing set of phase constants is determined by exhaustive search. Performing an exhaustive search guarantees that $\theta_v^{(\bar{d})}$ will be the PAR-minimizing sequence among the set $\theta_v^{(d)}$, $d \in \{0, 1, ..., D-1\}$.

Two issues in PTS need to be discussed before analyzing its complexity. The first is whether it is possible to choose the values of $\theta_v^{(d)}$ such that the multiplication in (4.8) can be implemented with simple sign changes. It was shown in [51] that in order to use a blind maximum-likelihood receiver to detect $\bar{d}$, full-complexity complex multiplications are required. The other consideration is whether it is possible to choose the sets $\mathcal{V}_v$ so that the IFFT in (4.8) can be performed at a reduced complexity. It has been shown that the PAR minimizing choice for $\mathcal{V}_v$ is random equally-sized sub-blocks, which do not generally allow for a complexity reducing structure [53]. On the other hand, If the IFFT is designed especially for the specific set of PTS partitions, then it is possible to exploit the sparseness of $X_{\mathcal{V}_v}$ to reduce the complexity of IFFTs [12].

4.3   Computational Complexity

This section will outline the computational complexity involved in SLM and PTS. We will assume that $\theta_v^{(0)} = 0$ and that $\phi_k^{(0)} = 0$, i.e. the first of D signal mappings is just the original OFDM symbol.

For SLM, as indicated in (4.3), $N(D-1)$ complex multiplications are required to create $X_k^{(d)}$, $d \in \{0, 1, ..., D-1\}$. Next, D length-NL IFFTs are needed to generate $x_{n/L}^{(d)}$, $d \in \{0, 1, ..., D-1\}$. Each oversampled IFFT requires $NL/2 \log N + NL/2$ complex multiplications and $NL \log N$ complex additions (all logarithms are base 2, i.e. $\log N \triangleq \log_2 N$)

Table 4.1: Number of real operations for SLM and PTS

SLM additions (A_{SLM})	$DNL(3\log N + 2) + 2N(D-1)$
SLM multiplications (M_{SLM})	$2DNL(\log N + 2) + 4N(D-1)$
PTS additions (A_{PTS})	$4(D-1/2)NLV - DNL + VA_{IFFT}$
PTS multiplications (M_{PTS})	$4(D-1)NLV + 2DNL + VM_{IFFT}$

[115]. Finally, $|x_{n/L}^{(d)}|^2$ must be calculated at each n to determine the PAR which comes at the expense of $2DLN$ real multiplications and DLN real additions.

In (4.8), the generation of a PTS symbol requires V length-NL oversampled IFFTs to create $x_{v/L,v}$. To make the comparison fair, we assume that each IFFT is especially designed to exploit the sparseness of $X_{\mathcal{V}_v}$. With this assumption we can calculate the mean[2] number of multiplications and additions required for each IFFT in terms of the sparseness of $X_{\mathcal{V}_v}$ [12]. In the context of PTS, the sparseness of $X_{\mathcal{V}_v}$ is the proportion of its entries that are non-zero, which is $1/V$. According to (4.8), $VNL(D-1)$ complex multiplications are needed to create $e^{j\theta_v^{(d)}} x_{v/L,v}$, $d \in \{0, 1, ..., D-1\}$, which are combined through $(V-1)NLD$ complex additions to generate $x_{n/L}^{(d)}$. Finally, just as in SLM, the cost of calculating the PAR$\{x_{n/L}^{(d)}\}$, $d \in \{0, 1, ..., D-1\}$, is $2DLN$ real multiplications and DLN real additions.

In general, a complex multiplication takes four real multiplications and two real additions. On the other hand, a complex addition requires two real additions. In Table 4.1, we have summarized the computational requirement of each scheme, where A_{IFFT} and M_{IFFT} are the number of real additions and real multiplication required for each sparse PTS IFFT.

The complexity of PTS and SLM is quantified through a parameter f that is the number of addition instructions required for each multiplication operation. So the overall complexity

---

[2]The mean complexity in [12] is averaged over all possible input vectors with the specified sparseness. As a point of reference, a 256-point IFFT of a 25% non-zero vector requires 78% as many complex multiplications and 70% as many complex additions as a full 256-point IFFT.
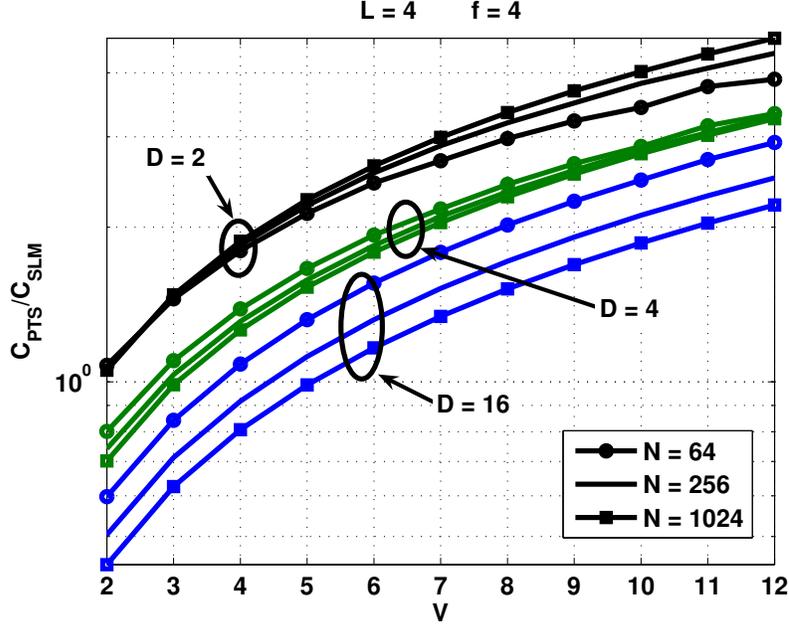
Figure 4.2: Plot of C_{PTS}/C_{SLM} versus the number of PTS partitions V for $L = 4$.

is

$$C_{SLM} = A_{SLM} + fM_{SLM}$$

$$C_{PTS} = A_{PTS} + fM_{PTS},$$

where A_{SLM}, M_{SLM}, A_{PTS} and M_{PTS} are defined in Table 4.1.

Fig. 4.2 is a plot of the ratio C_{PTS}/C_{SLM} versus the number of PTS partitions V. The plot contains lines for $N = \{64, 256, 1024\}$ and $D = \{2, 4, 16\}$ with $L = 4$ and $f = 4$. Note that Fig. 4.2 shows that the ratio is monotonically increasing in V. The point of utmost interest is where the lines cross $C_{PTS}/C_{SLM} = 1$. For $C_{PTS}/C_{SLM} > 1$, PTS is more computationally complex, whereas, when $C_{PTS}/C_{SLM} < 1$ SLM is more complex. The plot shows that when $D = 2$, PTS is always more complex. Even for a large value $D = 16$, SLM is less complex than PTS when $V > 5$. These are surprising results considering that PTS was designed to have a *lower* complexity than SLM.

4.4 SLM/PTS Comparison

From the PAR CCDF-minimizing criteria outlined in [128], we infer that SLM will result in a lower PAR than PTS for a given number of mappings D; this is empirically demonstrated

in Fig. 4.1. With Fig. 4.2, we can see that large values of V lead to increased computational complexity for PTS. Together, these two observations imply that PTS will be inferior to SLM in complexity and in PAR reduction capability for all values of V that cause $C_{PTS}/C_{SLM} > 1$.

The next question is: should SLM be used over PTS when V is so small that $C_{PTS}/C_{SLM} \leq 1$? To make this comparison, we must first find some metric that quantifies the performance of each PAR reduction scheme. The most obvious candidate is the PAR at a predetermined CCDF level. But such a metric is sensitive to the probability level chosen. Also, the PAR at a certain probability level does not translate in any obvious way to a meaningful system metric like bit error rate or PA power efficiency. Instead, we advocate three separate metrics all of which have a more tangible meaning than the PAR at a certain probability level.

To simplify the analysis we assume a soft clipping operation or the so-called ideal linear (or linearized) PA defined by

$$
g_{clip}(x) = \begin{cases} x, & |x| \leq A \\ Ae^{j\angle x}, & |x| > A. \end{cases} \tag{4.9}
$$

A popular linearization technique for PAs is called predistortion [91]. With predistortion, it is possible to realize an overall PA response that resembles (4.9).

4.4.1 Power Efficiency-Based Metric

The first metric we are going to introduce assumes a system where each OFDM symbol is scaled digitally by a factor $\sqrt{\alpha}$ before being sent to the PA [79]. Such a scaling operation appears as flat fading to the receiver and can be thought of as part of the multipath channel. The scaling factor is chosen so that the peak power of the transmitted symbol $x_{n/L}^{(\bar{d})}$ is exactly equal to A^2. With this definition,

$$
\alpha = \frac{A^2}{\max_{0 \leq n \leq NL-1} |x_{n/L}^{(\bar{d})}|^2}. \tag{4.10}
$$

The average symbol power can be shown to be proportional to $\mathrm{E}\left[1/\mathrm{PAR}\left\{x_{n/L}^{(\bar{d})}\right\}\right]$. Also, from [33], we can express the mean power efficiency, η of a class A power amplifier using

$$
\eta = \mathrm{E}\left[\frac{1}{2PAR}\right]. \tag{4.11}
$$

Accordingly, we will use this metric to quantify the performance of PTS and SLM when the minimum PAR criterion is implemented.

Fig. 4.3 is a plot of the class A PA power efficiency, η, versus the complexity for PTS with $V = \{2, 3, 4\}$ and for SLM, where $N = \{64, 256\}$. As a point of reference, assuming $L = 4$ and $f = 4$, conventional OFDM with $N = 64$ subcarriers or $N = 256$ subcarriers has complexity $C \approx 2 \cdot 10^4$ and $C \approx 10^5$, respectively. When $D = 32$, the SLM complexity numbers are $C_{SLM} \approx 7 \cdot 10^5$ and $C_{SLM} \approx 3 \cdot 10^6$ respectively for 64-subcarrier and 256-subcarrier SLM OFDM.

The plot shows that the performance of PTS is sensitive to the number of partitions V. There is not a single choice of V that is optimal over the entire complexity range so V should be chosen so that η is maximized for the complexity value of interest.

For both $N = 64$ and $N = 256$, there is no single value of V that is is better than the other values of V across all of complexity values shown in Fig. 4.3. However, since we have the freedom of choosing the number of partitions V in PTS, we can select the best V for each allowed complexity value. For $N = 64$, if no more than $5 \cdot 10^4$ complexity is allowed, then the best choice is $V = 2$ because it maximizes efficiency. Similarly, if no more than $5 \cdot 10^5$ complexity is allowed when $N = 256$, then $V = 2$ is also the best choice. In any case, even when V is optimized for maximum efficiency, SLM will outperform PTS. However, the trends in Fig. 4.3 show that the higher the allowed complexity, the less the difference is between η for PTS and SLM. For practical levels of complexity, SLM tends to be a significantly better choice than PTS.

4.4.2   Clipping Power-Based Metric

In using η as the performance metric, we assumed that each symbol is scaled to maximally utilize the linear range of the PA. For high PAR signals, this assumption may lead to an unacceptably low SNR. One solution is to assume that some part of the signal will be clipped by the predistorter/PA soft limiter. By anticipating the irreversible clipping distortion that will be introduced, it is possible to reformulate the SLM and PTS selection criterion to mitigate the effect of the distortion. The reformulation would mean that the
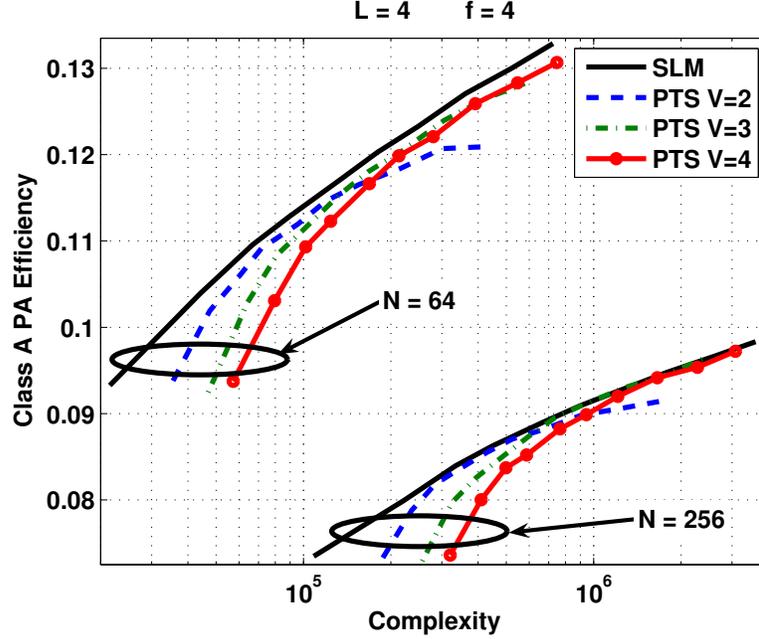
Figure 4.3: Plot of η versus the complexity (C_{PTS} or C_{SLM}). Each line in the plot contains 32 points corresponding to the set of $D \in \{1, ..., 32\}$.

signal that produces the lowest power distortion among the D alternatives $\{x_{n/L}^{(d)}\}_{d=0}^{D-1}$ is transmitted. This differs from conventional SLM and PTS where the signal with the lowest PAR is selected for transmission. Stated precisely, the index of the transmitted signal $x_{n/L}^{(\tilde{d})}$ is selected according to

$$\widetilde{d} = \underset{0 \leq d \leq D-1}{\arg \min} \sum_{n=0}^{NL-1} \left| x_{n/L}^{(d)} - g_{clip}(x_{n/L}^{(d)}) \right|^2 . \tag{4.12}$$

Similar SLM metrics have been presented in [64, 59]. Note that the blind detection techniques used to recover $\widetilde{d}$ described in [51, 15] will still be applicable for $\widetilde{d}$ recovery regardless of the selection criterion. Therefore, no blind receiver modification would be necessary to accommodate the selection criterion in (4.12).

There are two main reasons to select the transmitted signal based on minimum distortion noise, the first is to limit the amount of inband distortion, which leads to bit errors. The second is to limit the amount of spectral regrowth. We will show in the next section that a better selection criteria exists for limiting the number of bit errors; however the minimum distortion metric is excellent at reducing the amount of spectral regrowth.

The spectral regrowth can be quantified through a popular metric known as the adjacent

channel leakage ratio (ACLR). Define the frequency domain of the clipped signal to be

$$\bar{X}_k^{(d)} = \frac{1}{\sqrt{LN}} \sum_{n=0}^{NL-1} g_{clip}\left(x_{n/L}^{(d)}\right) e^{\frac{-j2\pi kn}{LN}}, \tag{4.13}$$

where $k \in \{0, 1, ..., LN-1\}$. Define the set of adjacent channel subcarriers $\mathcal{A} = \{N/2, N/2 + 1, ..., N-1, LN-N, LN-N, ..., LN-1-N/2\}$ and the set of in-band subcarriers $\mathcal{I} = \{0, 1, ..., N/2-1, LN-N/2, LN-N/2+1, ...LN-1\}$. Thus,

$$ACLR = \frac{\mathrm{E}\left[\sum_{k \in \mathcal{A}} |\bar{X}_k^{(\tilde{d})}|^2\right]}{\mathrm{E}\left[\sum_{k \in \mathcal{I}} |\bar{X}_k^{(\tilde{d})}|^2\right]}, \tag{4.14}$$

which is a measure of how much distortion power from the inband signal "leaks" in to the adjacent frequency bands.

Fig. 4.4 is a plot of the ACLR versus the complexity for PTS with $V = \{2, 3, 4\}$ and for SLM, where $N = \{64, 256\}$, and with $1 \leq D \leq 32$. The complexity for PTS and SLM using the section criterion in (4.12) are slightly different from the complexity calculations formulated in Section IV. Namely, $(2N-1)LD$ more real additions are necessary. To create the plot, the clipping level was set so that $A/\sigma_x = 4$dB, where σ_x^2 is the variance of X_k. As with the power efficiency metric in Section IV.A, the performance of PTS depends on the choice of V. For the best performance, V should be selected so that the ACLR is minimized at the complexity level of interest. The plot shows that SLM slightly outperforms PTS even when the minimizing V is selected.

4.4.3 Intermodulation Distortion-Based Metric

In [95, 96, 97], a case was made for selecting the transmitted symbol based on the worst case intermodulation distortion (IMD) power. For justification, those papers showed that the BER induced by clipping is dominated by the subcarrier with the largest IMD. Here we define the IMD E_k in the kth subcarrier as

$$E_k^{(d)} = X_k^{(d)} - \bar{X}_{k \in \mathcal{I}}^{(d)}, \tag{4.15}$$

where $\bar{X}_k^{(d)}$ is defined in (4.13). With this, the index of the transmitted signal $x_{n/L}^{(\check{d})}$ is selected according to

$$\check{d} = \underset{0 \leq d \leq D-1}{\arg\min} \left(\max_{0 \leq k \leq N-1} \left|E_k^{(d)}\right|\right), \tag{4.16}$$
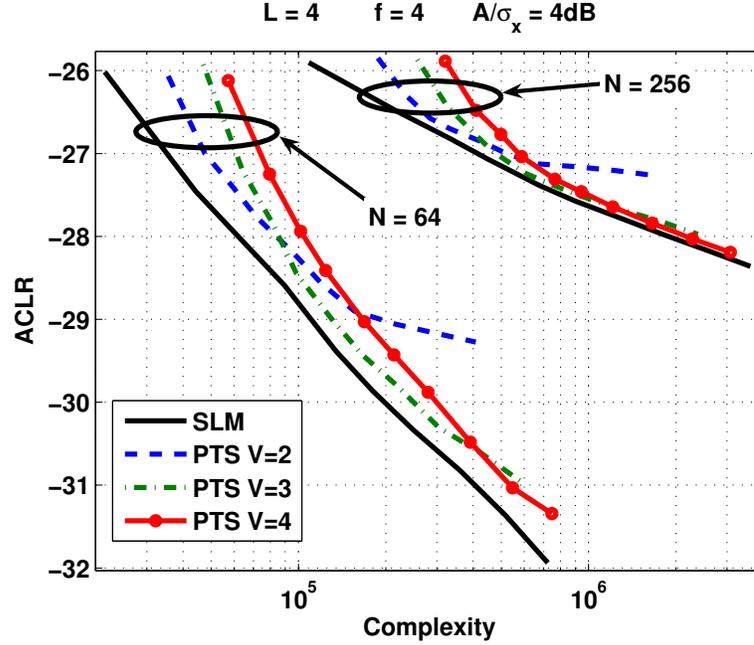
Figure 4.4: Plot of the ACLR in decibel scale versus the complexity (C_{PTS} or C_{SLM}). Each line in the plot contains 32 points corresponding to the set of $D \in \{1, 2, ..., 32\}$.

which can be recovered blindly without any modification to the blind receivers described in [51, 15]. As noted in [97], this selection criterion requires additional computational complexity over the conventional minimum PAR selection criterion in (4.5). Specifically, the additional computational complexity is D FFT operations and NLD complex additions. To compare the performance of SLM and PTS when both schemes use an IMD-based selection criteria, we suggest that BER be used.

Fig. 4.5 and Fig. 4.6 are plots of the BER versus the complexity for PTS with $V = \{2, 3, 4\}$ and for SLM, where $N = \{64, 256\}$, and with $1 \le D \le 32$. The BER is calculated assuming that X_k is drawn from a QPSK constellation. Also, a noiseless Rayleigh fading channel, where the receiver has perfect channel state information, is assumed so that the received signal is $H_k(X_k^{(\breve{d})} + E_k^{(\breve{d})})$. Here, H_k has a complex Gaussian distribution with zero mean and variance one (i.e. $H_k \sim \mathcal{CN}(0, 1)$). Finally, it is assumed that $\breve{d}$ is detected without error.

To create the plots two different clipping levels were used $A/\sigma_x = 4$dB and $A/\sigma_x = 6$dB, where σ_x^2 is the variance of X_k. For the 4dB clipping level, the BER may be too low
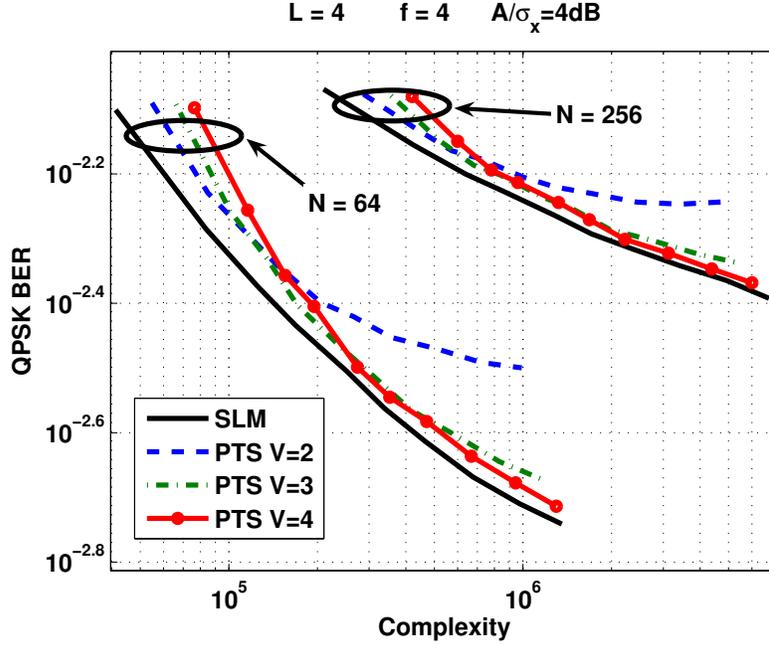
Figure 4.5: Plot of QPSK BER versus the complexity (C_{PTS} or C_{SLM}), with a clipping level of 4dB. Each line in the plot contains 32 points corresponding to the set of $D \in \{1, 2, ..., 32\}$.

for practical applications. However, the 6dB clipping does achieve an adequate BER for practical systems.

The plot shows that it is beneficial to select V so that, at the complexity level of interest, the BER is minimized. The figure also illustrates that, for all of the values plotted, SLM has better BER performance than PTS regardless of the number of PTS partitions employed. The difference is particularly pronounced for the $N = 64$, $A/\sigma_x = 6$dB case where SLM significantly outperforms PTS.
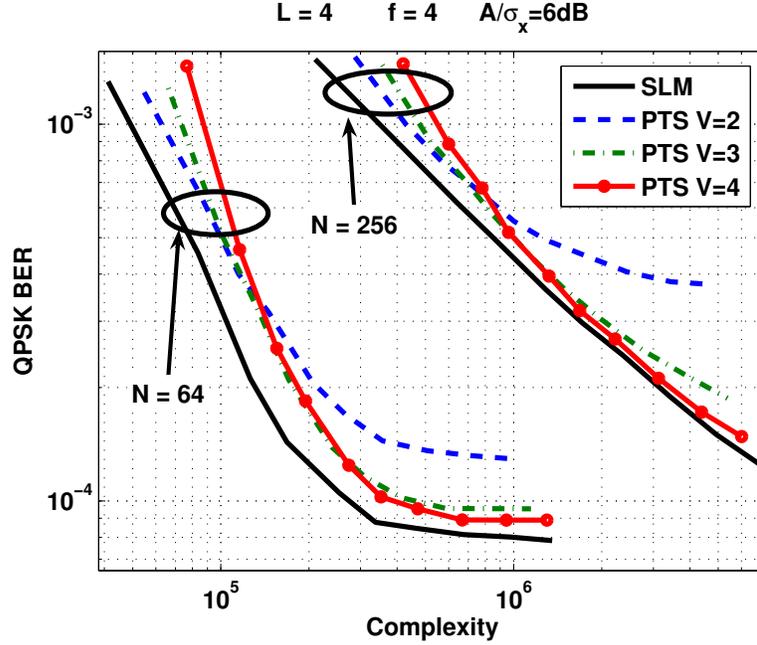
Figure 4.6: Plot of QPSK BER versus the complexity (C_{PTS} or C_{SLM}), with a clipping level of 6dB. Each line in the plot contains 32 points corresponding to the set of $D \in \{1, 2, ..., 32\}$.

4.5 Conclusions

In this chapter we focused on two popular distortionless PAR reduction techniques, namely PTS and SLM and analyzed their computational complexity and resulting PAR reduction performance. It was already known that SLM can produce multiple time-domain signals that are asymptotically independent, while the alternative signals generated by PTS are interdependent. This interdependency necessarily implies that PTS will have some PAR reduction capability degradation compared to SLM for a given number of mappings. However, it has been assumed in [75] that the computational complexity of PTS would be much less than that of SLM so that the computational savings of PTS would outweigh the PAR reduction advantages of SLM.

Surprisingly, we found that SLM is actually less computational complex than PTS when more than a couple of PTS partitions are used. In order to compare PTS and SLM we used three different selection criteria and, correspondingly, three different metrics. The results showed, for a given amount of computational complexity, SLM performs better than PTS in all three metrics. Even PTS with an optimized V does not beat the performance of

SLM in any of the metrics across all complexities. In summary, SLM is preferred to PTS because (i) SLM is conceptually simpler; (ii) SLM does not require any off-line complexity optimization with respect to V as would be recommended for PTS; (iii) SLM performs better than *optimized* PTS.

COMPUTATIONAL COMPLEXITY ANALYSIS OF FFT PRUNING -
A MARKOV MODELING APPROACH

5.1 Abstract

The Fourier transform is instrumental in many signal processing applications such as digital filtering, spectral analysis and communications. In 1965, Cooley and Tukey demonstrated that the discrete Fourier transform (DFT) can be computed using the fast Fourier transform (FFT) algorithm with reduced computational complexity. When the input vector to the FFT contains mostly zeros (i.e., is sparse), it is possible to realize computational savings over a full FFT by only performing the arithmetic operations on non-zero elements. That is, the FFT is "pruned" so that only the useful computations are performed. In this chapter, we derive the (non-stationary) Markov process that describes the number of occupied (i.e. non-zero) paths at each stage of a pruned FFT. With the probability distribution of the number of non-zero paths at each FFT stage, we then determine the probability distribution of the number of multiplications and additions necessary to compute the FFT of an input vector with a given sparsity distribution.

5.2 Introduction

The Fourier transform is instrumental in many signal processing applications such as digital filtering, spectral analysis and communications[1]. In [32], Cooley and Tukey demonstrated that the discrete Fourier transform (DFT) can be computed using the fast Fourier transform (FFT) algorithm, which reduces the computational complexity of an N-point DFT from $\mathcal{O}(N^2)$ to $\mathcal{O}(N \log N)$, where the base of the logarithm is the radix of the FFT. However, there are some applications where the input vector to the FFT, $\{x[n]\}_{n=0}^{N-1}$, has a relatively

---

[1]Part of this chapter was presented in R. J. Baxley and G. T. Zhou, "Computational complexity analysis of FFT pruning - A Markov modeling approach," Proc. IEEE 12th Digital Signal Processing Workshop, pp. 535-539, Grand Teton National Park, WY, September 2006. Reference [12]

small number of non-zero values. For example, signal interpolation can be performed using an "oversampled" FFT, where the FFT of a vector padded with a block of M zeros is encountered.

When the input vector to the FFT is sparse, it is possible to realize computational savings over a full FFT by only performing the arithmetic operations on non-zero elements. Equivalently, this can be thought of as "pruning" the zero paths in the FFT flow graph. FFT pruning was first studied in [68] and several algorithms have been proposed to implement pruned FFTs [68, 77, 106, 107, 94, 93]. However, most of these algorithms and analyses are based on pruned FFTs where the zeros in the input vector are contiguous.

There are applications which require the FFT of unstructured sparse vectors. That is, the input vector to the FFT will contain a large number of zeros that are not organized in any systematic way. The FFT of a sparse vector is called an input-pruned FFT. Conversely, the FFT of a full vector where only several output values need to be calculated is called an output-pruned FFT [68]. Input- and output-pruned FFTs occur in diverse applications including crest factor reduction in multicarrier communications [76], cognitive radio [45] and genetic sequence alignment applications [49].

Fig. 5.1 is a flow graph of an example input-pruned FFT, where the input vector contains only two non-zero values $x[4]$ and $x[13]$. The bold paths in the flow graph indicate the paths that need to be considered in the calculation of the FFT output. The paths with a power of $W = e^{-j2\pi/N}$, $j = \sqrt{-1}$, above them indicate that a complex multiplication is required to compute the value of that path. Also, the bold paths that terminate in a filled circle indicate that an addition is necessary to compute the value at the end of that stage, whereas an empty bold circle indicates that the value at the end of that stage is simply a copy or a sign-reversed copy of a value at the beginning of the stage. That is, the bold circles indicate an addition is necessary and the empty bold circles indicate that no arithmetic operation is necessary. With this, Fig. 5.1 shows that multiplications [2] are only necessary at stages one and three, while additions are only necessary at stage three.

---

[2]Since a complex sign change can be implemented with a two bit flipping operations we do not take into account sign changes in our complexity analysis.
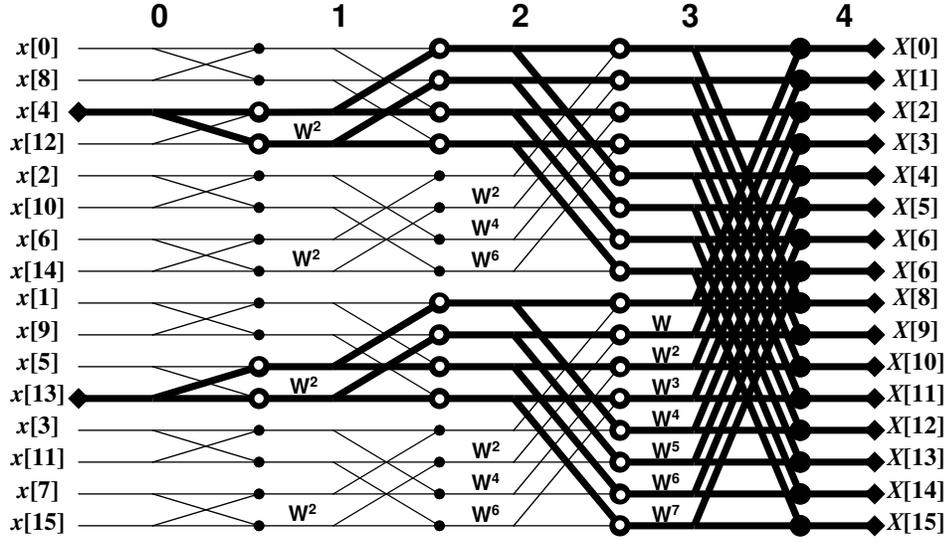
Figure 5.1: Signal flow graph for an input-pruned FFT ($N = 16$).

In [49] upper and lower bounds on the number of butterfly computations required to compute the FFT of an arbitrarily sparse input vector were given, where one butterfly operation requires the computation of one multiplication and two additions. Those complexity bounds were derived assuming that the proportion of non-zero entries was known (i.e. the input vector density), but that the positions of these non-zero input bins were random. Specifically, in [49] the bounds were justified by counting the most and least possible number of occupied butterflies for a given input vector density.

In this chapter, we are interested in finding a more precise characterization of the number of multiplications and additions required to compute an input-pruned FFT. Instead of bounding the number of occupied butterflies at each FFT stage, we derive the Markov process that describes the number of occupied (i.e. non-zero) paths at each FFT stage for a given input vector density.

In basing our complexity analysis on the number of occupied paths instead of the number of occupied butterflies we are able to derive a more precise estimate of the number of multiplications and additions required to compute the pruned FFT. By only examining the number of occupied butterflies, the analysis in [49] is unable to distinguish between butterflies that require full complexity (i.e. one multiplication and two additions) and butterflies that require no computation (i.e. a half filled butterfly whose single non-zero

64

element is not on the multiplied half of the butterfly). Thus, the butterfly-based complexity analysis in [49] has slightly less resolution than our path-based analysis.

With the probability distribution of the number of non-zero paths at each FFT stage, we can determine the probability distribution of the number of multiplications and additions for an FFT with a given sparseness. From these distributions, we can gain valuable insights into the computational complexity required to compute a pruned FFT.

In the next section we will explain our procedure for deriving the Markov model that describes the number of paths in each stage. In Section III, we derive the conditional distributions for the number of additions and multiplications required at each stage given the number of paths occupied at the beginning of the stage. In Section IV, we show how the stage-wise conditional distributions can be used to determine the pdf of the total number of additions and multiplications required to compute a pruned FFT with a given input vector sparseness. Finally, we verify our results in Section V by comparing them with Monte Carlo simulations.

Notational summary:

$Q^{(k)}$	Number of occupied paths at stage k
$A^{(k)}$	Number of additions at stage k
$M^{(k)}$	Number of multiplications at stage k
$x_{i,s}^{(k)}$	Entry in row i, column s of the matrix $\boldsymbol{X}^{(k)}$

5.3 *Markov model for path propagation*

Our approach to determining the complexity of a pruned FFT is based on modeling the number of non-zero paths at each stage of the FFT. Then, using this model, we derive the number of arithmetic operations (i.e. additions and multiplications) at each stage, and finally by adding the results of each stage together we determine the distribution of the number of operations for the entire pruned FFT. In this section we outline the procedure for determining the Markov model that describes the number of non-zero paths at each FFT stage. We will first show a few simple examples and then use inductive reasoning to extrapolate to a more general case. For purposes of simplicity, we will consider the radix-2

FFT in the remainder of the chapter.

At any stage k, the number of occupied paths at the beginning of that stage, $Q^{(k)}$, can take on values from 1 to N. In order to construct the transition matrix from stage zero to stage one let us look at some particular cases. If $Q^{(0)} = 1$, then the only possibility for the number of paths at stage $k = 1$, $Q^{(1)}$, is $Q^{(1)} = 2$. To clarify, $Q^{(k)}$ describes the number of occupied paths, but does not contain any information about where these are. Since there is only one occupied path, knowing the butterfly structure of the FFT, we can easily conclude that the second stage of the FFT will contain exactly two occupied paths.

If, on the other hand, $Q^{(0)} = 2$, then there are two cases to consider. The first is when both of the non-zero entries occupy the same butterfly, which can happen in $\binom{N/2}{1}$ different ways. In this case, the values from each of the two paths will be linearly combined to produce exactly two occupied paths in the second stage, i.e. $Q^{(1)} = 2$. If, however, both non-zero entries are on different butterflies, then each will be paired with a zero path and $Q^{(1)} = 4$. There are $\binom{N}{2}$ ways to choose two paths among the N possible paths, $\binom{N/2}{2}$ way to choose the two butterflies and 2^2 ways to arrange the non-zero paths amongst the two chosen butterflies. Thus,

$$\Pr(Q^{(1)} = 2|Q^{(0)} = 2) = \frac{\binom{N/2}{1}}{\binom{N}{2}}$$

$$\Pr(Q^{(1)} = 4|Q^{(0)} = 2) = \frac{\binom{N/2}{2}2^2}{\binom{N}{2}}.$$

Notice that these are the only two possibilities when $Q^{(0)} = 2$. As a matter of fact, the number of output paths will always be at least as large as the number of input paths. Furthermore, the difference $Q^{(k)} - Q^{(k-1)}$ will either be zero or will be divisible by 2^k.

By combining these observations the probability transition matrix for the number of non-zero paths from stage $k - 1$ to stage k is

$$\begin{aligned}
p_{i,s}^{(k)} &= \Pr\left(Q^{(k)} = 2^k s \middle| Q^{(k-1)} = 2^{k-1} i\right) \\
&= \begin{cases} \binom{N2^{1-k}}{i}^{-1}\binom{N2^{-k}}{i-s}\binom{N2^{-k}-i+s}{2s-i}2^{2s-i}, & \Omega \\ 0, & \text{else,} \end{cases} \\
&\triangleq \boldsymbol{P}^{(k)},
\end{aligned} \tag{5.1}$$

where $\Omega = \{1 \leq s \leq 2^{-k}N, \ s \leq i \leq 2s, \ 1 \leq k \leq \log_2 N\}$ is the set of non-zero entries in the matrix $\boldsymbol{P}^{(k)}$. Notice that $\boldsymbol{P}^{(k)} \in \mathbb{R}^{N2^{1-k} \times N2^{-k}}$ is a tall stochastic matrix. The matrix is tall because the possibilities for the number of occupied paths is halved from one stage to the next.

5.4 Conditional number of Additions and multiplications

From the butterfly structure, we can see that half of the paths are multiplied by a power of

$$W = e^{-j2\pi k/N}. \tag{5.2}$$

But when $k = 0$ no multiplication is necessary. Therefore, we only consider the multiplications with $\{W^k\}_{k=1}^{N/2-1}$ in the following complexity analysis. Also, since we assume that the positions of the non-zero input paths are uniformly distributed, then the blocks of non-zero paths at each stage are also uniformly distributed.

In order to derive the distribution of the number of multiplications conditioned on the number of input paths at the start of stage $k-1$, it is convenient to start by also conditioning on the number of paths at the start of stage k. By doing this, we can see that the number of multiplications with these conditions follows a binomial distribution. Specifically, we have the probability of the number of multiplications in stage $k-1$ conditioned on the number of paths in stage k and stage $k-1$ is

$$
\Pr\left(M^{(k-1)} = \left(\mu + i - s\right)\left(2^{k-1} - 1\right) \middle| Q^{(k)} = 2^k s, \ Q^{(k-1)} = 2^{k-1}i \right)
$$
$$
= \begin{cases} 2^{i-2s}\binom{2s-i}{\mu}, & 1 \leq s \leq 2^{-k}N, \ s \leq i \leq 2s, \\ & 2 \leq k \leq \log_2 N, \ 0 \leq \mu \leq 2s - i \quad (5.3) \\ 0, & \text{else}. \end{cases}
$$

Next we can use the law of total probabilities to get

$$
\begin{aligned}
c_{i,\mu}^{(k-1)} &= \Pr\left(M^{(k-1)} = (\mu + i - s)\left(2^{k-1} - 1\right) \,\middle|\, Q^{(k-1)} = 2^{k-1}i \right) \\
&= \sum_{s=1}^{N2^{-k}} \Pr\left(M^{(k-1)} = (\mu + i - s)\left(2^{k-1} - 1\right) \,\middle|\, Q^{(k)} = 2^k s,\ Q^{(k-1)} = 2^{k-1}i \right) p_{i,s}^{(k)} \\
&= \sum_{s=1}^{N2^{-k}} \frac{\binom{N2^{-k}}{i-s}\binom{N2^{-k}-i+s}{2s-i}\binom{2s-i}{\mu}}{\binom{N2^{1-k}}{i}} \\
&\triangleq \boldsymbol{C}^{(k-1)}.
\end{aligned}
\tag{5.4}
$$

Now, let us proceed to find the distribution of the number of additions. To do this we first derive the distribution of the number of additions in stage $k-1$ conditioned on the number of paths in stages $k-1$ and k. Finding this conditional distribution is straightforward because the number of additions is deterministic when the number of paths in stage $k-1$ and k are specified. Once we derive the conditional distribution we can use (5.1) and the law of total probabilities to find the number of additions in stage $k-1$ conditioned only on the number of paths in stage $k-1$. The conditional probability distribution on the number of additions in stage k, $A^{(k)}$, is

$$
\Pr\left(A^{(k)} = 2^k \alpha \,\middle|\, Q^{(k)} = 2^k s,\ Q^{(k-1)} = 2^{k-1}i \right) =
\begin{cases}
1, & \Omega,\ \alpha = i - s \\
0, & \text{else},
\end{cases}
\tag{5.5}
$$

where $\Omega = \{ 1 \le s \le 2^{-k}N,\ s \le i \le 2s,\ 1 \le k \le \log_2 N \}$, as defined in (5.1). Now using the law of total probabilities,

$$
\begin{aligned}
b_{i,\alpha}^{(k)} &= \Pr\left(A^{(k)} = 2^k \alpha \,\middle|\, Q^{(k-1)} = 2^{k-1}i \right) \\
&= \sum_{s=1}^{N2^{-k}} \Pr\left(A^{(k)} = 2^k \alpha \,\middle|\, Q^{(k)} = 2^k s,\ Q^{(k-1)} = 2^{k-1}i \right) p_{i,s}^{(k)} \\
&= p_{i,(i-\alpha)}^{(k)} \\
&\triangleq \boldsymbol{B}^{(k)},
\end{aligned}
\tag{5.6}
$$

where $1 \le k \le \log_2 N,\ 0 \le \alpha \le 2^{-k}N,\ \max(1, 2\alpha) \le i \le N2^{-k}$. In other words, $\boldsymbol{B}^{(k)}$ is just a permuted version of $\boldsymbol{P}^{(k)}$, in (5.1).

68

5.5 Distribution of additions and multiplications for a pruned FFT

From Markov theory, the probability transition matrix for the number of non-zero paths in stage k given $Q^{(0)}$ is

$$
\begin{aligned}
t_{i,s}^{(k)} &= \Pr\left(Q^{(k)} = 2^k s \Big| Q^{(0)} = i\right) \\
&= \prod_{d=1}^{k} \boldsymbol{P}^{(d)}.
\end{aligned}
\tag{5.7}
$$

With the cumulative transition matrix $\boldsymbol{T}^{(k)}$ from (5.8) and the law of total probabilities, we can write the probability distribution for the number of multiplications conditioned on the input vector sparseness (i.e. $Q^{(0)}$) as

$$
\Pr\left(M^{(k)} = (\mu + i - s)\left(2^k - 1\right) \Big| Q^{(0)} = i\right) = \boldsymbol{T}^{(k)} \boldsymbol{C}^{(k)},
$$

for $1 \le k \le \log_2 N - 1$. Finally, to find the total number of multiplications, we have to find the distribution of $\sum_{k=1}^{\log_2 N - 1} M^{(k)}$, which can be done through the row-wise multiple convolution of $\boldsymbol{T}^{(k)} \boldsymbol{M}^{(k)}$. Specifically we have

$$
\begin{aligned}
\Pr\left(\sum_{k=1}^{\log_2 N - 1} M^{(k)} = \Psi_s \Big| Q^{(0)} = i\right) &= \bigotimes_{k=1}^{\log_2 N - 1} \boldsymbol{T}^{(k)} \boldsymbol{C}^{(k)} \\
&\triangleq y_{i,s},
\end{aligned}
\tag{5.8}
$$

where $\bigotimes$ is the multiple row-wise convolution operator and Ψ_s is the sth entry of the set containing all possible values of $\sum_{k=1}^{\log_2 N - 1} M^{(k)}$.

Finding the distribution of the number of additions is more difficult because the distribution of the number of additions is not Markovian. That is,

$$
\Pr\left(A^{(k)} = s \Big| A^{(k-1)} = i\right) \neq \Pr\left(A^{(k)} = s \Big| A^{(k-1)} = i,\ A^{(k-2)} = d\right).
$$

Nevertheless, we propose that an approximation to the distribution of the total number of additions can be made by assuming that the number of additions *is* Markovian. With this assumption we can write

$$
\begin{aligned}
\Pr\left(\sum_{k=1}^{\log_2 N} A^{(k)} = \Theta_s \Big| Q^{(0)} = i\right) &\approx \bigotimes_{k=1}^{\log_2 N} \boldsymbol{T}^{(k)} \boldsymbol{B}^{(k)} \\
&\triangleq x_{i,s},
\end{aligned}
\tag{5.9}
$$

where Θ_s is the sth entry of the set containing all possible values of $\sum_{k=1}^{\log_2 N} A^{(k)}$.
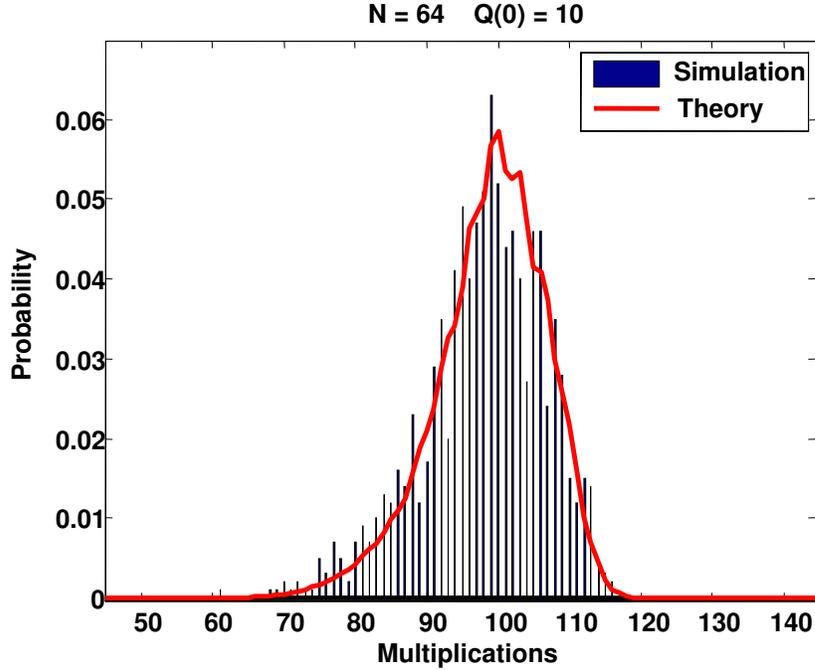
Figure 5.2: Experimental and theoretical pdfs of the total number of multiplications.

5.6 Simulation verification

In this section we will corroborate our theoretical findings through Monte Carlo simulation results. For our simulation we choose $N = 128$ and implemented a mock pruned FFT. At each level of sparseness (or, correspondingly, each $Q^{(0)}$) we ran 30,000 Monte Carlo simulations to find the distribution of the total number of additions and multiplications. We quantified the distributions through the first and second order centered moments.

Fig. 5.2 is a plot of the theoretical and simulated pdf of the number of multiplications for $N = 64$. the plot shows excellent agreement between the derived theoretical result and the simulated result.

Fig. 5.3 is a plot of the ratio of the mean number of additions for a given input vector sparseness to the number of additions required for a full FFT. Also plotted are the lines plus and minus one standard deviation from the mean. The plot verifies that our theoretical results, even with the simplifying assumption, match very closely to the simulation results. The mean seems to be exact (which is to be expected as Markovianess is not required) while the theoretical standard deviation is slightly larger than the empirical standard deviation.
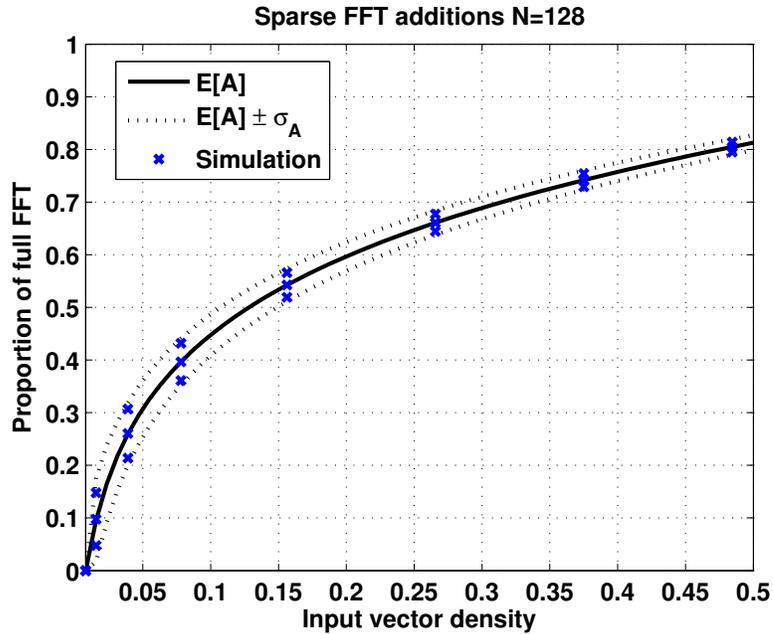
Figure 5.3: Proportion of the number of additions required at a given sparseness to the number of additions required for a full FFT.

Fig. 5.4 is similar to Fig. 5.3 except that it pertains to the number of multiplications instead of the number of additions. The plot shows that the simulation results closely match our theoretical results. By comparing the two plots we observe that the number of additions grows much more slowly with the input vector sparseness than does the number of multiplications. This implies that most of the computational savings realized by implementing a custom pruned FFT is gained through reducing the number of additions and not by reducing the number of multiplications.
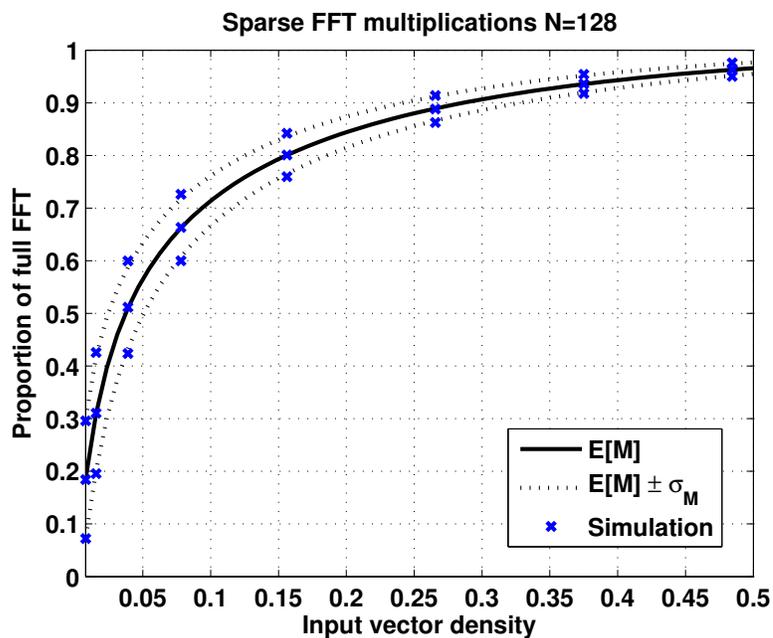
Figure 5.4: Proportion of the number of multiplications required at a given sparseness to the number of multiplications required for a full FFT.

5.7   Conclusions

In this chapter we have presented a method for determining the complexity of a pruned FFT. The proposed method is based on a Markov model of the number of occupied path at each FFT stage. This Markov path model, in conjunction with the conditional distribution of the number of multiplications and additions at each stage of the FFT, was then used to theoretically determine the total number of additions and multiplications necessary to compute a pruned FFT of a given sparseness. We verified our theoretical results through Monte Carlo simulations and showed that, despite a simplifying assumption in the derivation of the distribution of the number of additions, our results are very close to the simulated values.

CHAPTER VI

MAGNITUDE-SCALED SELECTED MAPPING: A CREST FACTOR REDUCTION SCHEME FOR OFDM WITHOUT SIDE INFORMATION

Selected mapping (SLM) is a popular distortionless crest factor reduction (CFR) method for orthogonal frequency division multiplexing (OFDM). With SLM, it is possible to reduce the peak-to-average power ratio (PAR) of an OFDM symbol by several decibels. In this chapter, we propose a method for SLM phase sequence detection that does not require side information transmission. The method, known as magnitude-scaled SLM, scales the frequency-domain power profile of the OFDM symbol with an envelope function. Using the envelope of the received symbol, the receiver can detect which phase sequence was transmitted. Also presented in this chapter are the theoretical characterizations of the detection error rate (DER) and symbol error rate (SER) in a magnitude-scaled SLM system. Compared with standard non-CFR OFDM, magnitude-scaled SLM can achieve an order of magnitude SER improvement in a peak-power-limited channel.

6.1 Introduction

Orthogonal frequency division multiplexing (OFDM) is an attractive multi-carrier transmission scheme due to its immunity to inter-symbol interference and robustness to multi-path fading[1]. It has been adopted by several communications standards, such as digital audio broadcasting (DAB), digital video broadcasting (DVB), wireless LAN and wireless MAN. However, one major problem associated with OFDM is its high peak-to-average power ratio (PAR) or crest factor (CF). When a high-PAR signal, such as OFDM, is passed through a high-power amplifier (HPA), the HPA will be required to operate in its non-linear region,

---

[1]Part of this chapter was presented in R. J. Baxley, C. Zhao and G. T. Zhou, "Magnitude-scaled selected mapping: A crest factor reduction scheme for OFDM without side-information transmission," *Proc. IEEE Intl. Conference on Acoustics, Speech, and Signal Processing*, pp. 373-376, Honolulu, Hawaii, April 2007. Reference [13].

which leads to both in-band and out-of-band distortions in the transmitted signal. Hence, crest factor reduction (CFR) of the OFDM signal is called for to improve the transmission quality.

Selected mapping (SLM), an effective and distortionless CFR method, selects the transmit sequence with the minimum PAR from a set of phase-rotated time-domain symbol vectors [7]. The index of the selected sequence should be correctly transmitted to the receiver as the side information to retrieve the corresponding phase vector for the de-rotation. Explicit side-information transmission will undesirably reduce the data rate, so a blind SLM (BSLM) scheme is preferred. Existing BSLM methods include maximum likelihood (ML) detection of the data symbols [51], maximum a posteriori (MAP) detection of the phase sequence [8], phase sequence detection based on pilot subcarriers [28], and phase sequence detection based on constellation shifts [83].

The magnitude-scaled SLM scheme proposed in this chapter is an extension of the idea presented in [127], which only worked for PSK constellations. The proposed scheme is applicable regardless of the constellation type. Basically, mag-nitude-scaled SLM uses envelope scaling functions, which depend on the index of the phase vector, to scale the OFDM symbol. The receiver can then use a specially designed metric to recover the transmitted phase vector.

Notations: Upper case and lower case bold face letters represent matrices and column vectors respectively; superscript ^{T} and $^{\mathcal{H}}$ stand for the transpose and the Hermitian transpose, respectively; $E[\cdot]$ is the expectation operator; $\|\mathbf{x}\|_n$ is the ℓ^n-norm of $\mathbf{x}$; $|\mathbf{x}|$ is a vector that is the element-wise magnitude of $\mathbf{x}$; $|\mathcal{A}|$ is the cardinality of set $\mathcal{A}$; $\mathbf{D_x}$ is a diagonal matrix with vector $\mathbf{x}$ on the diagonal; the $N \times N$ discrete Fourier transform (DFT) matrix is denoted by $[\mathbf{Q}]_{n,k} = N^{-1/2} \exp(j2\pi(n-1)(k-1)/N)$.

6.2   OFDM Model

In OFDM, individual subcarriers in the frequency-domain are modulated with constellation points, transformed to the time-domain and transmitted with a cyclic prefix. For PAR analysis, the cyclic prefix can be ignored since it has no effect of the symbol PAR. Let the

74

frequency-domain vector of constellation points be

$$\mathbf{x} = [x_1, x_2, ..., x_{N-1}, x_N]^T, \tag{6.1}$$

where x_k is drawn from a R-point QAM constellation and the power in $\mathbf{x}$ is normalized so that $E\left[\|\mathbf{x}\|_2^2\right] = N$. Using the inverse discrete Fourier transform, the time-domain symbol is

$$\mathbf{y} = \sqrt{\mathcal{E}_y}\mathbf{Q}^{\mathcal{H}}\mathbf{x}, \tag{6.2}$$

where $\mathcal{E}_y$ is the symbol energy of $\mathbf{y}$. The PAR of the transmitted signal is defined by

$$PAR\{\mathbf{y}\} = \frac{\|\mathbf{y}\|_\infty^2}{\mathcal{E}_y}. \tag{6.3}$$

For transmission through a peak-power-limited channel it is desirable to make the PAR as low as possible. The received baseband frequency-domain signal after synchronization is $\mathbf{z} = \sqrt{\mathcal{E}_y}\mathbf{D_h}\mathbf{x} + \mathbf{n}$, where $\mathbf{D_h}$ is a diagonal matrix with diagonal elements from the channel frequency response vector $\mathbf{h}$ and $\mathbf{n}$ is white complex Gaussian noise with zero mean and variance σ_n^2. Finally, assuming perfect channel state information, the estimated transmitted symbol is $\hat{\mathbf{x}} \triangleq \frac{\mathbf{D_h}^{-1}}{\sqrt{\mathcal{E}_y}}\mathbf{z}$.

6.3 *Magnitude-scaled SLM*

In standard SLM, M complex-valued vectors $\mathbf{s}^{(m)}$ are multiplied with $\mathbf{x}$ prior to transmission, where $1 \leq m \leq M$ to get $\mathbf{x}^{(m)} \triangleq \mathbf{D}_{\mathbf{s}^{(m)}}\mathbf{x}$. The candidate signal $\mathbf{Q}^{\mathcal{H}}\mathbf{x}^{(m)}$ that produces the lowest PAR among the M possible candidate signals is selected for transmission. Every element in $\mathbf{s}^{(m)}$ has unit magnitude, i.e., $|\mathbf{s}^{(m)}| = \mathbf{1}_{N \times 1}$.

In contrast to SLM, magnitude-scaled SLM does *not* impose the constraint $|\mathbf{s}^{(m)}| = \mathbf{1}_{N \times 1}$. Specifically, the complex-valued scaling vectors for magnitude-scaled SLM are of the form

$$[\mathbf{s}^{(m)}]_k \triangleq p_k^{(m)}e^{j\phi_k^{(m)}}, \tag{6.4}$$

where $0 < p_k^{(m)} < \sqrt{2}$. The distribution of the phase angles, $\phi_k^{(m)}$ are chosen so that $E[e^{j\phi_k^{(m)}}] = 0$ (e.g., $\phi_k^{(m)} \sim U\{0, \pi\}$), which is the condition required for SLM to achieve maximum CFR [128]. Define $\left[\mathbf{p}^{(m)}\right]_k \triangleq p_k^{(m)}$, where $\mathbf{p}^{(m)}$ is chosen to be a scaled and

shifted column of a pseudo-random matrix that has elements of either 1 or -1. Denote column i of the $N \times N$ pseudo-random matrix by $\mathbf{w}^{(i)}$, and define the set of indices $\mathcal{K}_1^{(i)} = \{k \mid [\mathbf{w}^{(i)}]_k = 1\}$ and the set of indices $\mathcal{K}_{-1}^{(i)} = \{k \mid [\mathbf{w}^{(i)}]_k = -1\}$. We require that $|\mathcal{K}_1^{(i)}| = |\mathcal{K}_{-1}^{(i)}|$ so that the average power of $\mathbf{x}^{(m)}$ is the same as the average power of $\mathbf{x}$. One example of $\mathbf{w}^{(i)}$ is a column of the Hadamard matrix, which is called a Walsh sequence. With the 8-element Walsh sequence,

$$\mathbf{w}^{(3)} \triangleq [1, 1, -1, -1, 1, 1, -1, -1]^T, \tag{6.5}$$

we have $\mathcal{K}_1^{(3)} = \{1, 2, 5, 6\}$ and $\mathcal{K}_{-1}^{(3)} = \{3, 4, 7, 8\}$. Walsh sequences have the nice property that for $1 < i \leq N$, $|\mathcal{K}_1^{(i)}| = |\mathcal{K}_{-1}^{(i)}|$. The magnitude sequence is chosen so that $p_k^{(m)} = \sqrt{\beta}$ when $k \in \mathcal{K}_1^{(m+1)}$ and $p_k^{(m)} = \sqrt{2 - \beta}$ when $k \in \mathcal{K}_{-1}^{(m+1)}$ where $1 < \beta < 2$.

Now the mth time-domain candidate signal is

$$\mathbf{y}^{(m)} = \sqrt{\mathcal{E}_y} \mathbf{Q}^{\mathcal{H}} \mathbf{x}^{(m)} \tag{6.6}$$

As long as $\mathbf{p}^{(m)}$ is chosen according to the Walsh sequence, we can guarantee that $\mathrm{E}\left[\|\mathbf{y}^{(m)}\|_2^2\right] = N\mathcal{E}_y$, $\forall m$. The index of the transmitted candidate signal $\mathbf{y}^{(\bar{m})}$ is chosen so that

$$\bar{m} \triangleq \underset{1 \leq m \leq M}{\arg\min} \left\|\mathbf{y}^{(m)}\right\|_{\infty}. \tag{6.7}$$

The PAR reduction capability of BSLM is evaluated by the complementary cumulative distribution function (CCDF) of the PAR values after amplitude scalings and phase rotations. The results are compared to the theoretical and empirical CCDFs for SLM (the theoretical ccdf can be found in [7]). Four cases are simulated with combinations of different N and M (see Fig. 6.1). The amplitude-scaling factor is set to $\beta = 1.2$, and the phase rotation factor $e^{j\phi_k^{(m)}}$ is i.i.d. ± 1 with equal probability. 16QAM is selected as the transmitting constellation. From Fig. 6.1, CCDFs for BSLM agree with theoretical and empirical CCDFs for SLM very well for various N and M. Hence, magnitude-scaled SLM is shown to provide same PAR reduction capability as standard SLM.

The received frequency-domain SLM symbol will be

$$\mathbf{z} = \sqrt{\mathcal{E}_y} \mathbf{D_h} \mathbf{x}^{(\bar{m})} + \mathbf{n}. \tag{6.8}$$
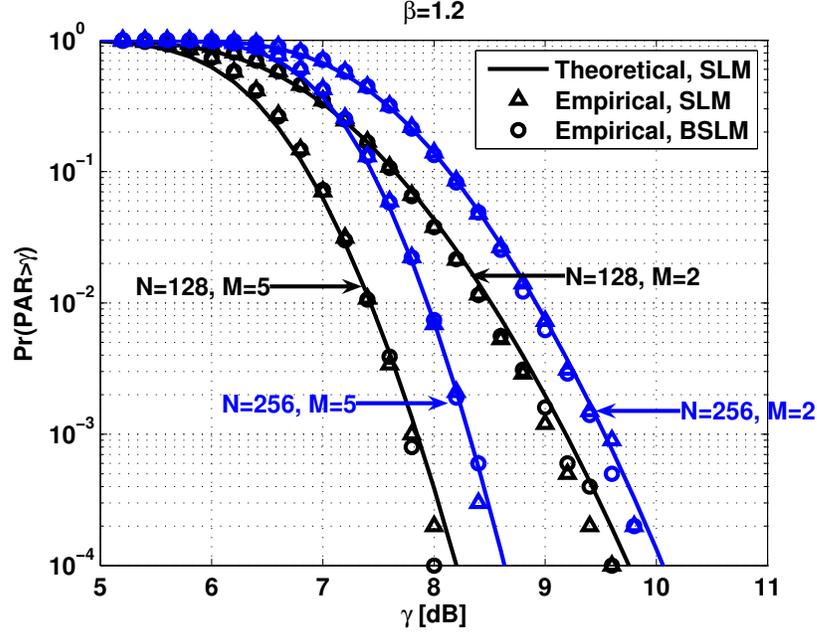
Figure 6.1: BSLM vs. SLM CCDF curves for 16QAM modulation.

Assuming perfect channel state information, we can write

$$\hat{\mathbf{x}}^{(\bar{m})} \triangleq \frac{\mathbf{D_h}^{-1}\mathbf{z}}{\sqrt{\mathcal{E}_y}} = \mathbf{x}^{(\bar{m})} + \frac{\mathbf{D_h}^{-1}\mathbf{n}}{\sqrt{\mathcal{E}_y}}. \tag{6.9}$$

Finally, in order to detect $\bar{m}$ blindly, we can create M receive metrics: one for each possible scaling sequence. The mth metric is

$$G^{(m)} = \sum_{k \in \mathcal{K}_1^{(m+1)}} \left| [\hat{\mathbf{x}}^{(\bar{m})}]_k \right|^2 - \sum_{k \in \mathcal{K}_{-1}^{(m+1)}} \left| [\hat{\mathbf{x}}^{(\bar{m})}]_k \right|^2 \tag{6.10}$$

It may also be convenient to express the detections metrics as a column vector

$$\begin{bmatrix} G^{(1)} \\ G^{(2)} \\ \vdots \\ G^{(M)} \end{bmatrix} = \left[\mathbf{w}^{(2)} \ \mathbf{w}^{(3)} \ \dots \ \mathbf{w}^{(M+1)} \right]^T \left| \hat{\mathbf{x}}^{(\bar{m})} \right|^2, \tag{6.11}$$

where $| \cdot |^2$ is the element-wise magnitude square value of a vector. Notice that $\mathrm{E}[G^{(\bar{m})}] = N\mathcal{E}_y(\beta - 1)$ and $\mathrm{E}[G^{(m \neq \bar{m})}] = 0$. Thus, we can estimate $\bar{m}$ with

$$\hat{\bar{m}} \triangleq \underset{1 \leq m \leq M}{\arg \max} G^{(m)}. \tag{6.12}$$

77

With $\hat{\bar{m}}$, the estimated symbol becomes

$$\hat{\mathbf{x}} = \mathbf{D}_{\mathbf{s}(\hat{\bar{m}})}^{-1} \hat{\mathbf{x}}^{(\bar{m})}. \tag{6.13}$$

6.4 Linear Scaling Channel Performance

Magnitude-scaled SLM is designed to operate in peak-power-limited channels. Thus, in order to provide a fair comparison of the proposed scheme to traditional OFDM in terms of SER, we must assume a clipping channel. Accordingly, we adopt the linear block scaling OFDM architecture proposed in [79]. In [79], it was demonstrated that by using a linear block scaling architecture the transmitted signal power is actually $1/PAR\{\mathbf{y}\}$, thus the SER of competing schemes is mostly aptly compared using the peak SNR (PSNR), where $PSNR \triangleq 1/PAR\{\mathbf{y}\}\sigma_n^2$. Assuming perfect detection of $\bar{m}$, a tight upper bound on the SER when QAM is used in an AWGN channel is

$$p_{s|\hat{m}=\bar{m}} \leq 2\mathrm{Erfc}\left[\sqrt{\frac{3r\beta PSNR}{2(R-1)}}\right] + 2\mathrm{Erfc}\left[\sqrt{\frac{3r(2-\beta)PSNR}{2(R-1)}}\right] \tag{6.14}$$

where R is the constellation size and $r \triangleq \log_2 R$ [88]. Furthermore, the detection error rate (DER) in an AWGN channel can be approximated by

$$\Pr\left[\hat{\bar{m}} \neq \bar{m}\right] = 1 - \left(1 - \frac{1}{2}\,\mathrm{Erfc}\left[\frac{(\beta-1)\sqrt{N}}{2\sigma PAR\{\mathbf{y}\}}\right]\right)^{M-1} \tag{6.15}$$

where $\sigma^2 = \sigma_n^4 + 2\sigma_n^2 + \mathcal{E}_y^2\sigma_{|x|^2}^2$ (see Appendix for details). The validity of this approximation is verified in Fig. 6.2. The plot shows that the expression in (6.15), matches very closely with the Monte Carlo simulated DER.

Finally, the SER of the proposed system can be quantified through $SER = p_{s|\hat{m}=\bar{m}} + DER(1 - 1/R - p_{s|\hat{m}=\bar{m}})$, where DER is defined in (6.15). In this case, SER depends on the random variable $PAR\{\mathbf{y}\}$. Obtaining the most precise estimate of the SER requires integrating SER over the probability density function of $PAR\{\mathbf{y}\}$ [14]. However, it is possible to use Jensen's inequality in conjunction with $\mathrm{E}[PAR\{\mathbf{y}\}]$ from [14] to provide a tight closed form lower bound on the SER.

In order to realize the full potential of the proposed scheme, it is necessary to optimize β and M, for a given signal power, $\mathcal{E}_y$, channel noise, σ_n^2 and constellation size R to minimize
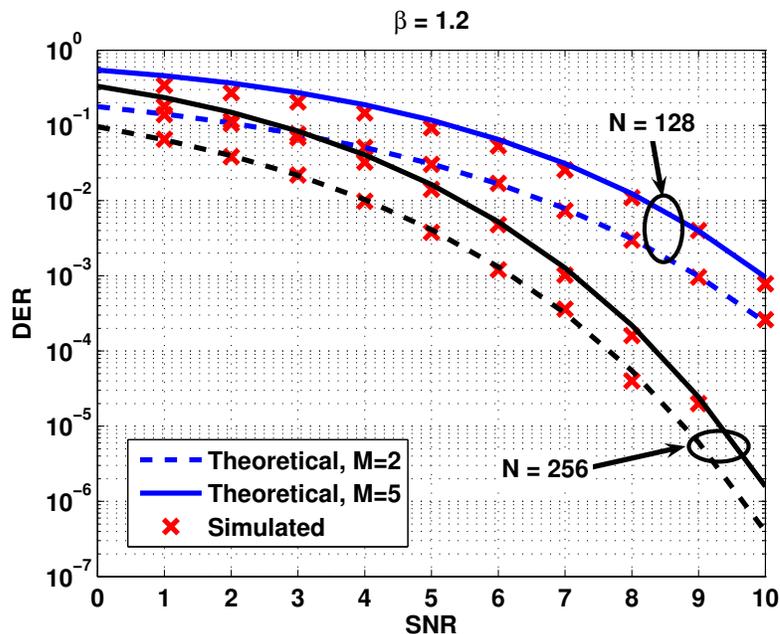
Figure 6.2: Simulated and theoretical DER for QPSK, where $SNR = \mathcal{E}_y/\sigma_n^2$.

the SER. Because the minimization is difficult to do analytically, we instead perform the optimization numerically. Fig. 6.3 is a plot of the optimal values of β versus $\log_2 N$. As expected, larger values for N lead to decreases in β. Finally, in Fig. 6.4 the SER for magnitude-scaled OFDM with optimized β is plotted along with standard OFDM. At 20dB of PSNR, the proposed magnitude-scale SLM scheme (with $M = 20$) outperforms standard OFDM by a factor of 10 in terms of SER.

6.5 Conclusions

In this chapter we proposed magnitude-scaled SLM as a CFR method that obviates the need for SLM side-information transmission. The proposed scheme uses Walsh-sequence based envelope function to shape the frequency-domain power profile of the OFDM symbol. At the receiver, envelope detection is used in conjunction with a specially designed metric to determine the transmitted SLM phase sequence. To verify the utility of magnitude-scaled SLM, we derived a closed-form bound for the SER and compared it to the SER of standard OFDM. In the linear block scaling channel corrupted by AWGN, the magnitude-scaled SLM signals saw in excess of a 1dB PSNR improvement over the standard OFDM.

6.6 Appendix

By applying the Central Limit Theorem, we can approximate $G^{(\bar{m})}$ and $G^{(m\neq\bar{m})}$ with Gaussian random variables so that $G^{(\bar{m})} \sim \mathcal{N}\left(N\mathcal{E}_y(\beta-1)/PAR\{\mathbf{y}\}, N\sigma^2\right)$ and $G^{(m\neq\bar{m})} \sim \mathcal{N}\left(0, N\sigma^2\right)$, where $\sigma^2 = \sigma_n^4 + 2\sigma_n^2 + \mathcal{E}_y^2\sigma_{|x|^2}^2$. Values of $\sigma_{|x|^2}^2$ are tabulated in Table 6.1.

When $M = 2$, we have

$$\Pr\left[\hat{\bar{m}} \neq \bar{m}\right] \quad = \quad \Pr\left[G^{(m\neq\bar{m})} > G^{(\bar{m})}\right] \tag{6.16}$$

$$= \quad \frac{1}{2}\,\mathrm{Erfc}\left[\frac{\mathcal{E}_y(\beta-1)\sqrt{N}}{2\sigma PAR\{\mathbf{y}\}}\right]. \tag{6.17}$$

For $M > 2$, assuming that $G^{(m\neq\bar{m})}$ is independent for different m, we can obtain

$$\Pr\left[\hat{\bar{m}} = \bar{m}\right] = \prod_{m\neq\bar{m}}\left\{1 - \Pr\left[G^{(m)} > G^{(\bar{m})}\right]\right\}. \tag{6.18}$$

Combining (6.17) and (6.18) results (6.15).

Table 6.1: Power variances for various constellation sizes

R	4	16	64	256	∞
$\sigma_{|x|^2}^2$	0	0.320	0.382	0.396	0.400
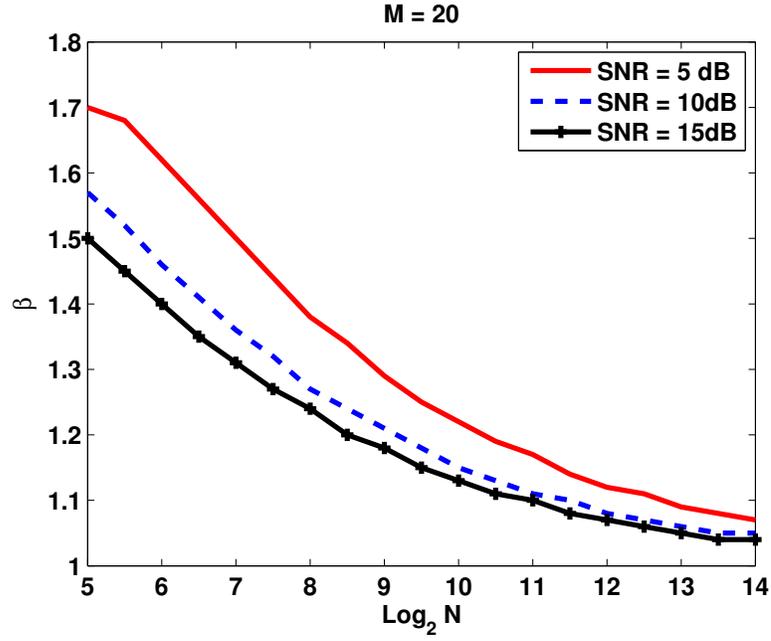
Figure 6.3: β versus $\log_2 N$, where $SNR = \mathcal{E}_y/\sigma_n^2$.
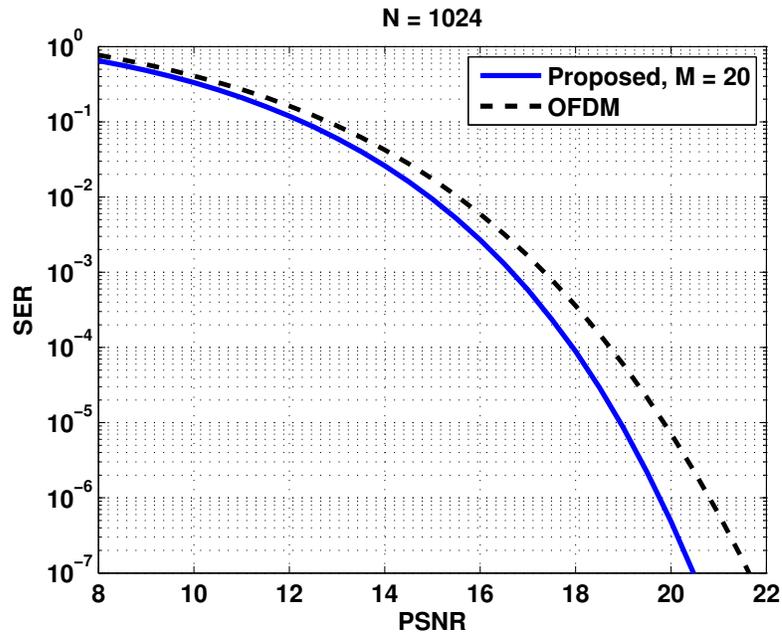
Figure 6.4: Total symbol error rate (including DER) versus the peak SNR.

CHAPTER VII

EMBEDDED SYNCHRONIZATION/PILOT SEQUENCE CREATION USING POCS

In this chapter we build on the orthogonal frequency division multiplexing (OFDM) peak-to-average power ratio (PAR) reduction work by Chen and Zhou. It has been demonstrated that pilot sequences that are constant modulus in the time domain can lead to an ensemble PAR-reduction across all data realizations. However, the problem of creating constant modulus sequences from arbitrary frequency domain power profiles has never been addressed. Often, it is desirable to have a some freedom of choice in how pilot and, possibly synchronization, energy is allocated in the frequency domain. In this chapter we present a projection on to convex sets (POCS) method for creating low-PAR synchronization/pilot (S/P) sequences with arbitrary frequency-domain power profiles.

7.1   Introduction

Orthogonal frequency division multiplexing (OFDM) has become a popular modulation method in high-speed wireless networks. By partitioning a wideband fading channel into flat narrowband channels, OFDM is able to mitigate the detrimental effects of multipath fading using a simple one-tap equalizer[1]. However, one drawback of OFDM is that OFDM signals exhibit large peak-to-average power ratios (PARs). Additionally, OFDM signals are very sensitive to timing offset (TO) and carrier frequency offset (CFO) [102].

One method for estimating the channel and combatting TO and CFO is to send a preamble sequence, $\{s_{pre}[n]\}_{n=0}^{N-1}$ prior to the information-bearing OFDM symbols. The receiver can perform a conjugate correlation of the received preamble and the expected pre-amble to extract an estimate for both the TO and the CFO with excellent probability

---

[1]Parts of this chapter were presented in R. J. Baxley and J. E. Kleider, "Embedded Synchronization/Pilot Sequence Creation Using POCS," *Proc. IEEE Intl. Conference on Acoustics, Speech, and Signal Processing*, Tolouse, France, May 2006. Reference [9].

of miss and false detection performance [112].

The received signal, after being corrupted by additive white Gaussian noise $\eta[n]$, a multipath channel $h[n]$, a TO n_o and a CFO ε, can be written as

$$w[n] = s_{pre}[n - n_o]e^{j2\pi n\varepsilon/N} * h[n] + \eta[n]. \tag{7.1}$$

Then the conjugate correlator output is

$$R[\tau] = \left(\sum_{l=0}^{N/2-1} s_{pre}^*[l]w[l-\tau] \right) \left(\sum_{l=N/2}^{N-1} s_{pre}^*[l]w[l-\tau] \right)^* \tag{7.2}$$

and the TO and CFO estimates are given, respectively, as $\hat{\tau} = \max_\tau |R[\tau]|$ and $\hat{\varepsilon} = \arg R[\hat{\tau}]$.

After TO and CFO correction, the channel can be estimated by dividing the frequency-domain version of the received signal, $W[k]$ by the frequency-domain version of the preamble, $S_{pre}[k]$. That is, $\hat{H}[k] = W[k]/S_{pre}[k]$.

In [48] it was suggested that embedded pilots can improve channel tracking performance in time-varying channels. This idea was furthered in [56] where it was shown that it is possible to forego the preamble sequence completely in favor of an embedded synchronization/pilot (S/P) sequence that is not completely orthogonal to the OFDM data. The authors of [56] argued that by linearly combining the S/P subsequence with the information-bearing OFDM sequence, a spectral efficiency improvement could be realized over the preamble synchronization approach.

In that model, the OFDM baseband frequency-domain data sequence is labelled $X[k]$, which is linearly combined with the S/P sequence, $S[k]$, so that the proportion of signal power in $S[k]$ is

$$\rho = \frac{\sum_{k=0}^{N-1} |S[k]|^2}{\sum_{k=0}^{N-1} |S[k] + X[k]|^2}. \tag{7.3}$$

If $S[k]$ and $X[k]$ have equal power, then the combined signal, $Y[k]$, is

$$Y[k] = \sqrt{1-\rho}X[k] + \sqrt{\rho}S[k]. \tag{7.4}$$

The discrete-time version of $Y[k]$ is

$$y[n] = \frac{1}{\sqrt{N}} \sum_{k=0}^{N-1} Y[k]\, e^{j\frac{2\pi kn}{N}}, \quad 0 \leq n \leq N-1. \tag{7.5}$$

In a practical system, a cyclic prefix is appended to $y[n]$, $y[n]$ is windowed, filtered, converted to an analog signal and up converted to the passband prior to transmission. In this chapter we are interested in peak-to-average power ratio (PAR). Accordingly, we can ignore the cyclic prefix as it does not contribute to the PAR. Also, the up conversion is known to increase the PAR by a constant of 3dB [109], so it too can be ignored in PAR considerations. Furthermore, the PAR of a signal before and after windowing, filtering and analog conversion is highly correlated, which means the affect on PAR of these processes is minimal [109]. Despite being beyond the scope of this chapter, it may be of interest to extend this work by taking windowing, filtering and analog conversion effects into account.

7.2   S/P Sequences

There are several considerations in designing S/P sequences. First, the authors of [65] were able to prove that, in order to minimize BER, the pilot tones should be equally spaced in the frequency domain and each assigned equal power. Second, for embedded synchronization applications, the authors of [56] relying partially on the work from [112] pointed out that synchronization sequences should have good conjugate correlation properties. As illustrated in [112], statistically independent PN-preamble sequences have excellent conjugate correlation properties. Third, in most OFDM applications, the S/P sequence will need to meet a spectral mask that includes null edge subcarriers. Fourth, in multiuser or multi-antenna systems it is desirable to have a large number of S/P sequences to choose from so that different users or antennaes can be distinguished. Finally, as we will explain in the next paragraph, the S/P sequences should have a low time-domain PAR.

Recall that $y[n]$ is a linear combination of $x[n]$ and $s[n]$, where $x[n]$ and $s[n]$ are the discrete time-domain representations of $X[k]$ and $S[k]$. Note that according to the central limit theorem, $x[n]$ is approximately complex-Gaussian distributed. We would like to create $s[n]$ so that the ensemble PAR of $y[n]$, across all realizations of $x[n]$, is minimum. The authors of [29] were able to experimentally show that a constant modulus $s[n]$, when linearly combined with $x[n]$, creates a $y[n]$ with a significantly lower PAR than when using
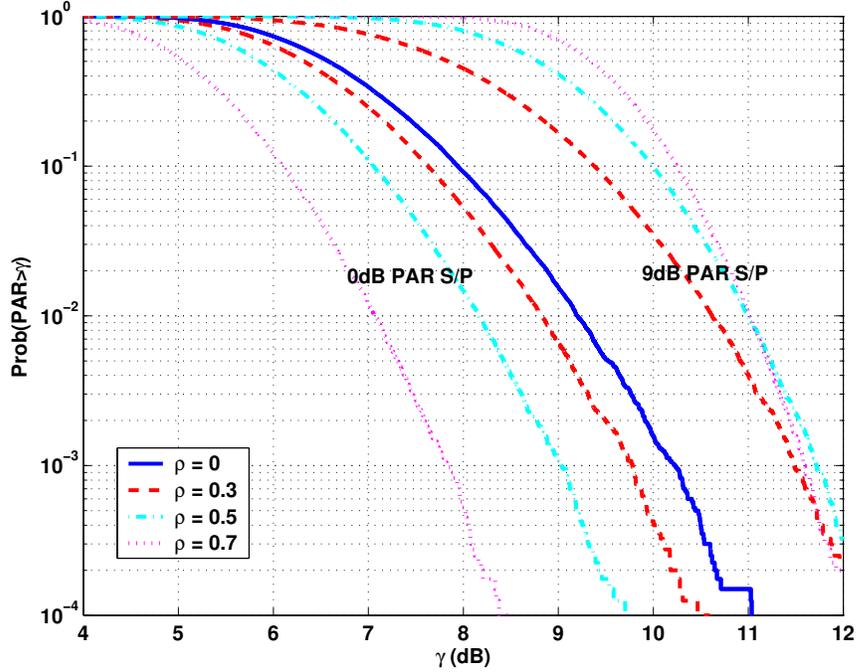
Figure 7.1: CCDFs of ODFM with a constant modulus embedded S/P sequence for different embedding factors and the CCDFs for a 9dB PAR embedded S/P sequence for different embedding factors.

a time-domain impulse train $s[n]$. In Figure 7.1 the CCDF of the PAR for two different embedding sequences with various embedding factors is plotted. The lower-PAR set of CCDF curves correspond to a S/P sequence that is constant modulus, while the higher-PAR curves correspond to a time-domain impulse train S/P sequence with a 9dB PAR. From the plot, it is obvious that the constant-modulus curves produce a significant PAR reduction.

In [108], the authors showed that chirp time domain sequences of the form $s[n] = e^{j\pi 2^v k^2/N}$ are equally-spaced (with spacing v), equally-power pilot sequences in the frequency domain. Here we would like to extend that result to more arbitrary frequency-domain sequences. Specifically, we are interested in being able to create $S[k]$ sequences that have null edge subcarriers, arbitrarily placed pilots, and, possibly, non-zero entries at the rest of the subcarriers as illustrated in Figure 7.2. Additionally, the time-domain versions of $S[k]$ should be low PAR and have excellent conjugate correlation properties.
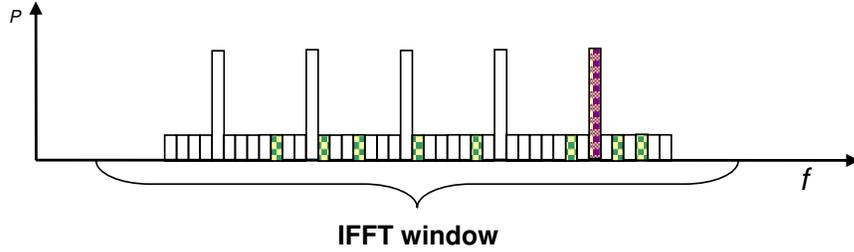
Figure 7.2: One possible example of a frequency-domain power profile.

Stated mathematically, the problem is

$$\text{minimize} \quad \text{PAR}\{s[n]\},$$

$$\text{subject to } |S[k]|^2 = P[k],$$

where $P[k]$ is the desired frequency-domain power profile. Notice that both $s[n]$ and $S[k]$ are N-length sequences, but $P[k]$ may contain zeros (at the null subcarriers).

The problem of finding the minimum-PAR sequence for a certain power profile can be solved using quadratically constrained quadratic programming (QCQP). However, using QCQP will only give one sequence per power profile without any guarantee of good self-correlation characteristics, whereas we want to be able to create many sequences with good self- and cross-correlation characteristics.

The QCQP problem can be solved suboptimally by using a me-thod known as projection on to convex sets (POCS). POCS is an active field with many applications like filter design, array signal processing, electron microscopy, speckle interferometry, topography, spectral estimation and neural networks [31]. Because POCS is an iterative search method, it may converge to a solution that is not the global minimum. However, it has the nice property that independent initial conditions cause the POCS algorithm to converge to independent solutions. We will exploit this property to allow for the creation of many independent near-optimal sequences.

For the problem at hand, we have two convex sets. The first is the power profile in the frequency domain and the second is the power profile in the time domain (i.e. low PAR). The 'projection' between the sets can easily be performed with the Fourier and inverse Fourier transforms. The procedure is listed below

86

1. Initialize the algorithm with a random-phase constant-modulus sequence $\bar{s}[n] = e^{j\theta_n}$, where $\theta_n \sim U[0, 2\pi)$.

2. Generate $\hat{S}[k] = \text{FFT}\{\bar{s}[n]\}$.

3. Using the phase of $\hat{S}[k]$, generate $\bar{S}[k] = \sqrt{P[k]}e^{j\angle\hat{S}[k]}$.

4. Generate $\hat{s}[n] = \text{IFFT}\{\bar{S}[k]\}$.

5. If the maximum number of iterations has been reached, exit the loop; else, go to step two.

After the algorithm finishes, there are two pairs of time/frequency sequences to choose from, $\{\bar{s}[n], \hat{S}[k]\}$ and $\{\hat{s}[n], \bar{S}[k]\}$. For the first pair, $\{\bar{s}[n], \hat{S}[k]\}$, the time-domain sequence has zero decibels of PAR, while the the frequency-domain sequence is not an exact match the desired power-profile. Instead, only the approximation, $|\hat{S}[k]|^2 \approx P[k]$, holds. Conversely, the pair $\{\hat{s}[n], \bar{S}[k]\}$ exactly meets the frequency-domain power-profile specification, but $\hat{s}[n]$ has a non-zero PAR. The question is, which pair should be used? Generally, it is desirable to choose $\{\hat{s}[n], \bar{S}[k]\}$ so that the frequency-domain power profile is perfectly matched to the desired profile. This choice ensures that the null subcarriers are actually nulls and that the pilots all have the same power.

7.3 Convergence Properties

As was pointed out in the last section, the properties of a S/P sequence depend on the initial conditions of the POCS algorithm. In practice, the S/P sequences are found offline so the speed of convergence is not a limiting factor. We are interested in finding the number of trials as well as the number of different initial conditions that must be used to find a suitably low-PAR sequence.

Figure 7.3 is a scatter plot of the PAR and MSE after 600 POCS iterations for 150 different initial conditions. The plot parameters are $N = 64$, there are 7 pilots and the amount of power in the non-pilot subcarriers is 20 percent of the power in the pilot subcarriers. In this plot, the MSE refers to the mean squared difference between $\hat{S}[k]$ and $\sqrt{P[k]}$ and the
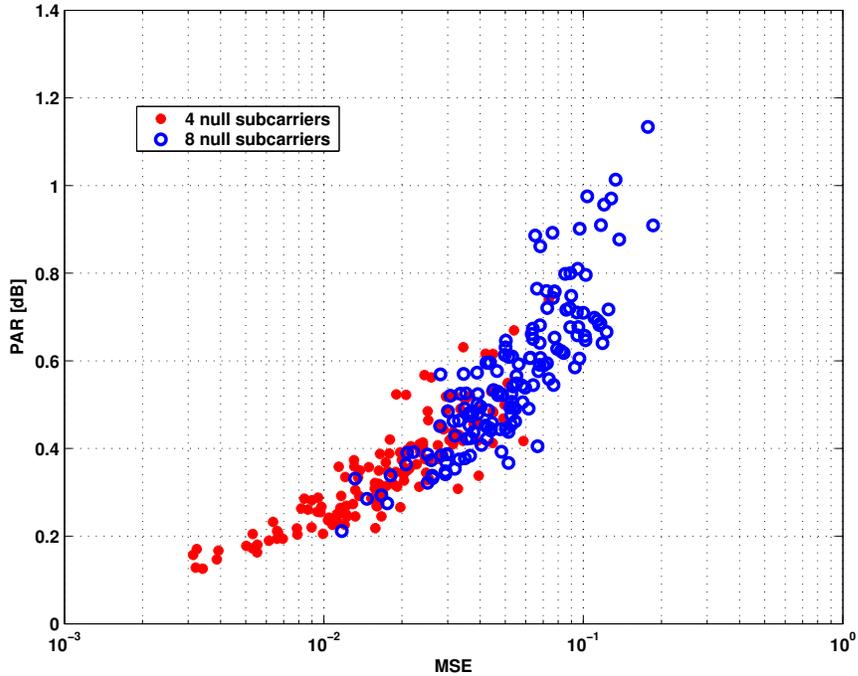
Figure 7.3: Plot of MSE versus PAR of 150 different initial conditions after 600 iterations.

PAR is the PAR of $\hat{s}[n]$. As was expected, the PAR and MSE are highly dependent on the initial conditions of the POCS algorithm.

Figure 7.4 is a plot of the convergence characteristics of the PAR for the five lowest-PAR sequences out of 150 different initial conditions. The plot parameters are $N = 64$, there are 7 pilots, a total of 4 null edge subcarriers, and the amount of power in the non-pilot subcarriers is 20 percent of the power in the pilot subcarriers. From the plot, we can see that the PAR is well below 1 dB for almost any initial conditions after 300 iterations.

In Figure 7.1 we plotted the CCDF of the PAR when a constant modulus S/P sequence
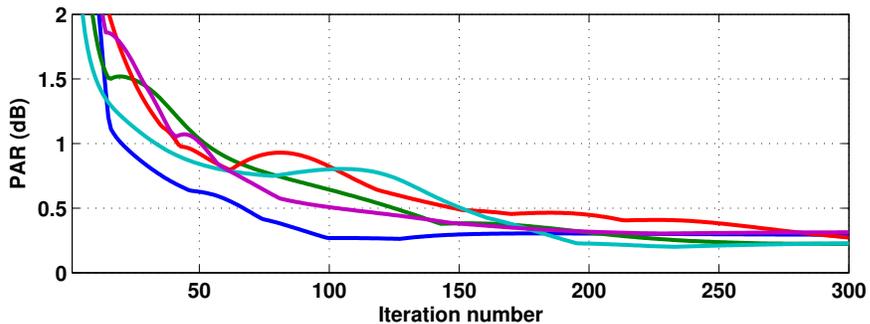
Figure 7.4: Plot of PAR for 5 low-PAR initial conditions through 300 iterations.
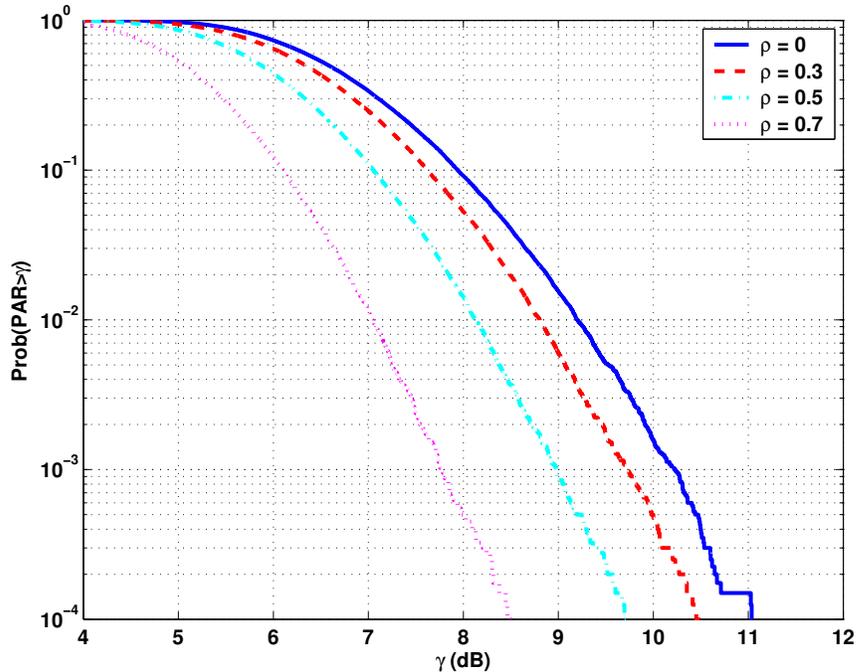
Figure 7.5: CCDF of the PAR of an OFDM signal with lowest-PAR S/P sequence after 300 iterations and 150 initial conditions embedded at different embedding factors.

is embedded in to an OFDM signal. Now we would like to illustrate that even though the S/P sequences created using the POCS procedure are not constant modulus, they do have a low enough PAR to still realize a large OFDM PAR reduction. Figure 7.5 is a plot of the CCDF of the the OFDM PAR when the lowest-PAR S/P sequence found after 300 iterations and 150 initial conditions is embedded in to an OFDM signal. In comparing the two figures, it is possible to see that the PAR CCDFs of the constant modulus S/P sequence embedding are virtually indistinguishable from the CCDFs of the 0.2 dB PAR S/P sequence embedding.

7.4   Correlation Properties

The correlation properties of the S/P sequences are very important for both TO and CFO estimation. In a multiuser system it may also be possible to use different S/P sequences for different users or for different antennas in a multi-antenna system. For the multi S/P sequence applications, it is be possible to distinguish users or antenna in addition to estimation the TO and CFO. We are also exploring the possibility of using a selected mapping [7]

approach with different S/P sequences to realize large PAR reductions. However, in order for any this to be feasible, the S/P sequences must have good conjugate correlation properties. In the present context, 'good' means that the non-peak self conjugate correlation values have to be small so that the TO can be correctly estimated. Additionally, for multi S/P sequence application it is also desirable to have all conjugate cross correlation values between different S/P sequences be small.

Figure 7.6 shows the CCDF of the non-peak maximum values of the conjugate correlation output with $N = 64$, 8 edge null subcarriers and 7 pilot subcarriers. Here we define $\beta = \frac{P[k_s]}{P[k_p]}$, where $P[k_s]$ is the power in the sync subcarriers that will be superimposed onto the information-bearing OFDM subcarriers and $P[k_p]$ is the power in the pilot subcarriers. This plot illustrates how sensitive the conjugate correlation operation is to β. As beta increases, the maximum non-peak conjugate correlation decreases. We note that, however, a larger β will increase the interference level that the S/P sequence contributes to the data-bearing OFDM subcarriers. More precisely, the ratio of the data-conveying energy to the noise energy is

$$SNR_e = \frac{(1-\rho)\sigma_Y^2}{\sigma_\eta^2 + \frac{\beta K_s}{K_p + \beta K_s}\rho\sigma_Y^2}, \tag{7.6}$$

assuming that the S/P signal is Gausssian and independent of the data signal, where σ_Y^2 is the power of the transmitted signal, σ_η^2 is the noise power, K_s is the number of sync subcarriers and K_p is the number of pilot subcarriers.

In choosing β and ρ, several parameters come into consideration. Among others the channel response, the maximum possible CFO, the amount of noise in the channel, and the size of N all affect the choice of β and ρ. Determining β and ρ in terms of those parameters is beyond the scope of this chapter. However, in Figure 7.7 we illustrate the effect of β and ρ on the maximum non-peak conjugate correlation output. The plot is of the CCDF of the maximum peak conjugate correlation output for different combinations of β and ρ with $N = 64$, 8 edge null subcarriers and 7 pilot subcarriers. The value of interest is $\zeta = 1$ as this is where the height of a non-peak output and a peak output are equal and thus indistinguishable. The distinguishability of these two cases is necessary for signal detection, so the probability level where $\zeta \geq 1$ is the probability that a S/P sequence for the given

90
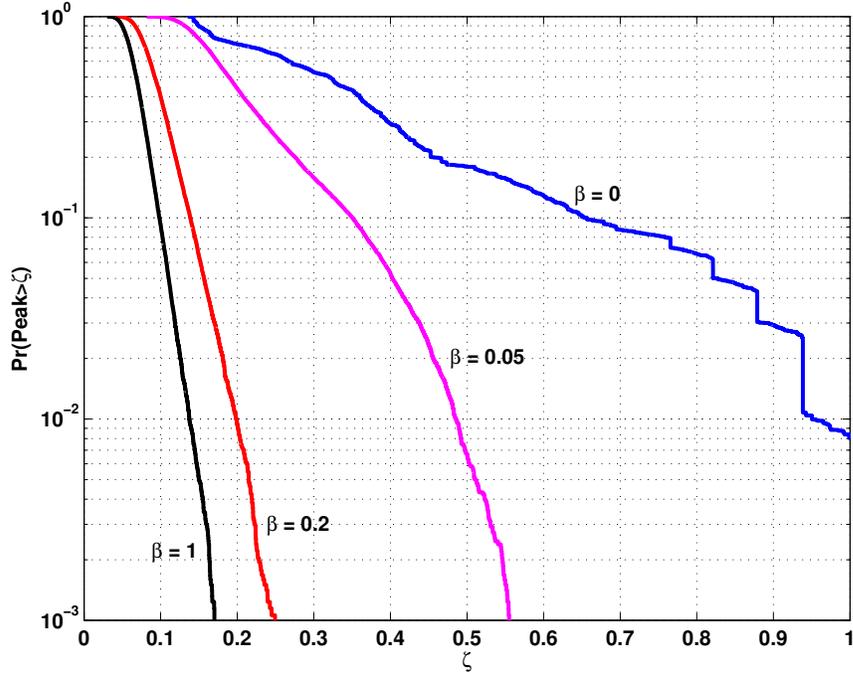
Figure 7.6: CCDF of the maximum non-peak conjugate correlation outputs for different amounts of non-pilot energy.

parameters will fail on average. For example, from Figure 7.7, we can see that for $\beta = 0.05$ and $\rho = 0.2$ the CCDF curve crosses $\zeta = 1$ with probability 0.005. So we can count on a S/P sequence created by the POCS method with those parameters to not be dependable for synchronization purposes five times in 1,000.

As was pointed out before, we are interested in searching through many different POCS initial conditions to find a low-PAR S/P sequence or, possibility, a set of low-PAR S/P sequences. But, in addition to finding low-PAR sequences, it is also necessary to find sequences with low non-peak correlation outputs so that the S/P sequence can be used in synchronization. Figure 7.8 is a plot of the normalized CCDF of the conjugate correlation output for the five lowest-PAR S/P sequences found out of 150 initial conditions with $N = 64$, 8 edge null subcarriers and 7 pilot subcarriers. To make the plot, 10,000 data sequences were created and combined in proportion with ρ for each of the five S/P sequences tested. The plot shows that there are not any drastic differences in conjugate correlation performance from one S/P sequence to the next for $\beta = 0.2$. On the other hand, the for $\beta = 0.05$, there are marked differences between the different S/P sequences. So depending
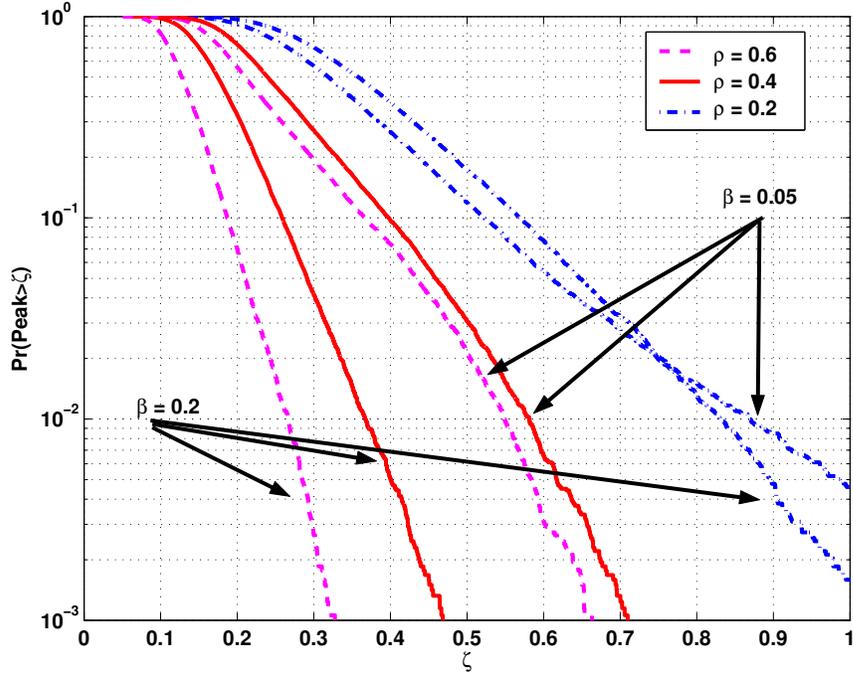
Figure 7.7: CCDF of the normalized maximum non-peak conjugate correlation outputs for various combinations of β and ρ.

on β and the application, correlation performance may or may not be worth examining when selecting S/P sequences.

Finally, Figure 7.9 is a plot of the probability of of a false detection (P_f) versus the probability of a miss detection (P_m) for two minimum-PAR S/P sequences generated from 300 iterations and 150 initial conditions, one with $\beta = 1$ and the other with $\beta = 1/7$ as well as a complex m-sequence created using a feedback shift register. For all three sequences $N = 64$, $\rho = 1$ and the $SNR = -7$dB.

7.5   Conclusions

In this chapter we have presented a novel method for creating low-PAR OFDM sychronization/pilot sequences with arbitrary frequency-do-main power profiles. By examining the convergence and correlation properties of the S/P sequences created by our scheme we have shown that only several hundred initial conditions and POCS iterations are necessary to find excellent S/P sequences. Through simulation, we were also able to show that for reasonable embedding factors, POCS-created S/P sequences can be used for embedded
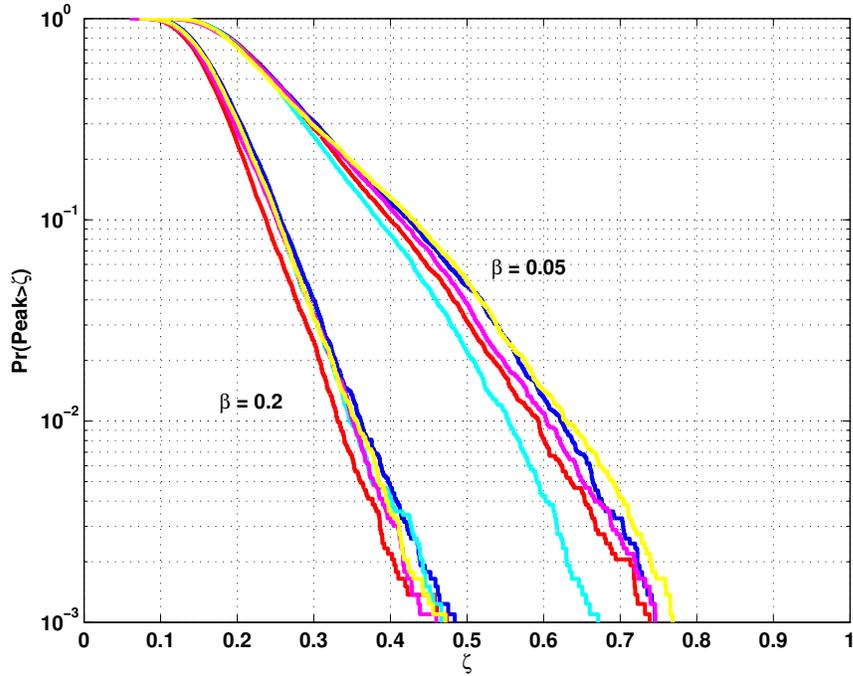
Figure 7.8: CCDF of the normalized maximum non-peak conjugate correlation outputs for the five lowest-PAR S/P sequences.

synchronization of OFDM signals that have P_m/P_f detection rates comparable to those of m-sequences. In future work, we will show how POCS-created S/P sequences can be integrated into a selected mapping PAR-reduction scheme to create even lower PAR embedded synchronization OFDM signals.
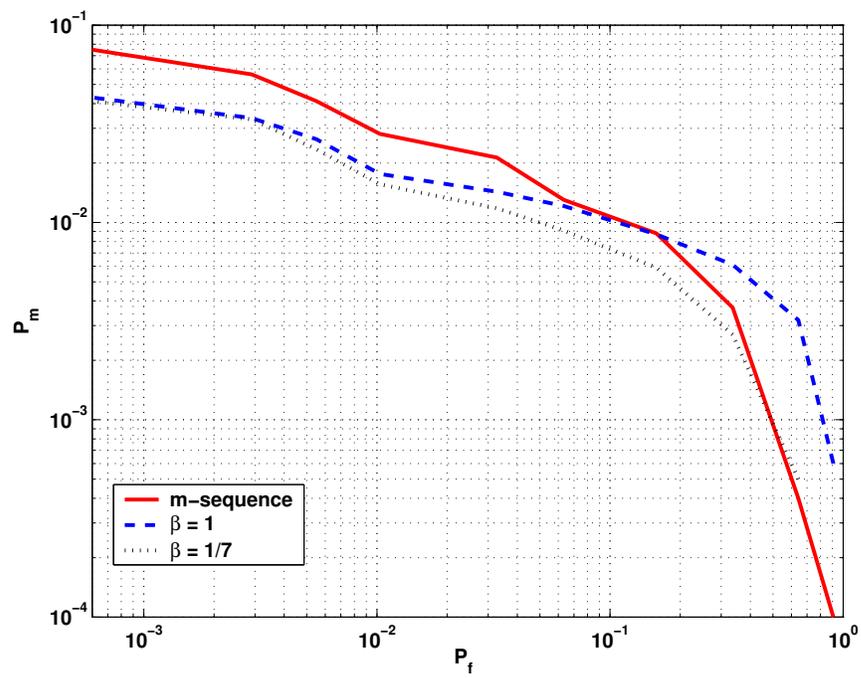
Figure 7.9: P_f versus P_m for two POCS-created S/P sequences compared with an m-sequence.

CHAPTER VIII

A METHOD FOR JOINT PEAK-TO-AVERAGE POWER RATIO REDUCTION AND SYNCHRONIZATION IN OFDM

Peak-to-average power ratio (PAR) reduction is an effective way to increase the power efficiency and decrease distortion noise in orthogonal frequency division multiplexing (OFDM) systems. Many PAR reduction schemes have been proposed, but few incorporate symbol-wise channel estimation and none accommodate per symbol synchronization. In this chapter we present joint synchronization pilot sequence (JSPS) selected mapping (SLM), which is a joint PAR reduction and synchronization scheme. In harsh peak-limited channels we show that JSPS-SLM can achieve large bit error rate (BER) performance gains.

8.1   Introduction

Orthogonal frequency division multiplexing (OFDM) is an effective high speed communications technique that allows for simple multipath channel equalization[1]. However, OFDM suffers from large peak-to-average power ratios (PARs) and sensitivity to carrier frequency offset (CFO). High PAR can lead to distortion noise and low power efficiency in peak limited channels, while CFO sensitivity can lead to inter-carrier interference (ICI).

In this chapter we develop a scheme that addresses both of these problems. The scheme is called joint synchronization pilot sequence (JSPS) selected mapping (SLM). The goal of our JSPS-SLM design is to simultaneously consider several channel impairments in a practical OFDM system and generate an unified approach to correcting for all of the impairments. The hope is that by simultaneously addressing the channel impairments along with the PAR, bandwidth overhead devoted to channel impairment correction can also be used for PAR reduction, which will lead to greater bandwidth efficiencies.

---

[1]Parts of this chapter were presented in R. J. Baxley, J. E. Kleider and G. T. Zhou, "A method for joint peak-to-average power ratio reduction and synchronization in OFDM," *Proc. IEEE Military Communications Conference*, Orlando, FL, October 2007. Reference [10].

JSPS-SLM is designed as a combined PAR reduction and embedded synchronization technique. Many PAR reduction schemes are designed without full consideration of the overall OFDM system. Specifically, other PAR reduction schemes generally assume perfect channel state information (CSI) and that the transmitter and receiver are perfectly synchronized in frequency and time. These assumptions may be realistic for static channels where a preamble-type synchronization sequence is used periodically. But for mobile communications applications, the channel is rarely static. Furthermore, it was shown in [56] that frequency-hopped ODFM is not bandwidth efficient when preamble synchronization is used.

8.2 System Model

To make a realistic characterization of the channel model that exists in mobile communications many different channel effects have to be included. Obviously, multipath fading and some sort of additive noise will be present. In addition to these two standard channel model components, a realistic, unsynchronized channel will have carrier frequency offset (CFO) and timing offset (TO) effects, which are often ignored in OFDM PAR analyses. Furthermore, in a peak power-constrained system, it is necessary to include the clipping characteristic of the power amplifier (PA) in the channel model. By including the PA in the channel model, the signal dynamic range becomes a design consideration making PAR reduction an attractive possibility.

In this chapter, the channel model is characterized by

$$z[n] = (f_{PA}(y[n - n_0]) \star h[n]) e^{-j2\pi\epsilon/N} + \eta[n]. \tag{8.1}$$

where $f_{PA}(\cdot)$ is the power amplifier input-to-output characteristic, which is assumed to be time-invariant with respect to each OFDM symbol and $\star$ is the convolution operator. A block diagram of the channel is displayed in Fig. 8.1.

The baseband data-bearing part of the transmitted signal prior to cyclic extension can
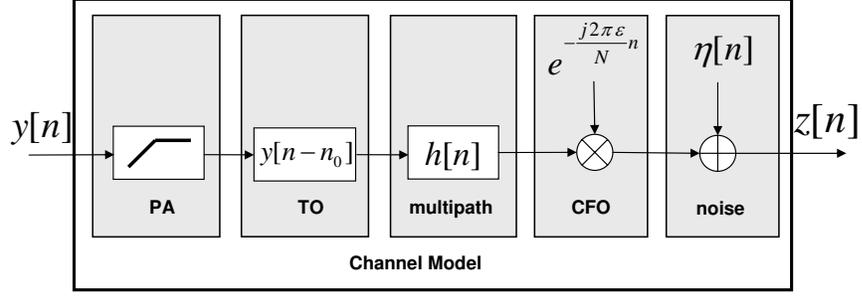
Figure 8.1: Channel model of the proposed system.

be expressed as

$$x[n] = \frac{1}{\sqrt{N}} \sum_{k=0}^{N-1} X_k \, e^{j2\pi kn/N} \tag{8.2}$$

$$= IDFT\{X_k\}. \tag{8.3}$$

where $\{X_k\}_{k=0}^{N-1}$ are drawn from a finite constellation and $n \in \{0, 1, ..., N-1\}$.

8.3 PAR, Selected Mapping and Synchronization

PAR is one metric for assessing the dynamic range of a signal. Signals with a low PAR are preferable because they allow the PA to operate at higher power efficiencies [109]. The PAR is defined

$$PAR\{y[n]\} = \frac{\max_n |y[n]|^2}{E\left[|y[n]|^2\right]}. \tag{8.4}$$

Selected mapping (SLM) is a popular PAR reduction tool that can reduce the PAR of OFDM symbols by several dBs [7]. In SLM, D candidate OFDM signals are generated by

$$x^{(d)}[n] = IDFT\{X_k e^{j\phi_k^{(d)}}\} \tag{8.5}$$

where $d \in \{1, 2, ..., D\}$. The index of the candidate signal with the lowest PAR is

$$\bar{d} = \min_{d \in \{1,2,...,D\}} PAR\{x^{(d)}[n]\}, \tag{8.6}$$

thus the transmitted signal $x^{(\bar{d})}[n]$ has the lowest PAR among the candidates. In order for the receiver to recover X_k, it must know $\phi_k^{(\bar{d})}$. It is reasonable to assume that the table of all values of $\phi_k^{(d)}$ is known at both the transmitter and receiver. With this assumption, the receiver only needs knowledge of $\bar{d}$ in order to recover X_k.

There have been many proposals for $\bar{d}$ recovery; some involve the transmission of side information (SI) and others work blindly without SI. The SI-based methods are not desirable because they reduce the bandwidth efficiency by utilizing bits that could otherwise be used for information transmission. Several promising blind detection methods have been proposed [83, 13, 51, 15, 28]. However, all of these methods assume that the receiver is perfectly synchronized with the transmitter. This may be the case in static channels, however, in mobile or frequency hopping environments it may be necessary to estimate the channel every symbol.

The purpose of this chapter is to outline a blind phase sequence detection method that does not require time or frequency synchronization or knowledge of the channel. We will show that the resulting scheme is robust in these unsynchronized, multipath, peak-limited channels.

8.4   JSPS-SLM OFDM

As we will explain, JSPS-SLM OFDM is a PAR reduction technique that is robust in harsh channels. The basic idea is to combine the embedded synchronization technique from [56] with SLM. However, the combination is not trivial as many design parameters need to considered.

The transmitted signal is made up of two parts, the data part X_k and the JSPS part S_k, that are combined through the parameter ρ. The resulting signal in the frequency domain is

$$Y_k = \sqrt{\rho}S_k + \sqrt{1-\rho}X_k, \tag{8.7}$$

where ρ is the embedding factor that dictates how much signal power is allocated to S_k. Here S_k and, equivalently $s[n] = IDFT\{S_k\}$, is a sequence known to the transmitter and the receiver that can be used for CFO estimation and TO estimation according to the procedures in [112]. In [56], the authors extended the method in [112] so that *embedded* sequences could be used for multipath channel estimation in addition to CFO and TO estimation.

In the proposed JSPS-SLM method, D candidate signals $\{y^{(d)}[n]\}_{d=1}^{D}$ are generated
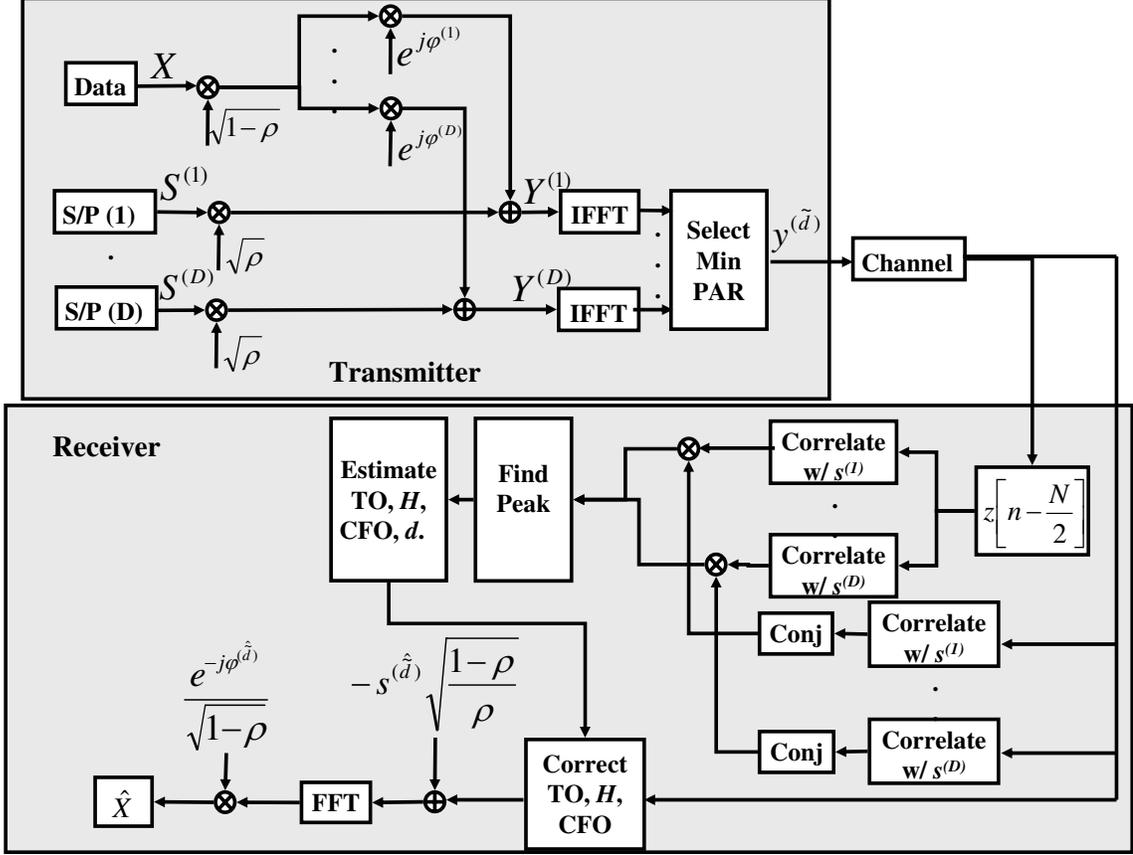
Figure 8.2: JSPS-SLM block diagram.

according to

$$Y_k^{(d)} = \sqrt{\rho}S_k^{(d)} + \sqrt{1-\rho}X_k e^{j\phi_k^{(d)}}, \tag{8.8}$$

where $y^{(d)}[n] = IDFT\{Y_k^{(d)}\}$. In Section 8.5, we will outline the design criteria for generating $S_k^{(d)}$. The candidate with the lowest PAR will be selected for transmission. Thus, if

$$\tilde{d} = \min_{d \in \{1,2,\ldots,D\}} PAR\{y^{(d)}[n]\}, \tag{8.9}$$

then the transmitted signal is $y^{(\tilde{d})}[n]$. The goal is for the receiver to be able to recover X_k, but the problem is that $\tilde{d}$ is unknown in the receiver. It is assumed that the receiver has knowledge of $S_k^{(d)}$ and $\phi_k^{(d)}$. So, in order for the receiver to determine $S_k^{(\tilde{d})}$ and $\phi_k^{(\tilde{d})}$, $\tilde{d}$ must be recovered. Fortunately, the conjugate correlation receiver can be used to do this. The received signal can now be expressed as

$$z^{(\tilde{d})}[n] = \left(f_{PA}\left(y^{(\tilde{d})}[n-n_0] \right) \star h[n] \right) e^{-j2\pi\epsilon/N} + \eta[n]. \tag{8.10}$$

Define the conjugate correlation (CC) between two length-N sequences to be

$$\text{CC}\{a[n], b[n]\} = \left(\sum_{n=0}^{N/2-1} a^*[n]b[n-u] \right) \left(\sum_{n=N/2}^{N-1} a^*[n]b[n-u] \right)^*, \tag{8.11}$$

where $(\cdot)^*$ is the conjugate operation. In the receiver, D conjugate correlation outputs are generated using

$$r^{(d)}[u] = \text{CC}\{s^{(d)}[n], z^{(\tilde{d})}[n-u]\}. \tag{8.12}$$

From $r^{(d)}[u]$, the SLM index, the TO and the CFO can be estimated by

$$\hat{\tilde{d}} = \arg\max_d |r^{(d)}[u]| \tag{8.13}$$

$$\hat{n}_0 = \arg\max_u |r^{(\hat{\tilde{d}})}[u]| \tag{8.14}$$

$$\hat{\epsilon} = \arg\left(r^{(\hat{\tilde{d}})}[\hat{n}_0] \right). \tag{8.15}$$

Hence, JSPS-SLM uses a robust and completely novel blind phase sequence detection criterion as defined in (8.13). As opposed to the other methods, the phase sequence index is detected based on the conjugate correlation with the candidate synchronization sequences, $s^{(d)}[n]$. Designing these sequences to optimize performance is a difficult problem that we will address in Section 8.5.

To illustrate how X_k can be recovered from $z^{(\tilde{d})}[n]$ using the estimators in (8.13-8.15), let us decompose the frequency-domain data signal into three non-overlapping parts: 1) data subcarrier denoted by the set of indices $\mathcal{K}_d$, 2) pilot subcarriers denoted by the set of indices $\mathcal{K}_p$, and 3) null subcarriers denoted by the set of indices $\mathcal{K}_n$. In this system configuration, $X_{k\notin\mathcal{K}_d} = 0$, so X_k only contains energy in the data subcarriers. The null subcarriers are constrained to zero to limit the amount of out-of-band spectral energy that encroaches on neighboring channels. The pilots will be defined as part of S_k. Just as with X_k, S_k can also be decomposed using the same three set of subcarrier indices: 1) synchronization subcarriers, $\mathcal{K}_d$, 2) pilot subcarriers, $\mathcal{K}_p$, and 3) null subcarriers, $\mathcal{K}_n$. The contents of the different sets is summarized in 8.1.

To recover X_k, first the receiver generates the quantity

$$W_k^{(\tilde{d})} = IDFT\left\{ z^{(\tilde{d})}[n+\hat{n}_0]e^{j2\pi n\hat{\epsilon}/N} \right\}, \tag{8.16}$$

100

Table 8.1: JSPS-SLM Signal Components

	$k \in \mathcal{K}_d$	$k \in \mathcal{K}_p$	$k \in \mathcal{K}_n$
X_k	$\neq 0$	$=0$	$=0$
S_k	$\neq 0$	$\neq 0$	$=0$
Y_k	$\neq 0$	$\neq 0$	$=0$

which gives $W_k^{(\tilde{d})} = Y_k^{(\tilde{d})} H_k + \eta_k + \delta_k + \iota_k$, where δ_k is the frequency domain noise caused by the power amplifier, ι_k is the inter-carrier interference (ICI) and where H_k and η_k are the IDFTs of $h[n]$ and $\eta[n]$, respectively. From $W_k^{(\tilde{d})}$ the channel in the pilot subcarriers can be estimated using

$$\hat{H}_k = \frac{W_k^{(\tilde{d})}}{S_k^{(\hat{d})}\sqrt{\rho}}, \quad k \in \mathcal{K}_p. \tag{8.17}$$

These pilot subcarrier channel estimates can be easily interpolated to the data-bearing subcarriers, $k \in \mathcal{K}_d$, using the techniques described in [25] so that $\hat{H}_k$ is defined for $k \in \mathcal{K}_d \bigcup \mathcal{K}_p$. Finally, the data symbol can be estimated via

$$\hat{X}_k = \frac{e^{-j\phi_k^{(\hat{d})}}}{\sqrt{1-\rho}}\left(\frac{W_k^{(\tilde{d})}}{\hat{H}_k} - \sqrt{\rho}S_k^{(\hat{d})}\right), \quad k \in \mathcal{K}_d \tag{8.18}$$

It is obvious from (8.18) that the calculation of $\hat{X}_k$ is highly sensitive to the estimated parameter $\hat{\tilde{d}}$. If $\hat{\tilde{d}} \neq \tilde{d}$, then $\hat{X}_k$ will be a phase scrambled version of X_k, making data recovery impossible, thus it is imperative that $\tilde{d}$ is estimated correctly. The entire JSPS-SLM system is shown as a block diagram in Fig. 8.2.

8.5   Synchronization Sequence Design

So far, we have introduced the transmitter and receiver structure for JSPS-SLM OFDM. In this section, we consider the design issues involved in generating $S_k^{(d)}$. The JSPS-SLM system can be broken into three major sections: i) PAR reduction in (8.9), ii) synchronization in (8.13-8.15), and iii) channel estimation in (8.17). This Section will outline the various design tradeoffs and considerations in each of these major parts.

8.5.1 PAR Reduction

In JSPS-SLM, there are two main sources of PAR reduction. One source is the fact that we are using D candidate signals and selecting the candidate with the lowest PAR. A more subtle source of PAR reduction in JSPS-SLM is in the design of $S_k^{(d)}$.

It was shown in [29], that by cleverly designing $S_k^{(d)}$, large PAR reductions are possible. Specifically, when $IDFT\{S_k^{(d)}\} = s^{(d)}[n]$, has low PAR, the combined sequence, $y^{(d)}[n] = \sqrt{\rho}s^{(d)}[n] + \sqrt{1-\rho}x^{(d)}[n]$, will, on average, have lower PAR than $x^{(d)}[n]$. The extent of the PAR reduction is largely dictated by the size of ρ. Larger values for ρ lead to larger PAR reductions. Also, in [29], it was shown that by improperly choosing the embedding sequences (e.g. high PAR sequences) will actually lead to a PAR increase. So it is vital that the set of sequences $\{s^{(d)}[n]\}_{d=1}^D$ all have low PAR.

However, designing D sequences $\{s^{(d)}[n]\}_{d=1}^D$, that all have low PAR and that meet the desired spectral constraints is not a trivial problem. In [9], we developed a flexible framework for generating a set of low-PAR sequences with an arbitrary power spectral density (PSD) that involved convex optimization techniques. Using this method it is possible to generate a set of sequences that all have $PAR < 0.5$dB. Deploying the resulting sequences $\{s^{(d)}[n]\}_{d=1}^D$ in JSPS-SLM results in large PAR reductions as demonstrated in Fig. 8.3. For instance, the PAR reduction at the 10^{-3} probability level is 4dB from the $\rho = 0$, $D = 1$ case to the $\rho = 0.3, D = 8$.

8.5.2 Synchronization

In the context of JSPS-SLM, synchronization includes $\tilde{d}$ detection, n_0 estimation and ϵ estimation. The first step in JSPS-SLM synchronization is determining which phase sequence index was transmitted, via the criterion in (8.13). From (8.13) it is apparent that correct detection of $\tilde{d}$ depends on the peaks of $|r^{(d)}[u]|$ for $d \neq \tilde{d}$. When these spurious peaks are all less than the peak in $|r^{(\tilde{d})}[u]|$, $\tilde{d}$ will be correctly detected. Thus, the set of $\{s^{(d)}[n]\}_{d=1}^D$ should be designed so that spurious peaks are low.

Once, $\tilde{d}$ is detected, the next step is to determine the TO, n_0 via (8.14). Equation (8.14), shows that n_0 is determined based on the maximum of the $\hat{\tilde{d}}$th conjugate correlation output.
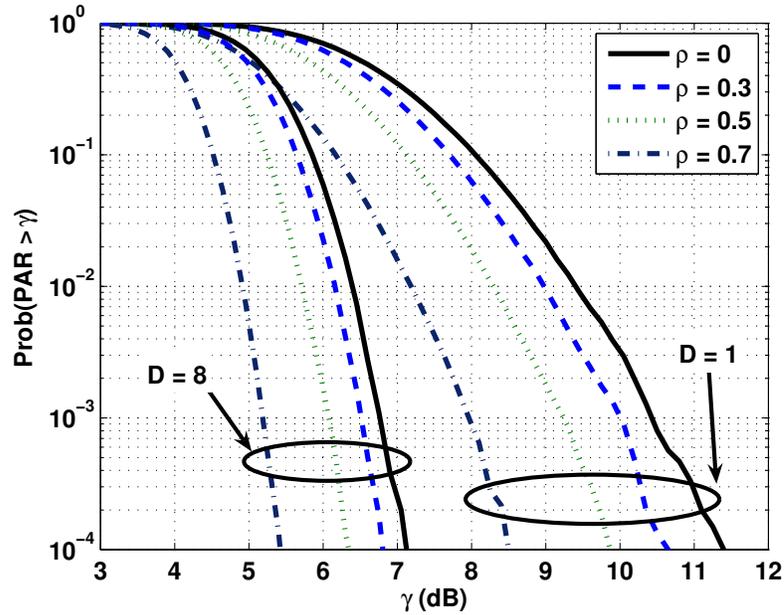
Figure 8.3: PAR CCDF for JSPS-SLM for different embedding factors ρ.

Assuming that $\hat{\tilde{d}} = \tilde{d}$, n_0, will be detected correctly as long as $|r^{(\tilde{d})}[n_0]| > |r^{(\tilde{d})}[n]|$ for $n \neq n_0$. Various performance simulations using different design parameters were provided in [9].

The final step in synchronization, is the estimation of the CFO parameter ϵ. There is no obvious relationship between the design of $\{s^{(d)}[n]\}_{d=1}^{D}$ and the estimation error $\mathrm{E}\left[|\epsilon - \epsilon|^2\right]$. Thus, for the purposes of this chapter, it is assumed that if the other two synchronization design criteria are met, that the resulting set of sequences $\{s^{(d)}[n]\}_{d=1}^{D}$, will also achieve adequate performance.

8.5.3 Channel Estimation

The performance of the zero forcing channel estimator defined in (8.17) is sensitive to the positions of the pilots and to the power allocated to the pilot subcarriers, S_k, $k \in \mathcal{K}p$. There is a large amount of literature involving optimal pilot placement for OFDM. When the subcarrier spacing is less than the number of null subcarriers (i.e. $|\mathcal{K}_n| \leq N/|\mathcal{K}_p| - 1$), placing constant power pilots evenly throughout the N subcarriers minimizes the channel estimation MSE [78]. When this condition is not satisfied, other pilot positioning techniques have been proposed [73, 11].

The amount of power in the pilot subcarriers can be quantified through

$$\beta = \frac{\sum_{k \in \mathcal{K}_p} |S_k|^2}{\sum_{k \in \mathcal{K}_p \bigcup \mathcal{K}_d} |S_k|^2},$$ (8.19)

which is the ratio of pilot power to the total JSPS power. Without loss of generality, set $\sum_{k \in \mathcal{K}_p \bigcup \mathcal{K}_d} |S_k|^2 = 1$ and $\mathrm{E}\left[\sum_{k \in \mathcal{K}_p \bigcup \mathcal{K}_d} |X_k|^2\right] = 1$. Now, to get an approximate relationship between the symbol estimation error and the parameters β, ρ, and the noise variance, assume that all of the synchronization works perfectly (i.e. $\hat{\tilde{d}} = \tilde{d}$, $\hat{n}_0 = n_0$ and $\hat{\epsilon} = \epsilon$) and that no distortion noise is introduced by the transmitter PA. Also, we assume that the interpolated channel estimate in each data subcarrier has the same error variance as the channel estimate in the pilot subcarriers (i.e. $\mathrm{E}[|\hat{H}_k - H_k|^2] = \frac{|\mathcal{K}_p|}{\beta \rho |\mathcal{K}_d|} \; \forall \; k \in \mathcal{K}_p \bigcup \mathcal{K}_d$). This assumption is valid when the zero-forcing channel estimator is used and $|\mathcal{K}_n| \le N/|\mathcal{K}_p| - 1$. With these assumptions, we have $W_k^{(\tilde{d})} = Y_k^{(\tilde{d})} H_k + \eta_k$, where η_k is complex Gaussian distributed (i.e., $\eta_k \sim \mathcal{CN}(0, \sigma_\eta^2)$).

Using these assumptions, (8.18), and the first order approximation that $\mathrm{E}[|\eta_k|^2 |\hat{X}_k|^2] \approx \sigma_\eta^2$ for $k \in \mathcal{K}_d$, the symbol estimate MSE is

$$\mathrm{E}\left[|\hat{X}_k - X_k|^2\right] = \frac{\sigma_\eta^2}{\sigma_{H_k}^2} \left(\frac{(1 - \beta)|\mathcal{K}_p|}{\beta(1 - \rho)|\mathcal{K}_d|} + \frac{|\mathcal{K}_p|}{\beta \rho |\mathcal{K}_d|} + \frac{1}{1 - \rho}\right)$$ (8.20)

for $k \in \mathcal{K}_d$. Notice, that the MSE is dependent on the ratio of pilot to data subcarriers $|\mathcal{K}_p|/|\mathcal{K}_d|$. Also, the minimizing β is $\beta = 1$ when perfect synchronization is assumed. However, in order to achieve acceptable synchronization performance it will be necessary to have $\beta < 1$. Some analysis on the effect of β is synchronization can be found in [9]. However, once β is chosen such that the synchronization performance is adequate, ρ should be chosen such that the symbol MSE in (8.20) is minimized. Fig. 8.4 is a plot of the minimizing ρ value, ρ^{opt}, that should be used for a given β and pilot-to-data subcarrier ratio, $|\mathcal{K}_p|/|\mathcal{K}_d|$.
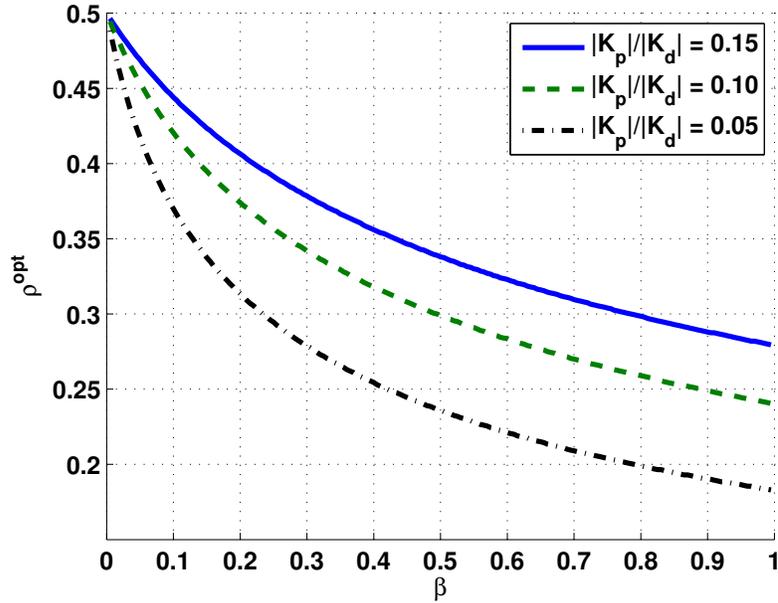
Figure 8.4: Optimal ρ for a given β.

8.6 Simulations

The plot in Fig. 8.5 demonstrates the BER performance of JSPS-SLM. To generate the plot, the convex optimization technique in [9] was used to generate the sequences $\{s^{(d)}[n]\}_{d=1}^{D}$ for the two JSPS-SLM designs. For the dot-dash non-JSPS-SLM curve, embedded synchronization was used without any PAR reduction considerations (i.e. $D = 1$ and $S_k^{(1)}$ was generated with the prescribed power profile but random phases). The embedded synchronization scheme was also plotted for the case when the CFO is not estimated to show how poor the performance of a PAR-reduction scheme that does not use CFO estimation could be.

For the plot, an ideal soft limiter channel was used with an input backoff (IBO) of 3dB. The CFO was set to a constant $\epsilon = 0.2$. The multipath channel, $h[n] \sim \mathcal{CN}(0, Ae^{-n})$, was set to length 16 with an exponential delay spread such that $A \sum_{n=0}^{15} e^{-n} = 1$. Also, $N = 256$, $|\mathcal{K}_p| = 16$, $|\mathcal{K}_d| = 240$ and $|\mathcal{K}_n| = 0$. The pilot tones were evenly spaced with equal power. The embedding factors were chosen to be $\beta = 0.25$ and $\rho = 0.35$.

The plot shows that JSPS-SLM outperforms the embedded synchronization schemes. Also, at high SNRs the $D = 8$ JSPS-SLM case performs more than 5dB better than the

$D = 1$ case.
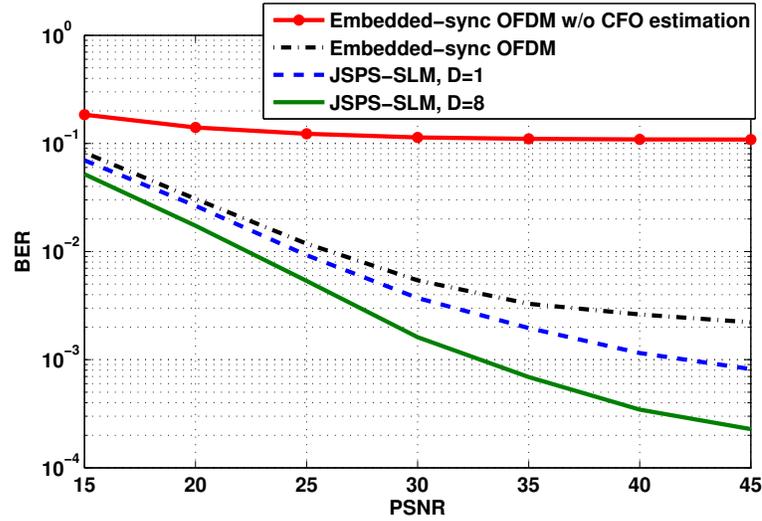
Figure 8.5: BER for JSPS-SLM and regular OFDM where $\epsilon = 0.2$ and $IBO = 3$dB.

8.7 Conclusions

In this chapter we have outlined the JSPS-SLM technique for OFDM, which is a joint PAR reduction synchronization channel estimation scheme. Also, we have outlined the major design decisions that must be made for JSPS-SLM. In addition to a high bandwidth efficiency, with proper design, we have shown that large PAR reductions are possible using JSPS-SLM. Finally, we demonstrated that large BER improvements are also possible using JSPS-SLM in harsh channel environments.

CHAPTER IX

PILOT DESIGN FOR OFDM WITH NULL EDGE SUBCARRIERS

Pilot symbol assisted modulation (PSAM) orthogonal frequency division multiplexing (OFDM) has proven to be a popular technique for high-speed communication through multipath fading channels. In this chapter we examine PSAM pilot design optimization in OFDM systems that employ edge null subcarriers for spectral shaping. Specifically, we show that the commonly used even pilot spacing design is suboptimal in terms of symbol estimate mean squared error (MSE) performance when a sufficient number of null subcarriers are present. We pursue a parametric design of the pilot spacings and use convex optimization techniques in order to find a pilot design that results in near-optimal symbol estimate MSE performance. Finally, we present several example PSAM OFDM pilot designs including one example based on the IEEE 802.16 standard to demonstrate performance improvements over the conventional even-spacing pilot design when null edge subcarriers are present.

9.1 Introduction

Orthogonal frequency division multiplexing (OFDM) is a popular method in wireless high-speed communications schemes [118]. Pilot symbol assisted modulation (PSAM) was proposed as a low complexity technique to estimate multipath channels and to remove their effects from the received OFDM symbol [25]. More recently, attention has been paid to optimal pilot design for channel estimation performance in OFDM. In [78], it was demonstrated that the mean squared error (MSE) minimizing pilot design consists of equi-spaced equi-powered pilots. Other pilot design criteria have been considered as well: in [24] for bit error rate (BER) minimization, in [73] for channel estimate MSE minimization, in [58] for multiple-input multiple-output (MIMO) preamble pilot design, in [38] for channel tracking performance, in [63] for Doppler spread mitigation, in [2] for channel capacity maximization, in [37] for multiuser pilot design, in [23] for MIMO channel capacity maximization, in [66] for MIMO channel estimate MSE minimization, and in [9, 10, 3] for peak-to-average

power ratio (PAR) reduction. A thorough overview of PSAM can be found in [110]. In this chapter, we will address optimal pilot designs in ODFM systems that have edge null subcarriers.

In almost all wireless communications standards, a transmitted signal is required to meet a spectral mask such that the power spectrum outside of the main user's channel is not too high, thus limiting the amount of distortion noise contributed to adjacent and alternate channel users. Such interference results from spectral splattering caused by system nonlinearities from the power amplifier, the mixer, the DAC, etc. Accordingly, many OFDM standards (digital audio broadcasting (DAB), digital video broadcasting (DVB), wireless LAN, wireless MAN, etc.) require that a certain number of subcarriers at each band edge remain unmodulated. These unmodulated (or "null") subcarriers make it easier for system designers to meet the spectral mask constraints [101]. As we will show, when a segment of the bandwidth is not available for pilot placement, as is the case in null-subcarrier OFDM systems, the pilot design problem needs to be readdressed.

When the entire OFDM band is available (i.e., no null subcarriers are present), it was proved in [78] that the optimal pilot design consists of evenly-spaced constant-power pilots. In this work we are interested in determining the optimal pilot design when null edge subcarriers are present. If the null subcarriers occupy a larger bandwidth than the spacing required by the evenly-spaced pilot design, then evenly spacing the pilot subcarriers is no longer feasible, and another solution needs to be found as acknowledged in [78] and [73]. Also, in [84], a proposal was made for selecting the pilot positions in OFDM preambles when null subcarriers are present. However, the method of [84] does not work for certain subcarrier/channel-length configurations; moreover, the optimization in [84] uses the ℓ_2 norm of the subcarrier channel-estimate MSEs, which may not accurately encapsulate the system performance.

Our proposed solution uses a cubic parameterization of the pilot subcarrriers in conjunction with a convex optimization algorithm to produce pilot designs that have near-optimal *symbol* estimate MSE performance as defined by *any* convex norm of the subcarrier symbol-estimate MSEs. In the example designs we show the effect of using different norm choices.

Additionally, through a design example based on the IEEE 802.16 standard [1], we demon-strate the performance improvement possible for null-subcarrier OFDM systems when the proposed pilot design is used instead of the conventional evenly-spaced pilot design.

Notations: Upper case and lower case bold face letters represent matrices and column vectors respectively; $\mathbf{A}^T$ and $\mathbf{A}^{\mathcal{H}}$ stand for the transpose and the Hermitian transpose of $\mathbf{A}$, respectively; $\mathrm{E}[\cdot]$ is the expectation operator; $\|\mathbf{x}\|_n$ is the ℓ_n norm of $\mathbf{x}$; $|\mathbf{x}|$ $(|\mathbf{A}|)$ is a vector (matrix) that is the element-wise magnitude of $\mathbf{x}$ $(\mathbf{A})$; $\mathbf{A}^+ = (\mathbf{A}^{\mathcal{H}}\mathbf{A})^{-1}\mathbf{A}^{\mathcal{H}}$ is the pseudoinverse of matrix $\mathbf{A}$; $|\mathcal{A}|$ is the cardinality of set $\mathcal{A}$; $((\cdot))_N$ is the modulo N operation; $\mathrm{int}(\cdot)$ rounds the argument to the nearest integer; $\mathbf{D}_{\mathbf{x}}$ is a diagonal matrix with vector $\mathbf{x}$ on the diagonal; $[\mathbf{A}]_{i,k}$ denotes entry in the ith row and the kth column of $\mathbf{A}$; finally, the $N \times N$ discrete Fourier transform (DFT) matrix is denoted by $[\mathbf{Q}]_{k,n} = N^{-1/2} \exp(-j2\pi(n-1)(k-1)/N)$, $1 \le k, n \le N$.

OFDM model: A PSAM OFDM system with null edge subcarriers is assumed in this chapter. The pilot, null and data subcarrier indices can be grouped into three disjoint sets, $\mathcal{K}_p$, $\mathcal{K}_n$ and $\mathcal{K}_d$, respectively, that span all N baseband subcarriers indices. The frequency domain symbol is

$$\mathbf{x} = [x_1, x_2, ..., 0, 0, ..., 0, ..., x_{N-1}, x_N]^T, \tag{9.1}$$

where x_k is chosen to be a scaled version of an element from a finite constellation in the complex domain, $\mathcal{A} = \{a_1, a_2, ..., a_{|\mathcal{A}|}\}$ such that $\mathrm{E}\left[\|\mathbf{x}\|_2^2\right] = \mathcal{E}_s$, where $\mathcal{E}_s$ is the total transmitted symbol energy.

The received baseband frequency-domain signal after synchronization and cyclic prefix (CP) removal is

$$\mathbf{y} = \mathbf{D}_{\mathbf{h}}\mathbf{x} + \mathbf{w}, \tag{9.2}$$

where $\mathbf{w}$ is additive white complex Gaussian noise with autocovariance matrix $\sigma_w^2 \mathbf{I}_N$ and $\mathbf{h}$ is the frequency response of the channel. Note that $\mathbf{h} = \mathbf{Q}_L \mathbf{h}^{(t)}$, where $\mathbf{h}^{(t)}$ is a length-L vector of the channel impulse response and $\mathbf{Q}_L$ is the first L columns of the DFT matrix $\mathbf{Q}$.

The received pilot subcarriers can now be expressed as

$$\mathbf{y}_p = \mathbf{D}_{\mathbf{h}_p}\mathbf{x}_p + \mathbf{w}_p. \qquad (9.3)$$

Define $\mathbf{x}_p$ as a vector containing elements from $\mathbf{x}$ with indices in $\mathcal{K}_p$; vectors $\mathbf{y}_p$, $\mathbf{w}_p$ and $\mathbf{h}_p$ are similarly defined. Denote the portion of the DFT matrix that translates $\mathbf{h}^{(t)}$ to the pilot subcarriers by

$$\mathbf{Q}_p \triangleq [\mathbf{Q}]_{\mathcal{K}_p,\ \{1,2,\dots,L\}}, \qquad (9.4)$$

so that $\mathbf{Q}_p \in \mathbb{C}^{|\mathcal{K}_p|\times L}$. Let $\mathbf{h}_p = \mathbf{Q}_p\mathbf{h}^{(t)}$.

Denote the channel estimate over the data subcarriers as $\hat{\mathbf{h}}_d$, which can be generated using the matrix

$$\mathbf{Q}_d \triangleq [\mathbf{Q}]_{\mathcal{K}_d,\ \{1,2,\dots,L\}}, \qquad (9.5)$$

so that $\mathbf{Q}_d \in \mathbb{C}^{|\mathcal{K}_d|\times L}$. Let $\hat{\mathbf{h}}_d = \mathbf{Q}_d\hat{\mathbf{h}}^{(t)}$. The transmitted constellation points can be estimated by

$$\hat{\mathbf{x}}_d = \arg\min_{\mathbf{a}\in\mathcal{A}^{|\mathcal{K}_d|}} \left\|\mathbf{y}_d\mathbf{D}_{\mathrm{E}[|\mathbf{x}_d|^2]}^{-1/2} - \hat{\mathbf{h}}_d\mathbf{a}\right\|_2, \qquad (9.6)$$

where $\mathcal{A}^{|\mathcal{K}_d|}$ is a $|\mathcal{K}_d|$ dimensional vector space containing elements from the set $\mathcal{A}$. Define $\mathbf{x}_d$ as a vector containing elements from $\mathbf{x}$ with indices in $\mathcal{K}_d$; vectors $\mathbf{y}_d$ and $\mathbf{h}_d$ are similarly defined. Implicit in (9.6) is that the accuracy of the channel estimate only matters in the data subcarriers. In other words, the accuracy of $[\hat{\mathbf{h}}]_k$ for $k \notin \mathcal{K}_d$ is irrelevant as it does not effect the data symbol estimation performance.

9.2 Channel Estimation

The procedure used to estimate the channel in a PSAM OFDM system varies depending on a number of factors including computational resources and knowledge of the channel statistics. In this chapter, we examine least-squares error (LSE) channel estimation, which requires no knowledge of the channel statistics and treats the channel taps as unknown deterministic variables. It was shown in [73] that LSE estimation achieves the Cramér-Rao bound. When some knowledge of the channel statistics is available, it is possible to use more accurate equalizer structures such as Bayesian channel estimation [54, p. 532], but this increased

accuracy comes at the expense of higher complexity and increased overhead. Methods have been proposed to reduce the complexity of Bayesian channel estimation [120, 39], but LSE estimation is still desirable for cases when the channel auto-covariance matrix is unknown. Also, other more complicated two-dimensional channel estimation techniques are possible that incorporate the time variations in the channel, see [61, 100]. In this chapter, we focus on the problem of channel estimation for null-subcarrier OFDM using pilots and an LSE estimator and assume the channel is approximately constant over one OFDM symbol, but can change from symbol to symbol.

If the channel statistics are unknown, then the channel impulse response can be treated as an unknown length-L deterministic vector[1]. The goal of channel estimation is to estimate this vector with as much accuracy as possible. By rewriting (9.3) as $\mathbf{y}_p = \mathbf{D}_{\mathbf{x}_p}\mathbf{Q}_p\mathbf{h}^{(t)} + \mathbf{w}_p$ and using the definition of $\mathbf{h}_d$, we can show that the LSE of the channel response in the data subcarriers is [54, p. 523],

$$
\begin{aligned}
\hat{\mathbf{h}}_d &= \underbrace{\mathbf{Q}_d \left(\mathbf{Q}_p^{\mathcal{H}} \mathbf{D}_{\mathbf{x}_p}^{\mathcal{H}} \mathbf{D}_{\mathbf{x}_p} \mathbf{Q}_p \right)^{-1} \mathbf{Q}_p^{\mathcal{H}} \mathbf{D}_{\mathbf{x}_p}^{\mathcal{H}}}_{\mathbf{P}} \mathbf{y}_p \\
&= \mathbf{h}_d + \mathbf{P}\mathbf{w}_p.
\end{aligned}
\tag{9.7}
$$

Following the lead from [78], in this chapter we require the number of pilots be at least the length of the channel impulse response vector i.e. $|\mathcal{K}_p| \geq L$. In LSE estimation, if this condition is not met, then the channel estimate in (9.7) will not be unique because the system of equations will be under determined.

Notice that this estimate in (9.7) does not require $\mathbf{x}_p$ to be drawn from any specific constellation. Instead, the requirement is that the receiver know the pilots sent by the transmitter so that $\mathbf{D}_{\mathbf{x}_p}$ and $\mathbf{Q}_p$ can be generated from the complex values modulating

---

[1]Strictly speaking the channel impulse response is only an approximation of the time-domain channel function. When the multipath impulses do not fall in the discrete sampling grid, the channel impulse response function will be infinite length and can not be captured with an length-L vector [113]. A discrete cosine transform-based method has been proposed to mitigate this problem in [122]. Also, in [70] a method was presented to resample a multipath profile so that it contains a finite number of channel taps after resampling while preserving the RMS delay spread of the channel. In this work, we assume that the tails of the impulse response function are negligible beyond L samples, which is also the assumption made in OFDM to justify that no ISI occurs.

$\mathbf{x}_p$ and the positions of the pilots $\mathcal{K}_p$, respectively. Furthermore, the complexity of this estimator is not dependent on the values of $\mathbf{x}_p$ or $\mathcal{K}_p$. All that is required is that the pilot design, as specified completely by $\mathbf{x}_p$ and $\mathcal{K}_p$, be known to both the transmitter and receiver.

Define the channel estimation error, $\boldsymbol{\zeta} \triangleq \hat{\mathbf{h}}_d - \mathbf{h}_d = \mathbf{P}\mathbf{w}_p$. It is straightforward to obtain its autocovariance matrix as

$$
\begin{aligned}
\mathbf{R}_{\boldsymbol{\zeta}} &= \mathrm{E}\left[\mathbf{P}\mathbf{w}_p\mathbf{w}_p^{\mathcal{H}}\mathbf{P}^{\mathcal{H}}\right] \\
&= \sigma_w^2 \mathbf{Q}_d \left(\mathbf{Q}_p^{\mathcal{H}}\mathbf{D}_{\mathbf{x}_p}^{\mathcal{H}}\mathbf{D}_{\mathbf{x}_p}\mathbf{Q}_p\right)^{-1} \mathbf{Q}_d^{\mathcal{H}}.
\end{aligned}
\tag{9.8}
$$

Of interest are the diagonal elements of the autocovariance matrix, $\mathbf{z} \triangleq \mathrm{diag}\{\mathbf{R}_{\boldsymbol{\zeta}}\}$, as they correspond to the variance of the channel estimate in each of the data subcarriers.

9.2.1 Data Subcarrier Estimation MSE

Using the criterion in (9.6), the metric that quantifies the data symbol estimation error is

$$
\boldsymbol{\epsilon} \triangleq \mathbf{D}_{\mathrm{E}[|\mathbf{x}_d|^2]}^{-1/2}(\mathbf{y}_d - \mathbf{D}_{\hat{\mathbf{h}}_d}\mathbf{x}_d).
\tag{9.9}
$$

When the LSE channel estimates are used, $\boldsymbol{\epsilon}$ conditioned on $\mathbf{x}_p$ is complex Gaussian distributed with zero mean and autocovariance matrix

$$
\mathbf{R}_{\boldsymbol{\epsilon}} = \mathbf{D}_{\mathbf{z}} + \sigma_w^2 \mathbf{D}_{\mathrm{E}[|\mathbf{x}_d|^2]}^{-1}, .
\tag{9.10}
$$

Define $\mathbf{e} \triangleq \mathrm{diag}\{\mathbf{R}_{\boldsymbol{\epsilon}}\}$.

The probability of bit error is a function of some norm of $\mathbf{e}$ that is dependent on the channel statistics. In the following analysis we use an objective function that is the ℓ_∞ norm of $\mathbf{e}$, $\|\mathbf{e}\|_\infty$, but the optimization can easily be extended to any convex norm of $\mathbf{e}$, including the frequently-used ℓ_2 norm, by simply redefining the objective function. Using the ℓ_∞ in the objective function has the advantage that the optimized pilot placement will produce a constant channel estimate error across all data subcarriers. For the case where there are no null subcarriers, the optimal equal-spaced pilot placement is MSE-optimal in both the ℓ_2 and ℓ_∞ norms because it produces a constant channel estimate performance across all subcarriers. A good comparison of various MSE objective function norm choices

can be found in [86]. Later, in Section 9.4, we illustrate how the performance is affected by the objective function norm choice.

Thus, the optimization problem that needs to be solved is

$$\arg \min_{\mathrm{E}[|\mathbf{x}|^2], \ \mathcal{K}_p} \quad \|\mathbf{e}\|_\infty$$
$$\text{subject to} \quad \mathrm{E}\left[\|\mathbf{x}\|_2^2\right] = \mathcal{E}_s,$$
$$\mathbf{x}_n = \mathbf{0}_{|\mathcal{K}_n| \times 1}. \tag{9.11}$$

In other words, the optimization variables are the distribution of power among the non-zero subcarriers $\mathrm{E}[|\mathbf{x}|^2]$, the power allocated to the pilots[2] and the positions of the pilot subcarriers $\mathcal{K}_p$, which along with $\mathcal{K}_n$ dictate the positions of the data subcarriers $\mathcal{K}_d$. The constraints are that the total symbol power be bounded by $\mathcal{E}_s$ and that the null subcarriers are set to zero. The objective function is discontinuous in the optimization variable $\mathcal{K}_p$. Therefore (9.11) is a non-convex optimization problem which is difficult to solve [21]. Next we propose to parameterize the pilot spacings and employ convex optimization techniques to produce a near optimal solution to (9.11).

9.3 LSE Pilot Design

In order to simplify the optimization problem in (9.11), we propose that it be split into two independent optimization problems that can be solved successively to find a near-optimal solution to (9.11): i) find a set of pilot subcarrier indices, $\mathcal{K}_p$, that make practical sense; ii) using this $\mathcal{K}_p$ as an additional constraint in (9.11), minimize the symbol estimate MSE, $\mathbf{e}$.

9.3.1 Pilot Position Parametrization

For small values of $|\mathcal{K}_p|$ and $N - |\mathcal{K}_n|$, it may be possible to exhaustively search all the possibilities of $\mathcal{K}_p$ to find the one that solves (9.11). But when $|\mathcal{K}_p|$ and $N - |\mathcal{K}_n|$ become moderately large, searching the $\binom{N-|\mathcal{K}_n|}{|\mathcal{K}_p|}$ possibilities of $\mathcal{K}_p$ becomes intractable. For instance, with $N - |\mathcal{K}_n| = 192$ and $L = 16$, $\binom{192}{16} \approx 10^{23}$.

Our goal is to limit the search space for $\mathcal{K}_p$ to only a relatively small number of reasonable possibilities. To do this, we propose to parameterize the pilot positions by a cubic

---

[2]It is assumed that the power in the pilot subcarriers is deterministic, so that $\mathrm{E}\left[|\mathbf{x}_p|^2\right] = |\mathbf{x}_p|^2$.

polynomial. Note that equal pilot spacing implies that the pilot positions are described by a linear function, i.e., a first order polynomial. Thus, to allow unequal pilot spacing and to ensure a certain degree of parsimony, it is reasonable to consider parametric modeling of the pilot spacing using other low order polynomials. It is desirable to have the pilots symmetric with respect to the center of the band - this requirement rules out the quadratic polynomial design since a second order polynomial cannot be symmetric. A cubic polynomial parameterization is therefore the next logical design.

First, we need to find a one-to-one mapping that relates the set of indices $\mathcal{K}$ to the set of "subcarrier numbers" $\mathcal{S}$, where $\mathcal{S}$ is a circularly shifted version of $\mathcal{K}$ with a domain in the integers of $[-N/2 + 1, N/2]$. Specifically, $\mathcal{S} = f(\mathcal{K})$ where

$$f(\mathcal{K}) \triangleq ((\mathcal{K} - N + 1))_N - N/2 + 1. \tag{9.12}$$

If the domain of f is restricted to $[1, N]$, then f is a one-to-one mapping so that $\mathcal{K} = f^{-1}(\mathcal{S})$. With $\mathcal{S}$, the data and pilot subcarrier numbers, $\mathcal{S}_d \bigcup \mathcal{S}_p$, are continuous over the integers (this is not the case with $\mathcal{K}$ because the null indices $\mathcal{K}_n$ occupy the middle segment of $\mathbf{x}$).

The goal is to find a cubic function, $g(\cdot)$, that maps the integers in $[0, |\mathcal{K}_p| - 1]$ to a set of possible pilot subcarrier numbers, $\mathcal{S}_p$. Once $\mathcal{S}_p$ is found through $g(\cdot)$, we can use $f^{-1}(\cdot)$ to find $\mathcal{K}_p$ and finally, use $\mathcal{K}_p$ to solve the segmented optimization problem discussed at the beginning of Section III. This process will be performed iteratively over all permissible values of

$$\mathcal{K}_p = \left\{ \text{int} \left(f^{-1} \circ g(\tau) \right) \middle| \tau \in \{0, 1, 2, ..., |\mathcal{K}_p| - 1\} \right\} \tag{9.13}$$

until the minimizing set is found. The cubic function that parameterizes the pilot subcarrier positions has the form

$$g(\tau) = a_3 \tau^3 + a_2 \tau^2 + a_1 \tau + a_0. \tag{9.14}$$

The pilots have to be placed in a non-null subcarrier (i.e. an in-band subcarrier). We further constrain $g(\tau)$ by assuming that the pilots are placed symmetrically about the center of the in-band region. Moreover, we assume that the pilots are placed sequentially from left to right, i.e., $g(\tau)$ has a positive slope. To further explain these constraints, let us define the number of in-band subcarriers, $N_i \triangleq |\mathcal{S}_p \bigcup \mathcal{S}_d|$. It is necessary to have int $\left(f^{-1} \circ g(\tau) \right) \notin \mathcal{K}_n$,

114

which means $g(\tau) \in [-(N_i - 1)/2, (N_i + 1)/2]$. The middle of the in-band region is at $1/2$. Mathematically, the constraint equations are

$$g\left(\frac{|\mathcal{K}_p| - 1}{2}\right) = 1/2 \tag{9.15}$$

$$g(0) = -(N_i - 1)/2 + \delta \tag{9.16}$$

$$g(|\mathcal{K}_p| - 1) = (N_i + 1)/2 - \delta \tag{9.17}$$

$$g'(\tau) > 0, \tag{9.18}$$

In the constraint equations, δ represents how far the edge pilots are from the in-band edges. For example, $\delta \in (0, 1]$ would mean the edge pilots are placed at the in-band edge, while $\delta \in (1, 2]$, would place the edge pilots one subcarrier from the in-band edge. Using the constraint equations in (9.15)-(9.18) and the fact that the edge pilots should not be spaced further from the in-band edge than the average pilot spacing, it is possible to eliminate three of the five variables and define a domain of the remaining two variables so that

$$a_0 = \delta - \frac{(N_i - 1)}{2} \tag{9.19}$$

$$a_1 = \frac{a_3(|\mathcal{K}_p| - 1)^3 + 2N_i - 4\delta}{2(|\mathcal{K}_p| - 1)} \tag{9.20}$$

$$a_2 = \frac{-3a_3(|\mathcal{K}_p| - 1)}{2} \tag{9.21}$$

$$\frac{-2(N_i - 2\delta)}{(|\mathcal{K}_p| - 1)^3} \leq a_3 \leq \frac{4(N_i - 2\delta)}{(|\mathcal{K}_p| - 1)^3} \tag{9.22}$$

$$0 < \delta \leq \frac{N_i}{|\mathcal{K}_p|}. \tag{9.23}$$

From (9.21), when $a_3 = 0$, $a_2 = 0$ as well; which means that $g(\tau)$ in (9.14) becomes a first order polynomial and the pilot spacing becomes even. From (9.14) and (9.21), we infer that

$$g''(\tau) = 6a_3\tau + 2a_2 \tag{9.24}$$

$$= 6a_3\left(\tau - \frac{|\mathcal{K}_p| - 1}{2}\right). \tag{9.25}$$

Therefore, when $a_3 < 0$, pilot spacing increases as τ goes from 0 to $\frac{(|\mathcal{K}_p| - 1)}{2}$, meaning that the pilot spacing at the edges of the in-band region are more closely spaced than the pilots in the middle of the in-band region. Conversely, when $a_3 > 0$ the outer pilots have a larger spacing than the pilots near the middle of the in-band region. Based on the results
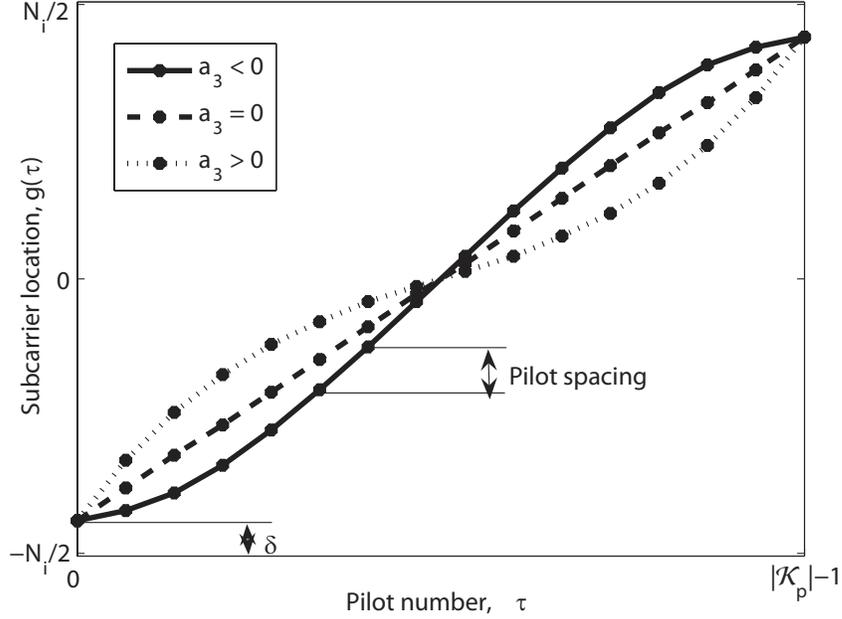
Figure 9.1: Plot of pilot subcarrier position for different values of a_3.

from [73], it is expected that $a_3 < 0$ will produce better pilot designs than $a_3 > 0$, which will be confirmed in Section 9.4 of this chapter. Fig. 9.1 is a plot of three example pilot parameterizations. In the plot the function $g(\tau)$ is plotted for different scenarios of a_3. The dots on each line indicate where the pilots would be placed.

9.3.2 Pilot Power

Assume that a set of plausible pilot indices generated with the cubic parametrization procedure from the last subsection is $\mathcal{K}_p$. If $|\mathcal{K}_p| = L$, i.e. $\mathbf{Q}_p$ as in (9.4) is square, then it is possible to write

$$\mathbf{z} = \text{diag}\left\{\sigma_w^2 \mathbf{Q}_d \mathbf{Q}_p^{-1} \mathbf{D}_{|\mathbf{x}_p|^{-2}} \mathbf{Q}_p^{\mathcal{H}-1} \mathbf{Q}_d^{\mathcal{H}}\right\}. \tag{9.26}$$

When $|\mathcal{K}_p| > L$, (9.26) can be rewritten using pseudoinverses as

$$\mathbf{z} = \text{diag}\left\{\sigma_w^2 \mathbf{Q}_d \mathbf{Q}_p^{+} \mathbf{D}_{|\mathbf{x}_p|^{-2}} \mathbf{Q}_p^{\mathcal{H}+} \mathbf{Q}_d^{\mathcal{H}}\right\} \tag{9.27}$$

as long as the power in the pilot subcarriers are constant (i.e. $[|\mathbf{x}_p|]_k = C \ \forall k$). However, since the pilot power in each subcarrier is not necessarily the same, it is necessary to use

the approximation

$$
\begin{aligned}
\mathbf{z} &\approx \operatorname{diag}\left\{\sigma_w^2 \mathbf{Q}_d \mathbf{Q}_p^+ \mathbf{D}_{|\mathbf{x}_p|^{-2}} \mathbf{Q}_p^{\mathcal{H}+} \mathbf{Q}_d^{\mathcal{H}}\right\} \\
&= \sigma_w^2 \underbrace{\left|\mathbf{Q}_d \mathbf{Q}_p^+\right|^2}_{\mathbf{A}} \underbrace{|\mathbf{x}_p|^{-2}}_{\mathbf{u}},
\end{aligned}
\tag{9.28}
$$

where $\left|\mathbf{Q}_d \mathbf{Q}_p^+\right|^2$ is the element-wise magnitude square of the matrix $\mathbf{Q}_d \mathbf{Q}_p^+$. From (9.28), it is clear that the channel estimate MSE, $\mathbf{z}$, is linear in $|\mathbf{x}_p|^{-2}$ (which is the element-wise exponentiation of the vector). This decomposition/expansion of the channel-estimate MSEs is novel and it is what allows the optimization problem to be convex. For instance, in order to find the pilot design that minimizes the maximum channel estimate MSE (or average channel estimate MSE, using the ℓ_2 norm), we need to assume that a plausible set of pilot subcarriers $\hat{\mathcal{K}}_p$ is found using the procedures from Section 9.3.1. With $\hat{\mathcal{K}}_p$, the pilot powers can be found by solving

$$
\begin{aligned}
\underset{\mathbf{u}}{\arg\min} \quad & \|\mathbf{A}\mathbf{u}\|_\infty \\
\text{subject to} \quad & \sum_{k=1}^{|\mathcal{K}_p|} \frac{1}{[\mathbf{u}]_k} = \mathcal{E}_p, \\
& \mathcal{K}_p = \hat{\mathcal{K}}_p, \\
& [\mathbf{u}]_k > 0 \ \forall \ k,
\end{aligned}
\tag{9.29}
$$

where $\mathcal{E}_p$ is the total power allocated to the pilots. Determining the channel estimate MSE minimizing pilot design is useful, but there are two main drawbacks to considering the pilot power design and the symbol power design separately: i) even with this channel estimate MSE minimizing design, the channel estimate MSEs will not be constant over all of the data subcarriers, which means the symbol estimate MSE will differ from subcarrier to subcarrier causing a non-constant quality of service across subcarriers; ii) the pilot power embedding ratio

$$
\beta = \frac{\|\mathbf{x}_p\|_2^2}{\|\mathbf{x}\|_2^2}
\tag{9.30}
$$

is not known for this proposed pilot design. Neither of these drawbacks are an issue when there are no null subcarriers present because the evenly-spaced equi-power design in that case guarantees a constant channel estimate MSE across the band and because the MSE

minimizing β has been derived in [85]. Thus, for the null subcarrier design we advocate using the symbol estimate MSE as the objective function to be minimized.

The additional free variable in the symbol estimate MSE design is the power allocated to the *data* subcarriers. As we will see in Section 9.4, by using the ℓ_∞ norm of the *symbol* estimate MSEs, we can produce an almost constant symbol estimate MSE over all of the data subcarriers.

9.3.3 Subcarrier Power

To extend the pilot power design to the full design, the symbol estimate MSE can be rewritten as

$$\mathbf{e} = \sigma_w^2 \big(|\mathbf{Q}_d \mathbf{Q}_p^+|^2 |\mathbf{x}_p|^{-2} + (\mathrm{E}\left[|\mathbf{x}_d|^2\right])^{-1}\big). \tag{9.31}$$

by substituting (9.28) into (9.10). It is possible to further simplify (9.31) by defining a new matrix $\mathbf{B} \in \mathbb{R}^{|\mathcal{K}_d| \times N_i}$ and vector $\mathbf{v} \in \mathbb{R}^{N_i \times 1}$ such that

$$\mathbf{e} = \sigma_w^2 \underbrace{\left[\ |\mathbf{Q}_d \mathbf{Q}_p^+|^2 \quad \mathbf{I}_{|\mathcal{K}_d| \times |\mathcal{K}_d|}\ \right]}_{\mathbf{B}} \underbrace{\left[\begin{array}{c} |\mathbf{x}_p|^{-2} \\ (\mathrm{E}\left[|\mathbf{x}_d|^2\right])^{-1} \end{array}\right]}_{\mathbf{v}} = \sigma_w^2 \mathbf{B}\mathbf{v}. \tag{9.32}$$

From (9.32), it is now obvious that the symbol estimate MSE $\mathbf{e}$ is linear in the vector $\mathbf{v}$. Once the optimizing $\mathbf{v}^\star$ is found it is straight forward to find the optimizing subcarrier powers $\mathrm{E}\left[|\mathbf{x}|^2\right]$.

Assume that a plausible set of pilot subcarriers $\hat{\mathcal{K}}_p$ is found using the procedures from Section 9.3.1. Using this pilot subcarrier set, we can simplify the optimization problem in (9.11) to

$$\begin{aligned} \arg\min_{\mathbf{u}} \quad & \|\mathbf{B}\mathbf{v}\|_\infty \\ \text{subject to} \quad & \sum_{k=1}^{|\mathcal{K}_d|} \frac{1}{[\mathbf{v}]_k} = \mathcal{E}_s, \\ & \mathcal{K}_p = \hat{\mathcal{K}}_p, \\ & [\mathbf{v}]_k > 0\ \forall\ k. \end{aligned} \tag{9.33}$$

This optimization problem is convex since the objective function is a convex norm of a

linear function and the constraint space is convex, thus it can be solved numerically using existing convex optimization software packages.

Now, the basic design procedure, which will be detailed in the next sub-section, is to solve (9.33) for all 'feasible' pilot subcarrier sets, $\hat{\mathcal{K}}_p$. The design chosen will be the one that minimizes $\|\mathbf{e}\|_\infty$.

9.3.4 Pilot Design Procedure

The overall pilot design procedures can be viewed as a grid search over the domain of (δ, a_3). Recall that the domain of (δ, a_3) is defined in (9.22) and (9.23). The pilot design procedure is outlined as a psuedo-code algorithm below

1. Initialize $i = 1$.

2. Select $\delta^{(i)}$ and $a_3^{(i)}$ in the domain defined by (9.22) and (9.23) and find $\hat{\mathcal{K}}_p^{(i)}$ according to (9.13).

3. Use $\hat{\mathcal{K}}_p^{(i)}$ to construct $\mathbf{B}^{(i)}$ via (9.32).

4. Solve (9.33) for $\|\mathbf{e^{(i)}}\|_\infty = \sigma_x^2 \|\mathbf{B}^{(i)}\mathbf{u}^{(i)}\|_\infty$.

5. If $\overline{MSE} > \|\mathbf{e}^{(i)}\|_\infty$ or $i = 1$, set $\overline{MSE} = \|\mathbf{e}^{(i)}\|_\infty$ and $\bar{i} = i$.

6. If $i = i_{max}$, exit, else, set $i = i + 1$ and go to Step 2.

When the algorithm exits, the optimizing values are $\mathbf{e}^\star = \mathbf{e}^{(\bar{i})}$, $\mathcal{K}_p^\star = \hat{\mathcal{K}}_p^{(\bar{i})}$ and $\mathbf{v}^\star = \mathbf{v}^{(\bar{i})}$. With these values, it is straightforward to find $\mathcal{K}_d^\star$ using the definition of the subcarrier sets and $\mathrm{E}\left[|\mathbf{x}|^2\right]^\star$ using the definition of $\mathbf{v}$ in (9.32). Notice that these 'optimal' values and sets will only be optimal among all cubic parameterizations of the pilot subcarriers and thus they may not be the globally optimal values. Nevertheless, the proposed solution is guaranteed to perform at least as well as the equi-spaced pilot design.

9.4 Pilot Design Optimization Example

For an example pilot design using the proposed procedure consider an OFDM system with N total subcarriers and $N/8$ null subcarriers on each band edge for a total of $N/4$ null

subcarriers. Thus there are $N_i = 3N/4$ in-band non-null subcarriers. This null carrier scenario is used for example purposes, but the scheme proposed in this chapter works for any number of null subcarriers. Of these in-band subcarriers, the number of pilot carriers and the number of data subcarriers will be varied in the following simulation examples. For all simulations, convex optimization problems were solved using [42]. The running time for all pilot optimizations was less than one hour running on a Windows PC with an Intel 1.6GHz processor and 1GB of RAM.

For the error rate simulations the channel is Rayleigh where each channel tap is i.i.d. complex Gaussian with zero mean and diagonal autocovariance matrix $[\mathbf{R}_{\mathbf{h}^{(t)}}]_{k,k} = Ae^{-0.1k}$, where $k \in \{1, 2, ..., L\}$ and A is a constant selected so that $\text{trace}\{\mathbf{R}_{\mathbf{h}^{(t)}}\} = 1$. Each error rate plot was generated using 100,000 channel realizations. Also, the channel is assumed to be independent from symbol to symbol. Recall that the proposed pilot design procedure is ambivalent to the statistics of the channel because it is based on LSE channel estimation.

9.4.1 Pilot positions

For the first example we have provided a plot in Fig. 9.2 of the maximum MSE $\|\mathbf{e}\|_\infty$ over a range of normalized a_3 values, where the NMSE is the MSE is normalized by the perfect channel state information (PCSI) MSE which results when the receiver has full knowledge of the channel. That is

$$
\begin{aligned}
NMSE &= \frac{\|\mathbf{e}\|_\infty}{MSE_{PCSI}} & (9.34) \\
&= \frac{\|\mathbf{e}\|_\infty |\mathcal{K}_d|}{\sigma_w^2 \mathcal{E}_s}. & (9.35)
\end{aligned}
$$

As the (9.34) indicates, MSE_{PCSI} is the MSE when no pilot energy is used; instead all energy is allocated to the data subcarriers. In this case, the NMSE can be thought of as the penalty paid for channel estimation and by definition, the lower bound on NMSE will be 0dB.

The normalization factor for a_3 is

$$
\gamma = \frac{2(N_i - 2\delta)}{(|\mathcal{K}_p| - 1)^3}, \tag{9.36}
$$

120
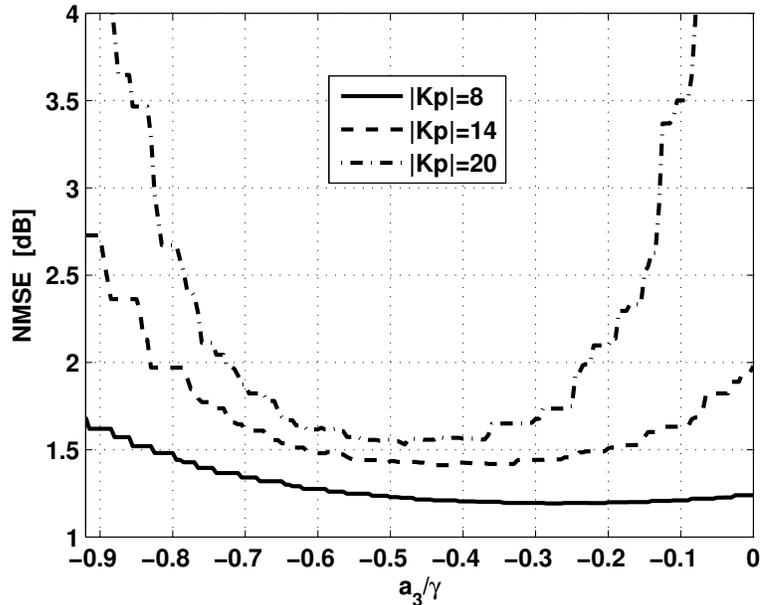
Figure 9.2: Plot of maximum symbol estimate NMSE versus a_3/γ.

which is the magnitude of the lower bound defined in (9.23). In the plot, $L = |\mathcal{K}_p|$. The resolution of the search grid was 0.01 in the δ dimension and 0.001 in the a_3 dimension. For all cases plotted, $|\mathcal{K}_n| > N/|\mathcal{K}_p|$, thus, as expected for the cases plotted, $\delta^\star = 0.01$. The lines plotted are precise and are not a result of simulation. The lack of smoothness in the lines comes from the fact that the maximum MSEs are a non-differentiable function of a_3.

In simulating Fig. 9.2, we compared the values of the MSE approximation in (9.28) and the true MSE from (9.8) which was used in the plot. We found that the difference between the two was always less than 0.1%, which indicates that for practical pilot scenarios, it is reasonable to use (9.28) in the pilot optimization objective function.

Symbol Power Profile: The PSD of the proposed design is plotted in linear scale in Fig. 9.3 where $N = 256$, $N_i = 192$ and $|\mathcal{K}_p| = L = 18$. With these parameters the proposed design has values $a_3 = -0.0371$ and $\delta = 0.01$. For both cases $\mathcal{E}_s = N_i$. Notice that for the proposed design the pilots near the band edges are spaced more closely together than the pilots near the middle of the band. Also, note that the power profile of the data subcarriers is not constant, but is instead chosen according to (9.33) so that the maximum
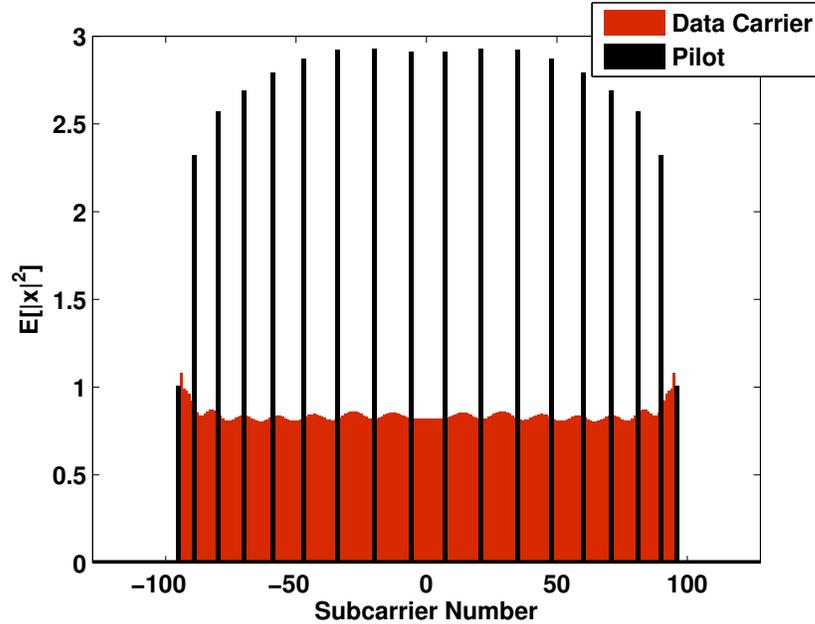
Figure 9.3: Proposed design power spectrum density in linear scale.

symbol estimate MSE is minimized. A similar phenomenon occurs when $|\mathcal{K}_p| > L$. In the proposed scheme, the receiver would need to know how the data subcarrier power profile varies so that $\mathrm{E}[|\mathbf{x}_d|^2]$ can be determined and the data can be properly decoded. Because all of the proposed design procedures are performed off line and are channel ambivalent, it is straightforward to store the power values in memory. Finally, as was mentioned in the introduction, PAR is often a concern in OFDM systems. In OFDM it is not desirable to have samples in the time domain that have significantly higher power than the average sample, as this will increase PAR. However, in the proposed scheme, the power profile is being altered in the frequency domain. After these frequency domain pilots are mixed through the IFFT operation, they should not adversely effect the PAR. There is a comprehensive derivation of the PAR distribution based on the signal PSD in [124], which shows that the PAR distribution is not sensitive to slight PSD deviations from the ideal flat band-limited OFDM PSD. In fact, several papers have shown that, if the phases on these pilot carriers is carefully selected, it may be possible to reduce the PAR [10, 9, 29].

Cubic Coefficient Optimization: Fig. 9.4 is a plot of the optimizing values of a_3, $a_3^\star$,
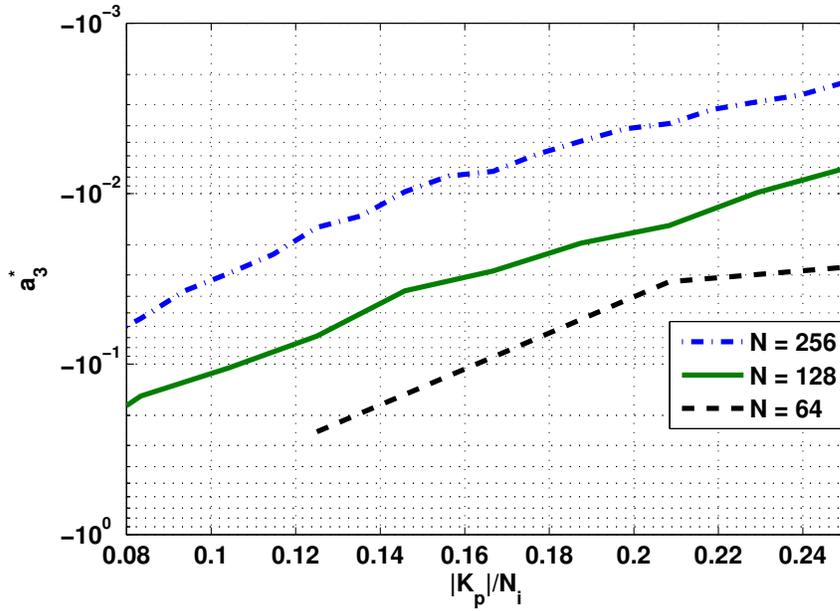
Figure 9.4: Plot of MSE-optimizing values $a_3^\star$, $L = |\mathcal{K}_p|$.

versus the ratio of pilot subcarriers to in-band subcarriers $|\mathcal{K}_p|/N_i$, where $|\mathcal{K}_p| = L$. The plot shows that the pilot spacing becomes more and more linear (i.e. a_3 approaches zero) as the number of pilot carriers increases. However, for all the values plotted, $a_3^\star$ is still negative which implies that the pilot carriers near the band edges should be more closely spaced than the center-band pilots.

Pilot Power Ratio: Fig. 9.5 is a plot of the ratio of pilot power to total power β defined in (9.30). Also plotted are the β values from [85],

$$\beta_{|\mathcal{K}_n|=0} = 1 - \frac{1}{1 + (N/L - 1)^{-1/2}} \tag{9.37}$$

which are MSE optimal when no null subcarriers are present. The plot demonstrates that for the null-subcarrier case, slightly more power should be allocated to the pilots than when all subcarriers are available. Thus, for the null carrier design the closed form expression in (9.37) should not be used.

Norm Choice & Channel Length Effect: So far, all of the simulations assume the channel length L is equal to the number of pilots, $|\mathcal{K}_p|$. This is the commonly used assumption when
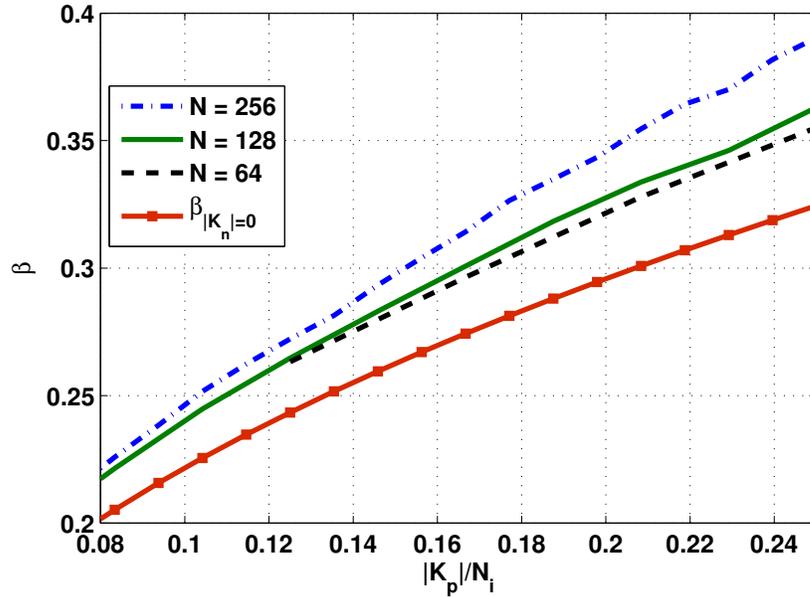
Figure 9.5: Plot of β for the proposed design, $L = |\mathcal{K}_p|$.

there is no channel state information. However, in practice, there may be scenarios when the channel length is known to be less than the number of pilots, that is, when $L < |\mathcal{K}_p|$. Ideally, the number of pilots should then be decreased to meet the channel length, but this is often not possible as the number of pilots are usually fixed as part of the communication standard. Despite this, it is possible to achieve some performance gains by using a value of L that is less than $|\mathcal{K}_p|$ in estimating the channel when it is known that the channel length does not exceed L.

The effect of this adjustment is plotted in Fig. 9.6 where the channel length L is varied for different numbers of pilots $L < |\mathcal{K}_p|$ where $N = 256$, $N_i = 192$. The plot shows that there will be some loss when more pilots are used than are needed. For example, the line corresponding $|\mathcal{K}_p| = 16$ has a lower (better) NMSE at L than either $|\mathcal{K}_p| = 28$ or $|\mathcal{K}_p| = 40$. This result is consistent with the equi-spaced pilot case, where in [78] a proof was provided showing that $|\mathcal{K}_p| = L$ minimizes the minimum ℓ_2 MSE. The plot also shows that the gap between the full-band equi-spaced pilot case where $N = N_i = 256$ is always less than 0.5dB. This can be considered the lower bound on the channel estimation performance as proved
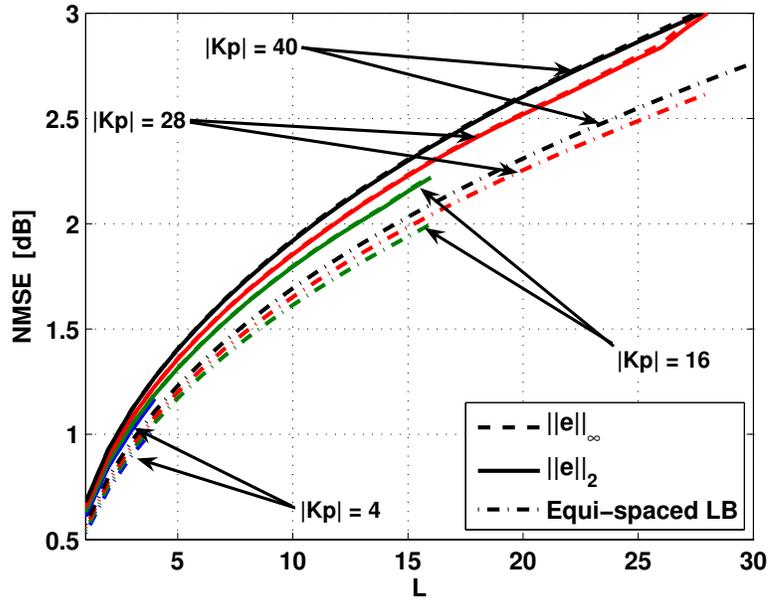
Figure 9.6: NMSE for versus the channel length L for different numbers of pilots $|\mathcal{K}_p|$. For the equi-spaced lower bound, $|\mathcal{K}_n| = 0$.

in [78].

Finally, the same plot also demonstrates the effect of using different norms in the objective function in (9.33). It is hard to distinguish the lines for the ℓ_∞ and ℓ_2 cases because they are almost equivalent. In fact, the difference is never greater than 0.01dB for all cases plotted. Such a narrow gap would imply that choosing one of these norms over the other is an unimportant choice. However, given the close performance gap slightly in favor of the ℓ_2 norm, the ℓ_∞ norm has the advantage of a constant quality of service over all subcarriers. The importance of having a constant MSE over all carriers varies with the application and channel code. The difference is probably only important when $|\mathcal{K}_p|$ is large, which causes the edge subcarriers to have much worse MSE than average when the ℓ_2 norm objective function is used. For comparison the NMSE across subcarriers is plotted in Fig. 9.7. For the $|\mathcal{K}_p| = 40$ case, the difference is about 2dB from the lowest NMSE carrier to the worst-case NMSE carrier near the band edge.
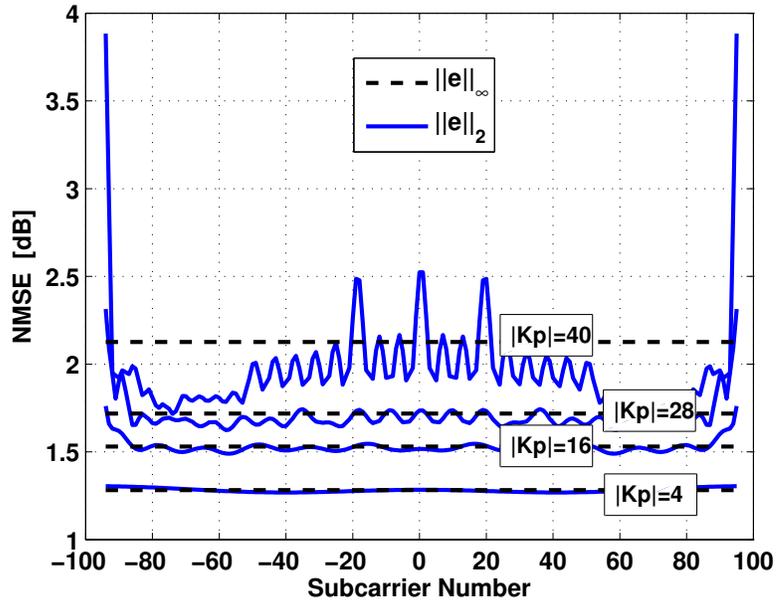
Figure 9.7: NMSE for versus number of pilots $|\mathcal{K}_p|$ for the ℓ_2 and ℓ_∞ norms versus the subcarrier number. $L = |\mathcal{K}_p|$ in all cases.

9.4.2 Comparisons

Typical Design: In order to assess the performance of the proposed pilot design, we chose to compare it to a "typical" pilot design named the "reference" design. For the reference design, $a_3 = 0$, $\beta = \beta_{|\mathcal{K}_n|=0}$ according to [85], all the pilots have a constant power and all of the data carriers have a constant power. Recall, that $a_3 = 0$ means that the pilots are evenly spacing in the in-band region. Also, for comparison, the pilot design proposed in [84] was generated. In [84], only the channel estimate MSE was considered, so to make the comparison fair, assume that all of the data carriers have constant power so that $\beta = \beta_{|\mathcal{K}|_n=0}$, which is MSE optimal for the full-band case.

The disadvantage of the design procedure in [84] is that it does not necessarily produce a viable pilot design. To review, the pilot positions in [84] are chosen to be the $|\mathcal{K}_p|$ highest-power subcarriers from the preamble design. In general, this procedure works well because there are usually exactly $|\mathcal{K}_p|$ distinct high-power subcarriers in the preamble design. However, this characteristic of the preamble design is not guaranteed. As one example, when
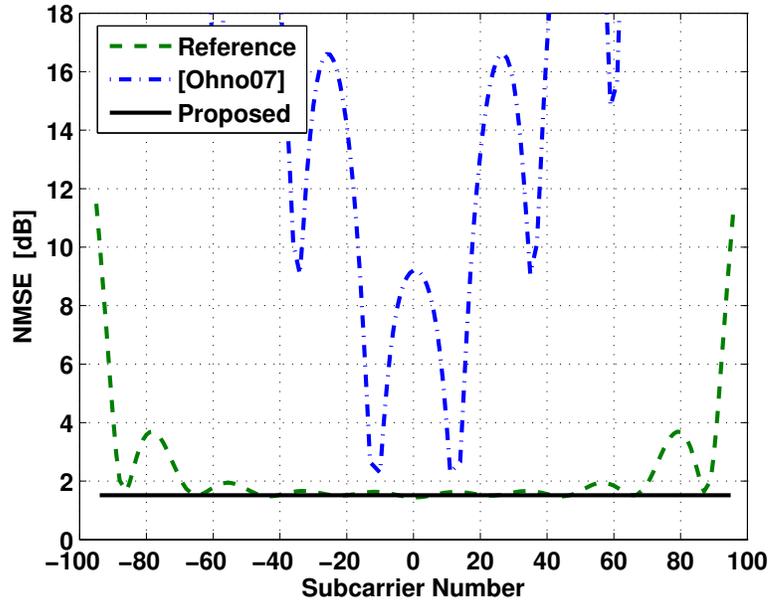
Figure 9.8: MSE profile where $L = |\mathcal{K}_p| = 10$. $\delta = 5$ for the reference design.

$N = 256$ and $|\mathcal{K}_p| = 10$ (or when $|\mathcal{K}_p| = 12$), the preamble design has spurious subcarriers in the center-band region that have higher power than the edge subcarriers. As a result the pilot design selected by the procedure in [84] has two adjacent pilots in the center-band region and no pilots at the edges of the in-band region, which produces catastrophic channel estimates. On the other hand, the design procedure proposed in this chapter will always produce a reasonable pilot design.

This effect is illustrated in Fig. 9.8, which is a plot of the symbol estimate MSE versus the subcarrier number, where $N = 256$ and $|\mathcal{K}_p| = L = 10$. From the plot it is clear that the design from [84], does not allow for effective symbol estimation. In fact, the MSE performance is worse than that of the reference design. In comparison, the design proposed in this chapter produces a flat MSE across all of the data subcarriers.

Fig. 9.9 is a plot of the MSE performance of the three designs when $N = 256$ and $|\mathcal{K}_p| = L = 18$. In this case, the design proposed in this chapter and the design proposed in [84] have almost identical performance. On the other hand, the MSE for the reference design is very poor near the band edges.
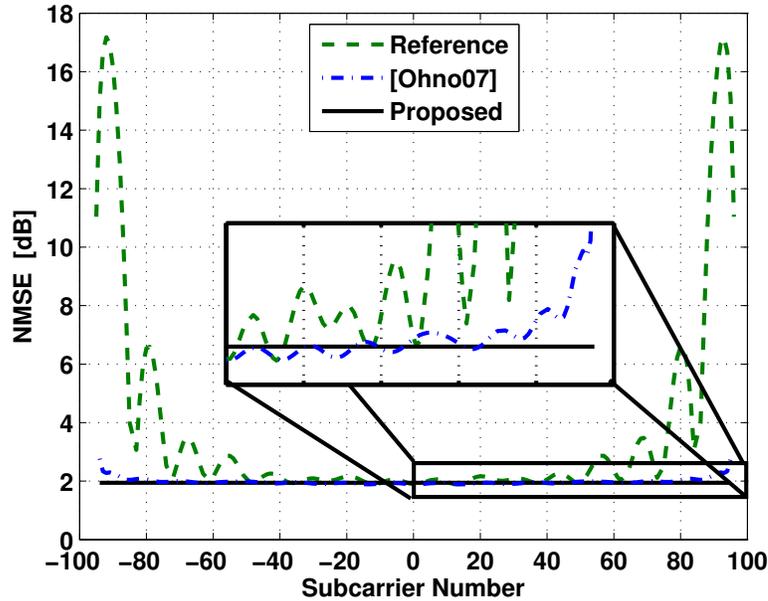
Figure 9.9: MSE profile where $L = |\mathcal{K}_p| = 18$. $\delta = 0.01$ for the reference design.

SER results: In Fig. 9.10 the uncoded symbol error rate (SER) of QPSK OFDM is plotted for the three pilot designs. For the plot, the Rayleigh fading channel described at the beginning of this section was used with $L = |\mathcal{K}_p|$. The SER performance of the proposed design is approximately 1dB worse than the PCSI case[3]. The plot also shows that the proposed design outperforms the reference design by about 1dB of SNR for the $L = 10$ case and more than 4dB of SNR for the $L = 18$ case. This performance gap is a result of the reference design having very poor channel estimates for the edge subcarriers. Finally, the design from [84] has almost identical performance as the proposed technique for the $L = 18$ case but is unusable for the $L = 10$ case.

IEEE 802.16 Improvement: In this subsection we explore the performance gains that could be realized if the pilots in IEEE 802.16 are rearranged according to the proposed design. The IEEE 802.16 standard contains three possible physical layer modes: Single carrier, OFDM, and orthogonal frequency division multiple access (OFDMA) [1]. Here, we

---

[3]In the PCSI case for this plot, $\beta = \beta_{|\mathcal{K}_n|=0}$ for the proposed pilot design. So despite PCSI, some energy is still allocated to the pilots, in order to make the comparisons realistic.
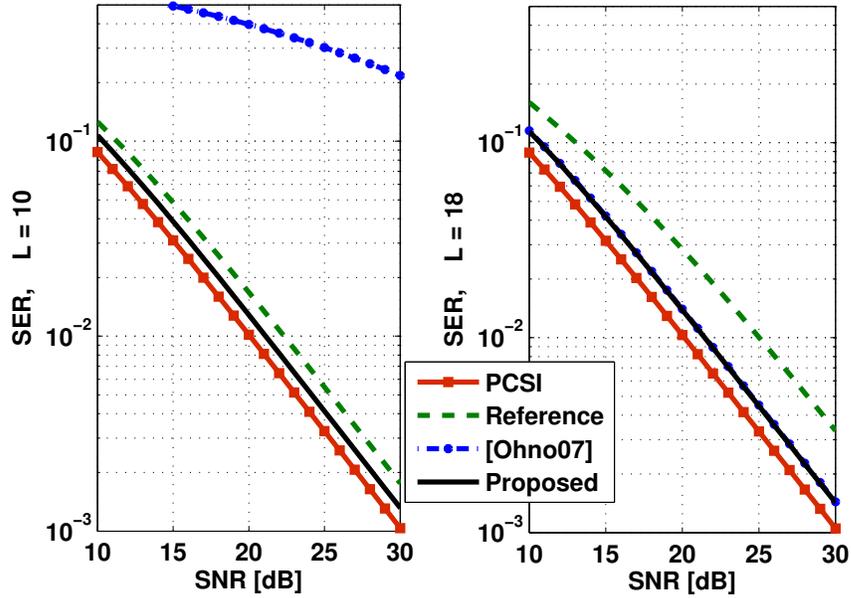
Figure 9.10: SER performance, $L = |\mathcal{K}_p|$.

focus only on the OFDM mode, but similar results can be realized for the other modes.

For IEEE 802.16 in OFDM mode [1, p. 427], the transmission frame is segmented into several parts. Of relevance here are the preamble and the data-carrying parts of the frame. The preamble is used for synchronization purposes including channel estimation. Additionally, each data-carrying symbol contains several pilots, which can be used for fine synchronization and also for channel estimation. In a data-carrying symbol 200 subcarriers of the 256 subcarrier window are used for data and pilots. Of the other 56 subcarriers, 28 are null in the lower-frequency guard band, 27 are nulled in the upper-frequency guard band and one is the DC subcarrier which is nulled. Of the 200 used subcarriers, 8 are allocated as pilots, while the remaining 192 are used for data transmission. The pilot positions specified by the standard are $\mathcal{K}_{p,OFDM} = \{-88, -63, -38, -13, 13, 38, 63, 88\}$, which all contain the same amount of power. Additionally, the pilot power ratio, β, is $\beta_{OFDM} = 1/25 = 0.04$. After solving the optimization problem in (9.33) using the 802.16 OFDM mode specifications, we find that $\hat{\mathcal{K}}_p = \{-100, -72, -43, -15, 15, 43, 72, 100\}$ for $L = 1$, $L = 4$ and $L = 8$ and that $\beta^\star_{L=1} = 0.067$, $\beta^\star_{L=4} = 0.124$ and $\beta^\star_{L=8} = 0.167$.
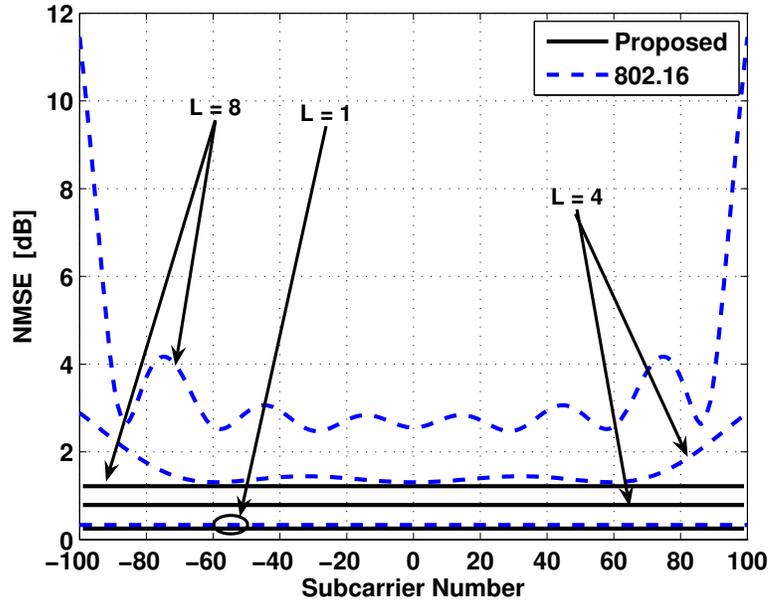
Figure 9.11: NMSE performance of IEEE 802.16 versus the proposed design. $|\mathcal{K}_p| = 8$ in all cases.

Fig. 9.11 is a plot of the NMSE of the proposed design and the 802.16 design. The plot shows that the standard pilot design does a poor job of estimating the symbols in the subcarriers near the guard band for $L > 1$. Conversely, the proposed pilot design is capable of a flat symbol estimate MSE across all data subcarriers.

Fig. 9.12, is a plot of the SER for the two pilot designs for different channel lengths using ideal interleaving and a (255, 239) Reed Solomon code as dictated by the 802.16 standard [1, p. 432]. The plot shows that, in an L-tap Rayleigh fading channel, the proposed pilot design leads to 3dB SNR improvement when $L = 8$ and a 1dB SNR improvement when $L = 4$.

All of the 802.16 results assume that the channel is estimated solely using the pilots in each symbol. In practice it may be possible to utilize the preamble symbol to help estimate the channel. However, in situations where the channel changes before the next preamble symbol is received, it is necessary to rely to the pilot aided channel estimates. In this case, as we have shown here, significant gains in 802.16 are possible with a simple reorganization
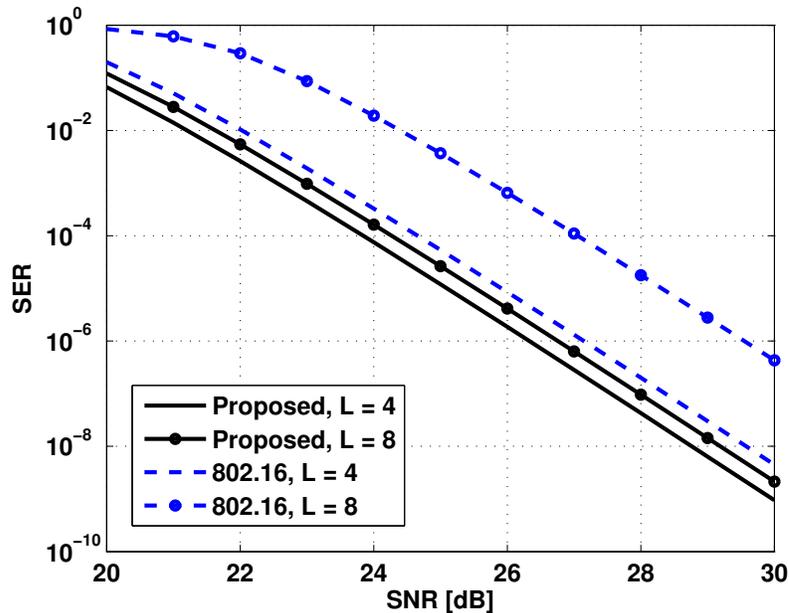
Figure 9.12: Reed-Solomon coded SER performance of IEEE 802.16 versus the proposed design. $|\mathcal{K}_p| = 8$ in all cases.

of the pilots.

9.5   Conclusions

In this chapter we discussed the problem of channel estimation in null-subcarrier OFDM. Specifically, we presented an optimization method for designing pilots in a PSAM null-subcarrier OFDM system for the case when the channel statistics are unknown (LSE estimation). The proposed method utilizes a cubic polynomial to define the pilot spacing and convex optimization techniques to obtain the pilot and data powers such that the symbol-estimate MSE is minimized.

Through an example pilot design it was demonstrated that significant improvements in the symbol-estimate MSE and SER are possible with the proposed pilot design over the reference design. Also, when the proposed design procedure is applied to an IEEE 802.16 system operating in OFDM mode up to 3dB of coded BER improvement can be realized. For systems with more null subcarriers, even larger improvements are possible. In summary, for null-subcarrier OFDM systems where the channel statistics are unknown,

131

large performance improvements can be realized by proper pilot design using the techniques proposed in this chapter.

CHAPTER X

RECEIVER NONLINEARITY OPTIMIZATION IN CLIPPING CHANNELS

In this chapter the effects of receiver nonlinearities are examined for clipping channels. The objective of this work is to determine the optimal receiver functions for additive noise clipping channels. In this case the optimal receiver function will be the one that maximizes the signal-to-noise-plus-distortion ratio (SNDR) of the received variable. To solve the problem we utilize functional analysis to find the SNDR-maximizing receiver function among all functions. The results are general and can be applied for any noise and signal distribution. Furthermore, the results show that for the examples given, the linear receiver is not SNDR-optimal.

10.1   Introduction

While it is common for communications channels to be assumed linear, there is almost always a nonlinear component to physical channels. The most obvious nonlinear characteristic of physical channels is their peak-limited nature [67]. Because it is impossible to drive a power amplifier (PA) with an infinite amount of power, there will be some limit to the peak power allowed by the channel.

The obvious question is how a transmitter should be designed when a peak limitation is imposed. This question is implicitly answered by the vast body of papers that discuss the "pre-distortion" of PA nonlinearities [111, 36, 90]. Typically, the term "pre-distortion" implies that an expanding nonlinear function is applied to signals before they reach the PA. The goal of predistortion is to have the concatenation of the predistortion function and the PA characteristic function be linear up to the saturation power of the PA; such a peak-limited linear function is known as a soft limiter. Implicit in all of this work is that the soft limiter is the most desirable transmit function. Note that in this paper we are only considering memoryless channels.

However, until [92] was published in 2005, it was not clear that the soft limiter was optimal in any sense. Fortunately, in [92], it was demonstrated that the soft limiter *with gain* is optimal in terms of the signal-to-noise-plus-distortion ratio (SNDR) when the gain is chosen correctly. SNDR optimality is an important goal because SNDR has been shown to be directed related to the bit error rate (BER) and capacity [34, 80, 82, 92, 90].

In this work we seek to determine the SNDR-optimal *recevier*-side functions in the presence of peak-limited channels. To accomplish this, we must first find an expression for the SNDR of additive noise channels with both transmitter and receiver memoryless functions. Next, we follow some functional analysis methods [41] to maximize the SNDR w.r.t to the receiver function.

Other work has considered channels where a receiver-side nonlinearity is used to compensate for a transmitter nonlinearity. Frequently these schemes are found in PAR reduction literature under the name of companding, which is a combination of the words **com**press and ex**pand** [117, 116, 50, 52]. In these schemes the receiver-side function is typically chosen to be the inverse of the transmitter function. The idea is that the signal will be compressed at the transmitter so as to avoid PA distortion and then expanded at the receiver with the inverse function to "undo" the compressing function. While this idea is intuitive, it was shown in [125] that using an inverse function pair is necessarily sub-optimal in terms of SNDR. In light of this, the obvious question is what are the SNDR-optimal receiver functions, which is the question this chapter seeks to answer.

10.2   SNDR Formulation

In [92], the SNDR is derived for any transmitter non-linear memoryless function. In this section we will extend the SNDR definition to system that have nonlinear function both before and after noise is added. That is where functions exist on both the transmitter and receiver side of the channel.

10.2.1   SNDR of Transmitter Functions

To start, we review the SNDR formulation for transmitter nonlinearities, which is the SNDR between output $y + v$ and input x in Fig. 10.1. Start by writing y in terms of x and a
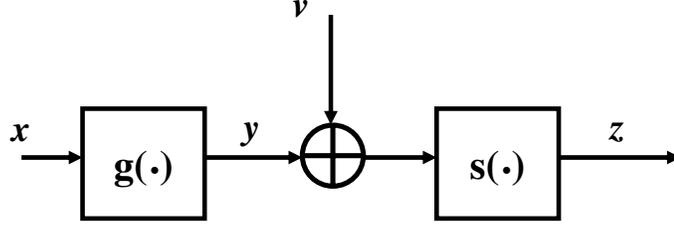
Figure 10.1: System diagram.

distortion term so that

$$y = g(x) = \alpha x + d, \tag{10.1}$$

where x is a random variable that is the input to the transmitter nonlinearity, $g(\cdot)$. In (10.1) α is chosen so that $E[dx^*] = 0$, where d is the distortion term which is also random. It is important to include α in the formulation so that the distortion term will be uncorrelated with the useful signal, x. Thus, we can calculate as

$$\alpha = \frac{E[yx^*]}{\sigma_x^2}. \tag{10.2}$$

Next, the variance of d is

$$E[|d|^2] = E[|y|^2] - |\alpha|^2 \sigma_x^2. \tag{10.3}$$

Step by step we have

$$\sigma_d^2 = E[|d|^2] \quad = \quad E[dd^*] \tag{10.4}$$

$$= \quad E[(y - \alpha x)(y - \alpha x)^*] \tag{10.5}$$

$$= \quad E[(y - \alpha x)(y^* - \alpha^* x^*)] \tag{10.6}$$

$$= \quad E[yy^* - \alpha xy^* - \alpha^* yx^* + \alpha\alpha^* xx^*] \tag{10.7}$$

$$= \quad E[|y|^2] - \alpha E[xy^*] - \alpha^* E[yx^*] + |\alpha|^2 \sigma_x^2 \tag{10.8}$$

$$= \quad E[|y|^2] - \frac{|E[yx^*]|^2}{\sigma_x^2}. \tag{10.9}$$

Finally,

$$SNDR_{x,y+v} = \frac{|E[yx^*]|^2}{\sigma_x^2 E[|y|^2] - |E[yx^*]|^2 + \sigma_x^2 \sigma_v^2}. \tag{10.10}$$

135

Which can be calculated by finding

$$E[yx^*] \quad = \quad E[g(x)x^*] = \int_{-\infty}^{\infty} g(x)x^* f_x(x) dx \tag{10.11}$$

$$E[|y|^2] \quad = \quad E[|g(x)|^2] = \int_{-\infty}^{\infty} |g(x)|^2 f_x(x) dx. \tag{10.12}$$

It may be necessary to calculated these integral numerically.

10.2.2 SNDR of Transmitter and Receiver Functions

The SNDR analysis in the previous subsection applies to all memoryless non-linear functions. Specifically, it is possible to use the Bussgang decomposition even when the function involves additive random variables. Thus, because the overall Tx-noise-Rx system can be view as a memoryless non-linear function, we can use the same formulation as was used for the Rx nonlinearity by simply replace all instances of y with z, so that

$$SNDR_{x,z} = \frac{|E[zx^*]|^2}{\sigma_x^2 E[|z|^2] - |E[zx^*]|^2}. \tag{10.13}$$

Here, $z = s(g(x) + v)$. We still need to calculate $E[zx^*]$ and $E[|z|^2]$ to determine the SNDR. However, since the non-linear function is in terms of the random variable v, we need to take the expectations over both v and x. To do this, we only need the joint density $f_{x,v}(x,v)$. If we can assume that x and v are independent then it will be possible to further simplify the joint pdf to a product of the individual pdfs, $f_{x,v}(x,v) = f_x(x)f_v(v)$. This assumption is made for all of the following analysis. Thus,

$$E[zx^*] \quad = \quad \int_{-\infty}^{\infty} \int_{-\infty}^{\infty} s(g(x) + v) x^* f_x(x) f_v(v) \ dx \ dv \tag{10.14}$$

$$E[|z|^2] \quad = \quad \int_{-\infty}^{\infty} \int_{-\infty}^{\infty} |s(g(x) + v)|^2 f_x(x) f_v(v) \ dx \ dv, \tag{10.15}$$

which should be simple to calculate numerically for any pair of functions, $g(\cdot)$ and $s(\cdot)$ and any pair of distributions, $f_x(x)$ and $f_v(v)$. In [92], it was possible to simply use the magnitude pdf to calculate these expectations. Here, that may not be possible because v and $g(x)$ may not add in-phase.

For verification, set $s(x) = x$ which results in

$$E[zx^*] \quad = \quad E[(g(x) + v)x^*] = E[g(x)x^*] \tag{10.16}$$

$$E[|z|^2] \quad = \quad E[|(g(x) + v)|^2] = E[|g(x)|^2] + \sigma_v^2. \tag{10.17}$$

Plugging these into (10.13) and the original SNDR expression in (10.10) follows.

In summary, the problem is to find the functions $g(\cdot)$ and $s(\cdot)$ that maximize

$$SNDR_{x,z} = \frac{|E[zx^*]|^2}{\sigma_x^2 E[|z|^2] - |E[zx^*]|^2},\tag{10.18}$$

where $E[zx^*]$ and $E[|z|^2]$ are defined in (10.14) and (10.15). Or, to be precise,

$$\underset{g(\cdot),\ s(\cdot)}{\text{maximize}} \quad SNDR_{x,z}[g(\cdot)\ , s(\cdot)]\tag{10.19}$$

When no constraints are placed on these functions the solution is straight forward: $g(x) = ax$ where $a \to \infty$ and $s(x) = x$; i.e. both functions are linear. Furthermore, when an average poser constraint is place on $g(x)$, such as $E[|g(x)|^2] \leq a$, then again the solution is two linear function, but with the gain of $g(\cdot)$ chosen so that the constraint is satisfied. As we will show, the problem is more complicated when a peak power constraint is places one or both of the functions., such as

$$\underset{g(\cdot),\ s(\cdot)}{\text{maximize}} \quad SNDR_{x,z}[g(\cdot),\ s(\cdot)]\tag{10.20}$$
$$\text{subject to} \quad \max_x |g(x)|^2 \leq 1.$$

In addition to jointly optimizing both functions, two possible sub problems can also be considered. One where the receiver function is known and the transmitter needs to be derived and the other where the transmitter function is known and the receiver is derived.

10.3 *Function Optimization*

In this we discuss the mathematics necessary to solve optimization problems w.r.t. functions. First, optimization w.r.t. variables is reviewed, then we review to analogous optimization w.r.t. functions.

10.3.1 Optimization With Respect to Variables

For some perspective, optimization is traditionally done w.r.t. variables. A typical problem may be

$$\underset{\mathbf{x}}{\text{minimize}} \quad f_o(\mathbf{x})\tag{10.21}$$
$$\text{subject to} \quad [f_{c1}(\mathbf{x}), f_{c2}(\mathbf{x}), ..., f_{cm}(\mathbf{x})]^T \leq \mathbf{0}_m,$$

where $\mathbf{x} = [x_1, x_2, ..., x_n]^T$ are optimization variables, $f_o(\cdot)$ is vector-valued objective function and $[f_{c1}(\mathbf{x}), f_{c2}(\mathbf{x}), ..., f_{cm}(\mathbf{x})]^T$ is a vector of vector-valued constraint functions. Many methods are available for solving these types of problems. For general functions that are not convex, random search or genetic algorithm methods may need to be implemented to find the solution. If the constraint space and the objective function are both convex, then interior point methods can be used to find the solution to arbitrary precision at low complexity.

The basic idea of the solution is to use an indicator function that has follows something like

$$I_c(\mathbf{x}) = \begin{cases} 0, & \{\mathbf{x} | [f_{c1}(\mathbf{x}), f_{c2}(\mathbf{x}), ..., f_{cm}(\mathbf{x})]^T \le \mathbf{0}_m\} \\ \infty, & else \end{cases}, \tag{10.22}$$

to turn the constrained problem into and unconstrained problem:

$$\underset{\mathbf{x}}{\text{minimize}} \quad f_o(\mathbf{x}) + I_c(\mathbf{x}). \tag{10.23}$$

Now, simple calculus can be employed and the solution is the $\mathbf{x}$ that satisfies

$$\frac{\partial f_o(\mathbf{x}) + \tilde{I}_c(\mathbf{x})}{\partial \mathbf{x}} = 0. \tag{10.24}$$

where $\tilde{I}_c(\mathbf{x})$ is an indicator function that is differentiable and approximates the ideal function in (10.22). It may be possible to find a closed-form solution to (10.24), but if it is not, Newton's method, which is an iterative numerical root-finding algorithm can be employed to solve the equation [21].

10.3.2 Optimization With Respect to Functions

A generalize functional optimization problem can be written as

$$\begin{aligned} \underset{g(\cdot)}{\text{maximize}} \quad & F_o(g(x)) \\ \text{subject to} \quad & [F_{c1}(g(x)), F_{c2}(g(x)), ..., F_{cm}(g(x))]^T \le \mathbf{0}_m, \end{aligned} \tag{10.25}$$

where $g(\cdot)$ is function to be optimized, $F_o(\cdot)$ is the objective *functional*, which is a function of functions and $[F_{c1}(g(x)), F_{c2}(g(x)), ..., F_{cm}(g(x))]^T$ is a vector of constraint *functional*s. The

solution exactly follows variable optimization. For simplicity, consider the unconstrained problem

$$\underset{g(\cdot)}{\text{maximize}} \quad F_o(g(x)). \tag{10.26}$$

Following the variable optimization, we need to solve

$$\frac{\partial F[g(x)]}{\partial g(x_0)} = 0 \tag{10.27}$$

for $g(\cdot)$. So the next step is to define the partial derivative of a functional. Again following variable calculus,

$$\frac{\partial F[g(x)]}{\partial g(x_0)} = \lim_{\epsilon \to 0} \frac{F[g(x) + \epsilon \delta(x - x_0)] - F[g(x)]}{\epsilon}. \tag{10.28}$$

From (10.28), we can derive the following properties

$$\frac{\partial g(x)}{\partial g(x_0)} = \delta(x - x_0) \tag{10.29}$$

$$\frac{\partial (g(x))^2}{\partial g(x_0)} = 2g(x)\delta(x - x_0) \tag{10.30}$$

$$\frac{\partial s'(x)}{\partial g(x_0)} = \frac{\partial \delta(x - x_0)}{\partial x} \tag{10.31}$$

$$\frac{\partial F[g(x)]}{\partial g(x_0)} = \frac{\partial F[x]}{\partial x}\delta(x - x_0), \tag{10.32}$$

where $\delta(\cdot)$ is the Dirac Delta function with its nth derivative defined to be

$$\delta^{(n)}(x - x_0) = \frac{(-1)^n n! \delta(x - x_0)}{x^n}. \tag{10.33}$$

10.3.3   Example: Kinematic Equations

To illustrate the power of function optimization, consider a simple physics problem, where a ball is dropped from a height $s(0) = x_0$ with an initial velocity of $s'(0) = v_0$. The question is, what the is position of the ball at time t, or said another way, what is the function $s(t)$? The problem is illustrated in Fig. 10.2.

We know from classical mechanics that the position equation is $s(t) = x_0 - v_0 t - \frac{1}{2}gt^2$, but is also possible to derive this equation by using the principal of least action which states
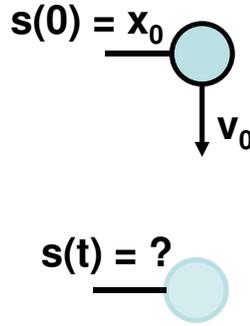
Figure 10.2: Illustration of the ball drop problem.

that the action

$$A = \int_{t_1}^{t_2} K_e(t) + P_e(t)dt \tag{10.34}$$

$$= \int_{t_1}^{t_2} \frac{1}{2}m(s'(\tau))^2 + m\ g\ s(\tau)d\tau, \tag{10.35}$$

where K_e is the kinetic energy and P_e is the potential energy, over any period of time, t_1 to t_2, is minimized by nature.

Without loss of generality, assume $t_1 = 0$. Thus the position equation can be solved by the optimization problem

$$\underset{s(\cdot)}{\text{maximize}} \int_0^t \frac{1}{2}m(s'(\tau))^2 + m\ g\ s(\tau)d\tau \tag{10.36}$$

where the optimal $s(t)$ solves

$$\frac{\partial}{\partial s(\tau_0)} \left[\int_0^t \frac{1}{2}m(s'(\tau))^2 + m\ g\ s(\tau)d\tau \right] = 0. \tag{10.37}$$

Differentiating and redistributing, we have

$$-\int_0^t g\ \delta(\tau - \tau_0)d\tau = \int_0^t (s'(\tau))\frac{\delta'(\tau - \tau_0)}{\tau}d\tau$$

$$-g = \frac{s'(\tau_0)}{\tau_0}$$

By applying the initial velocity constraint we have

$$-g\tau_0 - v_0 = s'(\tau_0), \tag{10.38}$$

140

finally, by applying the initial position constraint, we have

$$s(t) = -\frac{gt^2}{2} - v_0 t + x_0, \tag{10.39}$$

which is exactly the solution we were seeking.

10.4 SNDR Optimization

To optimize the SDNR w.r.t. either $s(\cdot)$ or $g(\cdot)$, we need to solve

$$\frac{\partial}{\partial g(x_0)} SNDR_{x,z}[g(\cdot),\ s(\cdot)] = 0 \tag{10.40}$$

and

$$\frac{\partial}{\partial s(x_0)} SNDR_{x,z}[g(\cdot),\ s(\cdot)] = 0 \tag{10.41}$$

simultaneously. Computing the partial w.r.t. $s(x_0)$, we find

$$\begin{aligned}
\frac{\partial}{\partial s(x_0)} SNDR_{x,z}[g(\cdot),\ s(\cdot)] &= \frac{\partial}{\partial s(x_0)} \frac{|E[zx^*]|^2}{\sigma_x^2 E[|z|^2] - |E[zx^*]|^2} \\
&= \frac{\frac{\partial N}{\partial s(x_o)} D - \frac{\partial D}{\partial s(x_o)} N}{\left(\sigma_x^2 E[|z|^2] - |E[zx^*]|^2\right)^2}, \tag{10.42}
\end{aligned}$$

where N and D are the numerator and denominator of the SNDR expression, respectively. To solve (10.41), we need the numerator of (10.42) to be zero. Assuming real variables, and simplifying, we have

$$\begin{aligned}
\frac{\partial N}{\partial s(x_o)} D &= \frac{\partial D}{\partial s(x_o)} N \\
\frac{\partial N}{\partial s(x_o)} D &= \left(\sigma_x^2 \frac{\partial E[z^2]}{\partial s(x_o)} - \frac{\partial N}{\partial s(x_o)}\right) N \\
\frac{\partial N}{\partial s(x_o)} (D - N) &= \sigma_x^2 \frac{\partial E[z^2]}{\partial s(x_o)} N \\
2E[xz] \frac{\partial E[xz]}{\partial s(x_o)} \left(\sigma_x^2 E[z^2]\right) &= \sigma_x^2 \frac{\partial E[z^2]}{\partial s(x_o)} E[xz]^2 \\
2 \frac{\partial E[xz]}{\partial s(x_o)} E[z^2] &= \frac{\partial E[z^2]}{\partial s(x_o)} E[xz].
\end{aligned}$$

This same simplification holds for the partial w.r.t. $g(x_o)$.

Finally, it is necessary to solve for $\frac{\partial E[xz]}{\partial s(x_o)}$, $\frac{\partial E[xz]}{\partial g(x_o)}$, $\frac{\partial E[z^2]}{\partial s(x_o)}$, and $\frac{\partial E[z^2]}{\partial s(x_o)}$, which are

$$\begin{aligned}
\frac{\partial E[xz]}{\partial s(x_o)} &= \int_{-\infty}^{\infty} \int_{-\infty}^{\infty} x\delta(g(x) + v - x_o) f_x(x) f_v(v) dx\ dv \\
&= \int_{x_o - \mathcal{R}_g} g^{-1}(x_o - v) f_x(g^{-1}(x_o - v)) f_v(v) dv, \tag{10.43}
\end{aligned}$$

141

where $\mathcal{R}_g$ is the set of values in the range of $g(x) \ \forall \ x \in \mathbb{R}$,

$$
\begin{aligned}
\frac{\partial E[z^2]}{\partial s(x_o)} &= \int_{-\infty}^{\infty} \int_{-\infty}^{\infty} 2s(g(x) + v)\delta(g(x) + v - x_o)f_x(x)f_v(v)dx \ dv \\
&= 2s(x_o) \int_{x_o - \mathcal{R}_g} f_x(g^{-1}(x_o - v))f_v(v)dv,
\end{aligned}
\tag{10.44}
$$

$$
\begin{aligned}
\frac{\partial E[xz]}{\partial g(x_o)} &= \int_{-\infty}^{\infty} \int_{-\infty}^{\infty} s'(g(x) + v)\delta(x - x_o)f_x(x)f_v(v)dx \ dv \\
&= \int_{-\infty}^{\infty} s'(g(x_o) + v)f_x(x_o)f_v(v)dv,
\end{aligned}
\tag{10.45}
$$

and

$$
\begin{aligned}
\frac{\partial E[z^2]}{\partial g(x_o)} &= \int_{-\infty}^{\infty} \int_{-\infty}^{\infty} 2s(g(x) + v)s'(g(x) + v)\delta(x - x_o)f_x(x)f_v(v)dx \ dv \\
&= 2\int_{-\infty}^{\infty} s(g(x) + v)s'(g(x_o) + v)f_x(x_o)f_v(v)dv.
\end{aligned}
\tag{10.46}
$$

From here, it is difficult to further simplify the problem without using particular examples.

10.4.1   Example: Uniform Noise, Signal, Clipping Transmitter

As an example, let us assume that both the noise and the signal are uniformly distributed and that the transmitter is a soft limiter with gain of one. That is

$$
x \ \sim \ U[-u_x, u_x]
\tag{10.47}
$$

$$
v \ \sim \ U[-u_v, u_v]
\tag{10.48}
$$

$$
u_x \ \geq \ 1
\tag{10.49}
$$

$$
g(x) \ = \ \begin{cases} -1, & x < -1 \\ x, & |x| \leq 1 \\ 1, & x > 1 \end{cases}
\tag{10.50}
$$

Now, we can compute

$$
\begin{aligned}
\frac{\partial E[xz]}{\partial s(x_o)} &= \frac{1}{4u_x u_v} \int_{-u_v}^{u_v} \int_{-u_x}^{u_x} x\delta(g(x) + v - x_o)U_x(x)U_v(v)dx \ dv \\
&= \frac{1}{4u_x u_v} \int_{-u_v}^{u_v} g^{-1}(x_o - v)U_x(g^{-1}(x_o - v))U_v(v)dv
\end{aligned}
\tag{10.51}
$$

where

$$
U_x(x) = \begin{cases} 1, & x \in [-u_x, u_x] \\ 0, & else \end{cases}
\tag{10.52}
$$

142

and $U_v(v)$ is similarly defined. Next, calculate

$$q_{xz}(x_o) \triangleq \int_{-u_v}^{u_v} g^{-1}(x_o - v)U_x(g^{-1}(x_o - v))U_v(v)dv \tag{10.53}$$

$$= \begin{cases} \int_{-u_v}^{x_o+1} x_o - vdv = \frac{1}{2}(-1 + u_v^2 + 2u_v x_o + x_o^2), \\ \qquad x_o \in [-u_v - 1, -u_v + 1) \bigcup u_v \geq 1 = \mathcal{S}_1 \\ \int_{x_o-1}^{x_o+1} x_o - vdv = 0, \\ \qquad x_o \in [-u_v + 1, u_v - 1) \bigcup u_v \geq 1 = \mathcal{S}_2 \\ \int_{x_o-1}^{u_v} x_o - vdv = \frac{1}{2}(1 - u_v^2 + 2u_v x_o + x_o^2), \\ \qquad x_o \in [u_v - 1, u_v + 1) \bigcup u_v \geq 1 = \mathcal{S}_3 \\ \int_{-u_v}^{x_o+1} x_o - vdv = \frac{1}{2}(-1 + u_v^2 + 2u_v x_o + x_o^2), \\ \qquad x_o \in [-u_v - 1, u_v - 1) \bigcup u_v < 1 = \mathcal{S}_4 \\ \int_{-uv}^{uv} x_o - vdv = 2u_v x_o, \\ \qquad x_o \in [u_v - 1, -u_v + 1) \bigcup u_v < 1 = \mathcal{S}_5 \\ \int_{x_o-1}^{u_v} x_o - vdv = \frac{1}{2}(1 - u_v^2 + 2u_v x_o + x_o^2), \\ \qquad x_o \in [-u_v + 1, u_v + 1) \bigcup u_v < 1 = \mathcal{S}_6. \end{cases} \tag{10.54}$$

The partial w.r.t. $s(x_o)$ is

$$\begin{aligned} \frac{\partial E[z^2]}{\partial s(x_o)} &= \frac{1}{4u_x u_v} \int_{-u_v}^{u_v} \int_{-u_x}^{u_x} 2s(g(x) + v)\delta(g(x) + v - x_o)U_x(x)U_v(v)dx \; dv \\ &= \frac{2}{4u_x u_v} \int_{-u_v}^{u_v} s(x_o)U_x(g^{-1}(x_o - v))U_v(v)dv \\ &= \frac{2s(x_o)}{4u_x u_v} \int_{-u_v}^{u_v} U_x(g^{-1}(x_o - v))U_v(v)dv, \end{aligned} \tag{10.55}$$

where

$$q_{zz}(x_o) \triangleq \int_{-u_v}^{u_v} U_x(g^{-1}(x_o - v))U_v(v)dv \tag{10.56}$$

$$= \begin{cases} \int_{-u_v}^{x_o+1} dv = x_o + 1 + u_v, & (u_v, x_o) \in \mathcal{S}_1 \\ \int_{x_o-1}^{x_o+1} dv = 2, & (u_v, x_o) \in \mathcal{S}_2 \\ \int_{x_o-1}^{u_v} dv = -x_o + 1 + u_v, & (u_v, x_o) \in \mathcal{S}_3 \\ \int_{-u_v}^{x_o+1} dv = x_o + 1 + u_v, & (u_v, x_o) \in \mathcal{S}_4 \\ \int_{-uv}^{uv} dv = 2u_v, & (u_v, x_o) \in \mathcal{S}_5 \\ \int_{x_o-1}^{u_v} dv = -x_o + 1 + u_v, & (u_v, x_o) \in \mathcal{S}_6. \end{cases} \tag{10.57}$$

We need

$$2\frac{\partial E[xz]}{\partial s(x_o)}E[z^2] \;=\; \frac{\partial E[z^2]}{\partial s(x_o)}E[xz]. \tag{10.58}$$

So

$$2\frac{1}{4u_xu_v}q_{xz}(x_o)E[z^2] \;=\; \frac{2s(x_o)}{4u_xu_v}q_{zz}(x_o)E[xz]$$

$$\frac{q_{xz}(x_o)}{q_{zz}(x_o)}\frac{E[z^2]}{E[xz]} \;=\; s(x_o). \tag{10.59}$$

where

$$\frac{q_{xz}(x_o)}{q_{zz}(x_o)} = \begin{cases} \frac{1}{2}(-1+u_v+x_o), & (u_v,x_o)\in\mathcal{S}_1 \\[4pt] 0, & (u_v,x_o)\in\mathcal{S}_2 \\[4pt] \frac{1}{2}(1-u_v+x_o), & (u_v,x_o)\in\mathcal{S}_3 \\[4pt] \frac{1}{2}(-1+u_v+x_o), & (u_v,x_o)\in\mathcal{S}_4 \\[4pt] x_o, & (u_v,x_o)\in\mathcal{S}_5 \\[4pt] \frac{1}{2}(1-u_v+x_o), & (u_v,x_o)\in\mathcal{S}_6, \end{cases} \tag{10.60}$$

Now, it is necessary to find some way to make (10.59) hold. One way may be to introduce variable multiplier so that

$$s(x_o) = a\frac{q_{xz}(x_o)}{q_{zz}(x_o)} \tag{10.61}$$

then find the a that satisfies (10.59). Fortunately, $\frac{E[z^2]}{E[xz]}$ is a constant w.r.t. x_o and the SNDR is scale invariant w.r.t. $s(\cdot)$, so it is not necessary to determine a. Thus, the SNDR-maximizing $s(\cdot)$ among all possible functions for the constraints in (10.63)-(10.65) is simply given (10.60). That is,

$$s(x_o) = \frac{q_{xz}(x_o)}{q_{zz}(x_o)}. \tag{10.62}$$

Interestingly, the optimal function has no dependence on u_x. This is because one of the constraints was that $u_x \geq 1$, which necessitates some clipping. For the case when $u_x < 1$, the transmitter appears linear and the optimal receiver is simply linear.

Optimal Functions Fig. 10.3 is a plot of the optimal functions $s(x)$ for different values of u_v. The plot shows several interesting features. The first is that when the $u_v > 1$ which is the maximum output of $g(x)$, the optimal receiver function actually zeros out part of the

144
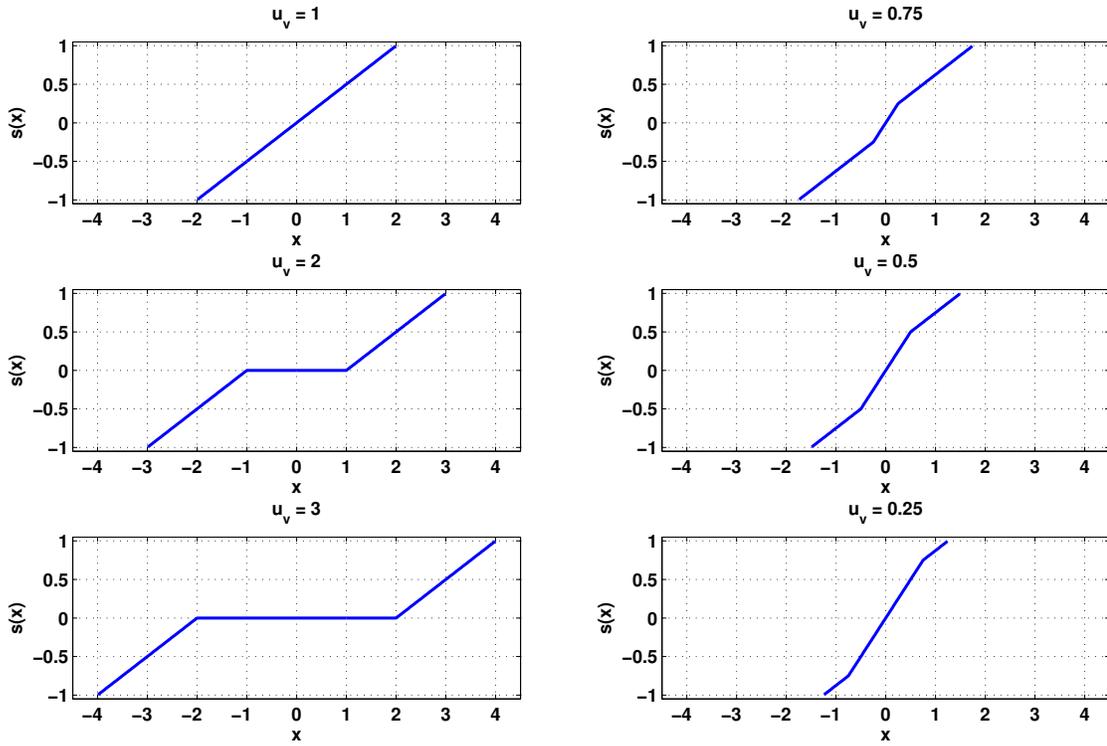
Figure 10.3: Optimal receiver functions for different noise distribution supports.

received signal. The second is that when $u_v < 1$, the optimal receiver is a piecewise function with different slopes in for different input values.

SNDR Results In Fig. 10.4 is a plot of the SNDR of the proposed $s(\cdot)$ in (10.62) and the SNDR of a linear receiver. We can see that most of the difference occurs in the high noise regime, which is intuitive as this is where the optimal receiver differs the most from the linear receiver.
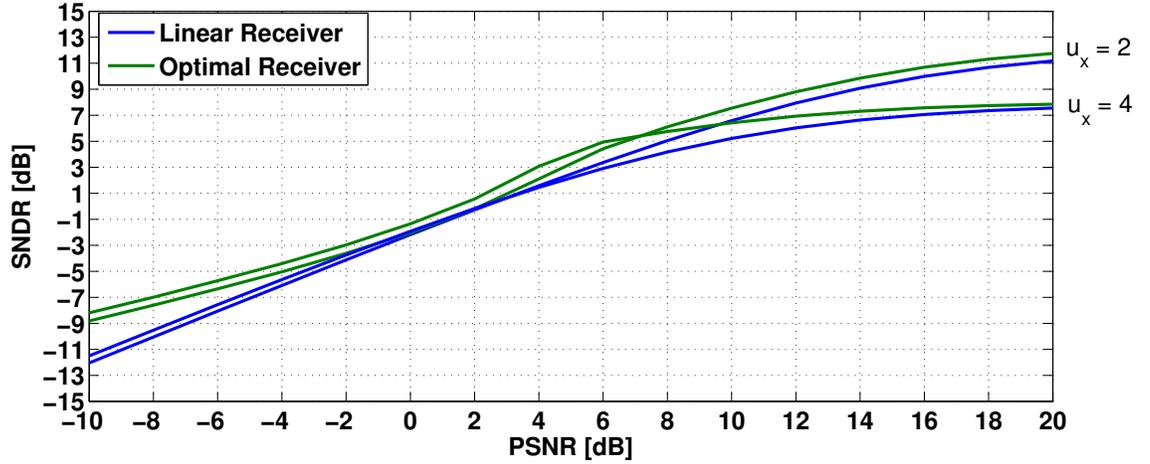
Figure 10.4: SNDR of for a linear receiver and for the proposed SNDR-optimal receiver.

10.4.2 Example: Gaussian Noise, Signal, Clipping Transmitter

For the second example, assume that both the noise and the signal are Gaussian distributed and that the transmitter is a soft limiter with gain of one. That is

$$x \quad \sim \quad N[0, \sigma_x^2] \tag{10.63}$$

$$v \quad \sim \quad N[0, \sigma_v^2] \tag{10.64}$$

$$g(x) \quad = \quad \begin{cases} -1, & x < -1 \\ x, & |x| \leq 1 \\ 1, & x > 1 \end{cases} \tag{10.65}$$

After integration of (10.45), we find that

$$
\begin{aligned}
\frac{\partial E[xz]}{\partial s(x_o)} = {} & \frac{1}{2\left(\sigma_v^2 + \sigma_x^2\right)^{3/2}} e^{-\frac{1}{2\sigma_x^2} - \frac{1 + x_o + x_o^2}{\sigma_v^2}} \sigma_v \sigma_x^2 \Bigg(-2 e^{\frac{1 + x_o^2}{2\sigma_v^2}} \left(-1 + e^{\frac{2x_o}{\sigma_v^2}} \right) \sigma_v \sqrt{\sigma_v^2 + \sigma_x^2} \\
& + e^{\frac{\sigma_v^4 + 2\sigma_x^4\left(1 + x_o + x_o^2\right) + \sigma_v^2 \sigma_x^2 \left(3 + 2x_o + x_o^2\right)}{2\sigma_v^2 \sigma_x^2 \left(\sigma_v^2 + \sigma_x^2\right)}} \sqrt{2\pi} \sigma_x x_o \mathrm{Erf}\left[\frac{\sigma_v^2 - \sigma_x^2(-1 + x_o)}{\sqrt{2}\sigma_v \sigma_x \sqrt{\sigma_v^2 + \sigma_x^2}} \right] \\
& + e^{\frac{\sigma_v^4 + 2\sigma_x^4\left(1 + x_o + x_o^2\right) + \sigma_v^2 \sigma_x^2 \left(3 + 2x_o + x_o^2\right)}{2\sigma_v^2 \sigma_x^2 \left(\sigma_v^2 + \sigma_x^2\right)}} \sqrt{2\pi} \sigma_x x_o \mathrm{Erf}\left[\frac{\sigma_v^2 + \sigma_x^2(1 + x_o)}{\sqrt{2}\sigma_v \sigma_x \sqrt{\sigma_v^2 + \sigma_x^2}} \right] \Bigg). \tag{10.66}
\end{aligned}
$$

Computing (10.46) for this example gives

$$
\frac{\partial E[z^2]}{\partial s(x_o)} = \frac{e^{-\frac{x_o^2}{2(\sigma_v^2 + \sigma_x^2)}} \sqrt{\frac{\pi}{2}} \sigma_v \sigma_x}{\sqrt{\sigma_v^2 + \sigma_x^2}} \left(\mathrm{Erf}\left[\frac{\sigma_v^2 - \sigma_x^2(-1 + x_o)}{\sqrt{2}\sigma_v \sigma_x \sqrt{\sigma_v^2 + \sigma_x^2}} \right] + \mathrm{Erf}\left[\frac{\sigma_v^2 + \sigma_x^2(1 + x_o)}{\sqrt{2}\sigma_v \sigma_x \sqrt{\sigma_v^2 + \sigma_x^2}} \right] \right).
$$
$$\tag{10.67}$$

146
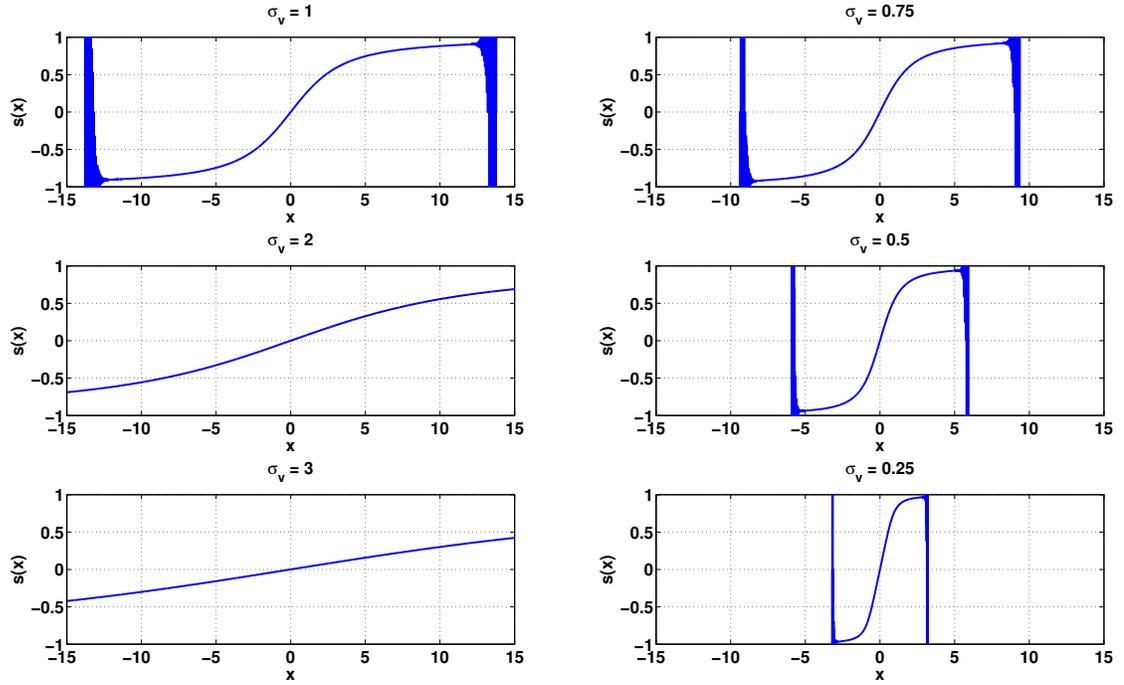
Figure 10.5: Optimal receiver functions for different noise variances, where $\sigma_x = 1$.

Again, the term $\frac{E[z^2]}{E[xz]}$ in (10.59) is constant w.r.t. x_o so it does not need to be calculated. Thus,

$$s(x_o) = \frac{\partial E[xz]}{\partial s(x_o)} \Big/ \frac{\partial E[z^2]}{\partial s(x_o)}. \tag{10.68}$$

Optimal Functions Fig. 10.5 is a plot of the optimal functions $s(x)$ for different values of σ_v. The plot shows that the optimal function for different noise powers has essentially the same shape, just that the support is expanded. At the edges of the functions there are some values that are not well defined. This is because $s(x_o) \to 0/0$ at the edges which leads to numerical instability for finite precision programs. It is not clear what the values would converge to in practice but they appear to be asymptotically approaching one.

SNDR Results In Fig. 10.6 is a plot of the SNDR of the proposed $s(\cdot)$ in (10.68) and the SNDR of a linear receiver. Most of the difference occurs for PSNR values from 0dB to 15dB.
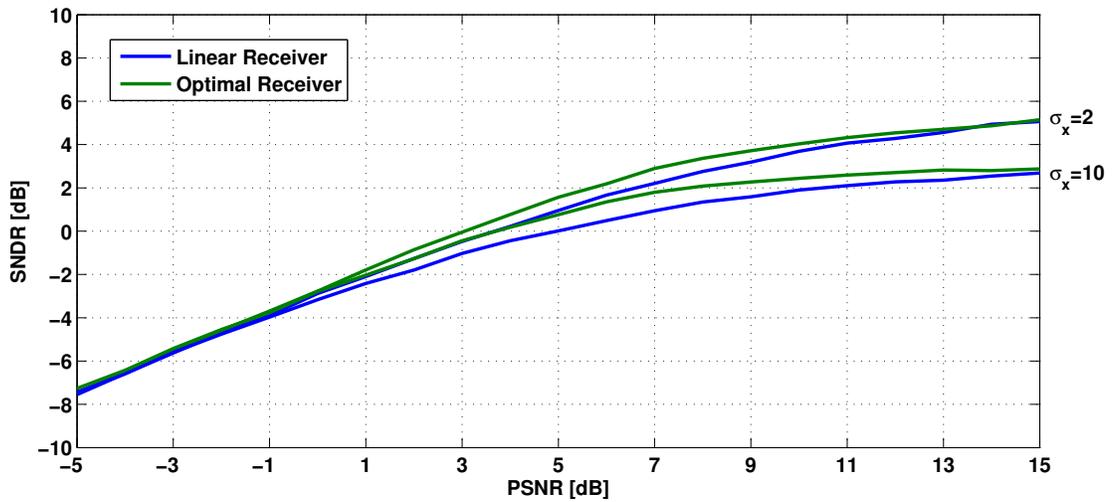
Figure 10.6: SNDR of for a linear receiver and for the proposed SNDR-optimal receiver.

10.5   Conclusions

In this chapter we have outlined a method for determining the optimal transmitter and receiver function pairs in additive noise channels. To verify the result, we used an example where the transmitter function is a soft clipper and found the optimal receiver function when both the noise and signal are uniformly distributed. In this example, we found that several dBs of SNDR improvement are possible. In the future it will be of interest to expand this work in three possible directions i) solve for other practical examples where the noise takes on different distributions; ii) reformulate the result for complex functions and variables; iii) jointly solve for both the Tx and Rx functions.

CHAPTER XI

CONTRIBUTIONS

In this thesis we have given an overview of the problem of transmitting multicarrier signals through peak-limited channels. As part of the overview we have identified and solved several problems in peak-limited communications. The research results are summarized in the following list:

- It was established that the sample-wise SNDR and the block-wise SNDR are similar for the most common operating environments (moderate noise levels, $N \geq 128$).

- It was demonstrated how SLM can be modified for SNDR maximization.

- The computational complexity of a pruned FFT for PTS was derived.

- With the pruned FFT complexity analysis, it was demonstrated that SLM outperforms PTS per unit of complexity in virtually all operating environments.

- The low-complexity magnitude-SLM scheme was proposed and justified for certain operating environments.

- A projection on to convex sets method for generating low-PAR JSPSs with desirable correlation properties was demonstrated.

- A JSPS-SLM algorithm was derived that allows for synergistic synchronization, channel estimation, PAR reduction and phase sequence detection.

- The pilot placement for null subcarrier OFDM systems was determined. The proposed placement algorithm achieve near optimal symbol-estimate MSE and allows for a significant improvement over existing evenly-spaced pilot placement schemes.

- A formulation for the optimal transmitter-receiver function pair was presented.

Several publications have resulted from work contained in or related to this thesis. Below is a comprehensive list of this work:

11.1 Journal

[J1] C. Zhao, R. J. Baxley and G. T. Zhou, "Peak-to-average power ratio and power efficiency considerations in MIMO-OFDM systems," *IEEE Communications Letters*, vol. 12, no. 4, pp. 268–270, April, 2008.

[J2] R. J. Baxley and G. T. Zhou, "Comparing selected mapping and partial transmit sequence for PAR reduction," *IEEE Transactions on Broadcasting*, vol. 53, no. 4, pp. 797–803, December 2007.

[J3] R. J. Baxley, C. Zhao, and G. T. Zhou, "Constrained clipping for crest factor reduction in OFDM," *IEEE Transactions on Broadcasting*, vol. 52, no. 4, pp. 570–575, December 2006.

[J4] R. J. Baxley and G. T. Zhou, "MAP metric for blind phase sequence detection in selected mapping," *IEEE Transactions on Broadcasting*, vol. 51, no. 4, pp. 565–570, December 2005.

[J5] R. J. Baxley and G. T. Zhou, "Power savings analysis of peak-to-average power ratio in OFDM," *IEEE Transactions on Consumer Electronics*, vol. 50, no. 3, pp. 792–798, August 2004.

[J6] R. J. Baxley, J. E. Kleider, and G. T. Zhou, "Pilot design for OFDM with null edge subcarriers," accepted subject to revisions in *IEEE Transactions on Wireless Communications*, January 2008.

11.2 Conference

[C1] J. Kleider, X. Ma, R. Baxley, and G.T. Zhou, "MISO joint synchronization-pilot design for OFDM systems," *Proc. IEEE Intl. Conference on Acoustics, Speech, and Signal Processing*, Las Vegas, NV, March 2008.

[C2] Q. Liu, R. J. Baxley, and G. T. Zhou, "Free subcarrier optimization for peak-to-average power ratio minimization in OFDM systems," *Proc. IEEE Intl. Conference on Acoustics, Speech, and Signal Processing*, Las Vegas, NV, March 2008.

[C3] Q. Liu, R. J. Baxley, X. Ma and G. T. Zhou, "EVM optimization for OFDM systems with deterministic constraint on the peak-to-average power ratio," *Proc. 42nd Conference on Information Sciences and Systems*, Princeton, NJ, March 2008.

[C4] R. J. Baxley, J. E. Kleider and G. T. Zhou, "A method for joint peak-to-average power ratio reduction and synchronization in OFDM," *Proc. IEEE MILCOM Conference*, Orlando, FL, October 2007.

[C5] R. J. Baxley and G. T. Zhou, "SNDR considerations for the minimum clipping power loss scheme," *Proc. IEEE MILCOM Conference*, Orlando, FL, October 2007.

[C6] C. Zhao, R. J. Baxley, and G. T. Zhou, "SNDR analysis for transceiver nonlinearities in AWGN Channels," *Proc. IEEE Statistical Signal Processing Workshop*, pp. 522-526, Madison, WI, August 2007.

[C7] R. J. Baxley and G. T. Zhou, "A comparison of SNDR maximization techniques for OFDM," *Proc. IEEE Statistical Signal Processing Workshop*, pp. 423-427, Madison, WI, August 2007.

[C8] R. J. Baxley, J. Kleider and G. T. Zhou, "Pilot design for IEEE 802.16 OFDM and OFDMA", Proc. *IEEE Intl. Conference on Acoustics, Speech, and Signal Processing*, pp. 321-324, Honolulu, Hawaii, April 2007.

[C9] R. J. Baxley, C. Zhao and G. T. Zhou, "Magnitude-scaled selected mapping: A crest factor reduction scheme for OFDM without side-information transmission," *Proc. IEEE Intl. Conference on Acoustics, Speech, and Signal Processing*, pp. 373-376, Honolulu, Hawaii, April 2007.

[C10] C. Zhao, R. J. Baxley, G. T. Zhou, D. Boppana, and J. S. Kenney, "Constrained clipping for crest factor reduction in multiple-user OFDM," *Proc. IEEE Radio and*

Wireless Symposium, pp. 341-344, Long Beach, CA, January 2007.

[C11] C. Zhao and R. J. Baxley, "Error vector magnitude analysis for OFDM systems," in *Proc. IEEE Asilomar Conference*, pp. 1830-1834, Pacific Grove, CA, October 2006.

[C12] X. Ma, R. J. Baxley, J. Kleider, and G. T. Zhou, "Superimposed training for channel shortening equalization in OFDM," *Proc. IEEE MILCOM Conference*, Washington, D.C., October 2006.

[C13] R. J. Baxley and G. T. Zhou, "Comparison of selected mapping and partial transmit sequence for crest factor reduction in OFDM," *Proc. IEEE MILCOM Conference*, Washington, D.C., October 2006.

[C14] R. J. Baxley and G. T. Zhou, "Computational complexity analysis of FFT pruning - A Markov modeling approach," *Proc. IEEE 12th Digital Signal Processing Workshop*, pp. 535-539, Grand Teton National Park, WY, September 2006.

[C15] R. J. Baxley, J. Kleider, "Embedded synchronization/pilot sequence creation using POCS," *Proc. IEEE Intl. Conference on Acoustics, Speech, and Signal Processing*, pp. 321-324, Toulouse, France, May 2006.

[C16] R. J. Baxley and G. T. Zhou, "Ordered phase sequence testing in SLM for improved blind detection," *Proc. IEEE Workshop on Signal Processing Advances in Wireless Communications*, pp. 274-277, New York City, NY, June 2005.

[C17] R. J. Baxley and G. T. Zhou, "Assessing peak-to-average power ratios for communications applications," *Proc. IEEE MILCOM Conference*, pp. 181-185, Monterey, CA, October 2004.

[C18] G. T. Zhou, R. J. Baxley, and N. Chen, "Selected mapping with monomial phase rotations for peak-to-average power ratio reduction in OFDM," *Proc. IEEE Intl. Conf. on Communications, Circuits, and Systems*, pp. 66-70, Chengdu, China, June 2004.

11.3 Patents

[P1] R. J. Baxley and J. E. Kleider, "Means and method for generation of communication codes possessing excellent synchronization, peak-to-average ratio, and channel estimation properties," US Utility Patent Application, 2007.

[P2] J. E. Kleider and R. J. Baxley, "Means and method for joint synchronization, peak-to-average ratio reduction, and channel estimation in multi-carrier transmission," US Utility Patent Application, 2007.

[P3] R. J. Baxley, J. E. Kleider and K. Anderson, "Means and method for robust multi-carrier communication system in harsh non-linearly amplified and time-varying multipath channels," US Utility Patent Application, 2007.

[P4] C. Zhao, R. J. Baxley, and G. T. Zhou, "A clipping technique for OFDM with in-band EVM control and out-of-band spectrum shaping," US Utility Patent Application, 2006.

REFERENCES

[1] "IEEE Standard for Local and Metropolitan Area Networks Part 16: Air Interface for Fixed Broadband Wireless Access Systems," *IEEE Std 802.16-2004 (Revision of IEEE Std 802.16-2001)*, pp. 1–857, 2004.

[2] ADIREDDY, S., TONG, L., and VISWANATHAN, H., "Optimal placement of training for frequency-selective block-fading channels," *IEEE Transactions on Information Theory*, vol. 48, pp. 2338–2353, August 2002.

[3] AGGARWAL, A. and MENG, T. H., "Minimizing the peak-to-average power ratio of OFDM signals using convex optimization," *IEEE Transactions on Signal Processing*, vol. 54, pp. 3099–3110, August 2006.

[4] ALAVI, A., TELLAMBURA, C., and FAIR, I., "PAPR reduction of OFDM signals using partial transmit sequence: an optimal approach using sphere decoding," *IEEE Communications Letters*, vol. 9, pp. 982–984, November 2005.

[5] ARMSTRONG, J., "Analysis of new and existing methods of reducing intercarrier interference due to carrier frequency offset in OFDM," *IEEE Transactions on Communications*, vol. 47, pp. 365–369, March 1999.

[6] BAEK, M.-S., KIM, M.-J., YOU, Y.-H., and SONG, H.-K., "Semi-blind channel estimation and PAR reduction for MIMO-OFDM system with multiple antennas," *IEEE Transactions on Broadcasting*, vol. 50, pp. 414–424, December 2004.

[7] BAUML, R. W., FISCHER, R. F. H., and HUBER, J. B., "Reducing the peak-to-average power ratio of multicarrier modulationby selected mapping," *Electronics Letters*, vol. 32, pp. 2056–2057, October 1996.

[8] BAXLEY, R. J., "Analyzing selected mapping for peak-to-average power reduction in ofdm," Master's thesis, Georgia Institute of Technology, May 2005.

[9] BAXLEY, R. J. and KLEIDER, J. E., "Embedded synchronization/pilot sequence creation using POCS," in *Proc. IEEE International Conference on Acoustics, Speech and Signal Processing, 2006.*, pp. 321–324, May 2006.

[10] BAXLEY, R. J., KLEIDER, J. E., and ZHOU, G. T., "A method for joint peak-to-average power ratio reduction and synchronization in ofdm," in *Proc. IEEE Military Communications Conference*, October 2007.

[11] BAXLEY, R. J., KLEIDER, J. E., and ZHOU, G. T., "Pilot design for IEEE 802.16 OFDM and OFDMA," in *Proc. IEEE Intl. Conference on Acoustics, Speech and Signal Processing*, vol. 2, (Honolulu, HI), April 2007.

[12] BAXLEY, R. J. and TONG ZHOU, G., "Computational complexity analysis of FFT pruning - a markov modeling approach," in *Proc. IEEE Digital Signal Processing Workshop*, (Teton National Park, WY, USA), pp. 535–539, September 2006.

154

[13] BAXLEY, R. J., ZHAO, C., and ZHOU, G. T., "Magnitude-scaled selected mapping: A crest factor reduction scheme for OFDM without side-information transmission," in *Proc. IEEE Intl. Conference on Acoustics, Speech and Signal Processing*, vol. 3, (Honolulu, HI), April 2007.

[14] BAXLEY, R. J. and ZHOU, G. T., "Assessing peak-to-average power ratios for communications applications," in *Proc. IEEE Military Communications Conference*, pp. 181–185, October 2004.

[15] BAXLEY, R. J. and ZHOU, G. T., "MAP metric for blind phase sequence detection in selected mapping," *IEEE Transactions on Broadcasting*, vol. 51, pp. 565–570, December 2005.

[16] BAXLEY, R. J. and ZHOU, G. T., "Ordered phase sequence testing in SLM for improved blind detection," in *Proc. IEEE 6th Workshop on Signal Processing Advances in Wireless Communications*, pp. 256–259, June 2005.

[17] BAXLEY, R. J. and ZHOU, G. T., "Comparison of selected mapping and partial transmit sequence for crest factor reduction in OFDM," in *Proc. IEEE Military Communications Conference*, October 2006.

[18] BAXLEY, R. J. and ZHOU, G. T., "Comparing selected mapping and partial transmit sequence for PAR reduction," *IEEE Transactions on Broadcasting*, vol. 53, pp. 797–803, December 2007.

[19] BAXLEY, R. J. and ZHOU, G. T., "A comparison of SNDR maximization techniques for OFDM," in *Proc. IEEE Workshop on Statistical Signal Processing*, (Madison, WI, USA), pp. 423–427, August 2007.

[20] BAXLEY, R. J. and ZHOU, G. T., "Sndr considerations for the minimum clipping power loss," in *Proc. IEEE Military Communications Conference*, October 2007.

[21] BOYD, S. and VANDENBERGHE, L., *Convex Optimization*. Cambridge University Press, 2004.

[22] BRILLINGER, D., *Time Series Data Analysis and Theory*. Philadelphia, PA: SIAM, 2001.

[23] BUDIANU, C. and TONG, L., "Channel estimation for space-time orthogonal block codes," *IEEE Transactions on Signal Processing*, vol. 50, pp. 2515–2528, October 2002.

[24] CAI, X. and GIANNAKIS, G. B., "Error probability minimizing pilots for OFDM with m-PSK modulation over rayleigh-fading channels," *IEEE Transactions on Vehicular Technology*, vol. 53, pp. 146–155, January 2004.

[25] CAVERS, J. K., "An analysis of pilot symbol assisted modulation for rayleigh fading channels," *IEEE Transactions on Vehicular Technology*, vol. 40, pp. 686–693, November 1991.

[26] CHANG, R. W., "Synthesis of band-limited orthogonal signals for multichannel data transmission," *Bell Syst. Tech. J.*, vol. 45, pp. 1775–1796, December 1966.

[27] Chang, R. W., "Orthogonal frequency division multiplexing." U.S. Patent 3 488 445, January 1970.

[28] Chen, N. and Zhou, G. T., "Peak-to-average power ratio reduction in OFDM with blind selected pilot tone modulation," *IEEE Transactions on Wireless Communications*, vol. 5, pp. 2210–2216, August 2006.

[29] Chen, N. and Zhou, G. T., "Superimposed training for OFDM: a peak-to-average power ratio analysis," *IEEE Transactions on Signal Processing*, vol. 54, pp. 2277–2287, June 2006.

[30] Cimini, L. J. and Sollenberger, N. R., "Peak-to-average power ratio reduction of an OFDM signal using partial transmit sequences," in *Proc. IEEE International Conference on Communications*, vol. 1, (Vancouver, BC), pp. 511–515, June 1999.

[31] Combettes, F. L., "The foundations of set theoretic estimation," *Proceedings of the IEEE*, vol. 81, pp. 182–208, February 1993.

[32] Cooley, J. W. and Tukey, J. W., "An algorithm for the machine calculation of complex fourier series," *Mathematics of Computation*, vol. 19, pp. 297–301, April 1965.

[33] Cripps, S. C., *RF Power Amplifiers for Wireless Communications*. Norwood, MA: Artech House, 1999.

[34] Dardari, D., Tralli, V., and Vaccari, A., "A theoretical characterization of nonlinear distortion effects in OFDM systems," *IEEE Trans. on Commun.*, vol. 48, no. 10, pp. 1755–1764, 2000.

[35] Dinur, N. and Wulich, D., "Peak-to-average power ratio in high-order OFDM," *IEEE Transaction on Communications*, vol. 49, pp. 1063–1072, June 2001.

[36] Dogancay, K., "Blind compensation of nonlinear distortion for bandlimited signals," *IEEE Transactions on Circuits and Syst. I: Regular Papers*, vol. 52, no. 9, pp. 1872–1882, 2005.

[37] Dong, M. and Tong, L., "Optimal design and placement of pilot symbols for channel estimation," *IEEE Transactions on Signal Processing*, vol. 50, pp. 3055–3069, December 2002.

[38] Dong, M., Tong, L., and Sadler, B. M., "Optimal pilot placement for channel tracking in OFDM," in *Proc. IEEE Military Communications Conference*, pp. 602–606, October 2002.

[39] Edfors, O., Sandell, M., van de Beek, J. J., Wilson, S. K., and Borjesson, P. O., "OFDM channel estimation by singular value decomposition," *IEEE Transactions on Communications*, vol. 46, pp. 931–939, July 1998.

[40] Eun, C. and Powers, E. J., "A new volterra predistorter based on the indirect learning architecture," *IEEE Transactions on Signal Processing*, vol. 45, pp. 223–227, January 1997.

[41] GELFAND, I. M. and FOMIN, S. V., *Calculus of Variations*. Dover Publications, 2000.

[42] GRANT, M. and BOYD, S., "Cvx: Matlab software for disciplined convex programming (web page and software)." http://stanford.edu/ boyd/cvx, March 2008.

[43] HAN, S. H. and LEE, J. H., "Modified selected mapping technique for PAPR reduction of coded OFDM signal," *IEEE Transactions on Broadcasting*, vol. 50, pp. 335–341, September 2004.

[44] HAN, S. H. and LEE, J. H., "An overview of peak-to-average power ratio reduction techniques for multicarrier transmission," *IEEE Wireless Communications*, vol. 12, pp. 56–65, April 2005.

[45] HAYKIN, S., "Cognitive radio: brain-empowered wireless communications," *IEEE Journal on Selected Areas in Communications*, vol. 23, pp. 201–220, February 2005.

[46] HIEU, N. T., KIOM, S.-W., and RYU, H.-G., "PAPR reduction of the low complexity phase weighting method in OFDM communication system," *IEEE Transactions on Consumer Electronics*, vol. 51, pp. 776–782, August 2005.

[47] HO, W. S., MADHUKUMAR, A. S., and CHIN, F., "Peak-to-average power reduction using partial transmit sequences: a suboptimal approach based on dual layered phase sequencing," *IEEE Transactions on Broadcasting*, vol. 49, pp. 225–231, June 2003.

[48] HOEHER, P. and TUFVESSON, F., "Channel estimation with superimposed pilot sequence," in *Proc. IEEE Global Telecommunications Conference*, vol. 4, (Rio de Janeireo), pp. 2162–2166, 1999.

[49] HU, Z. and WAN, H., "A novel generic fast fourier transform pruning technique and complexity analysis," *IEEE Transactions on Signal Processing*, vol. 53, pp. 274–282, January 2005.

[50] HUANG, X., LU, J., ZHENG, J., LETAIEF, K. B., and GU, J., "Companding transform for reduction in peak-to-average power ratio of OFDM signals," *IEEE Transactions on Wireless Communications*, vol. 3, pp. 2030–2039, November 2004.

[51] JAYALATH, A. D. S. and TELLAMBURA, C., "SLM and PTS peak-power reduction of OFDM signals without side information," *IEEE Transactions on Wireless Communications*, vol. 4, pp. 2006–2013, September 2005.

[52] JIANG, T., YANG, Y., and SONG, Y.-H., "Exponential companding technique for PAPR reduction in OFDM systems," *IEEE Transactions on Broadcasting*, vol. 51, pp. 244–248, June 2005.

[53] KANG, S. G., KIM, J. G., and JOO, E. K., "A novel subblock partition scheme for partial transmit sequence OFDM," *IEEE Transactions on Broadcasting*, vol. 45, pp. 333–338, September 1999.

[54] KAY, S. M., *Fundamentals of Statistical Signal Processing, Volume I: Estimation Theory*. Englewood Cliffs, NJ: Prentice-Hall, 1993.

[55] KIM, D. and STUBER, G. L., "Clipping noise mitigation for OFDM by decision-aided reconstruction," *IEEE Communications Letters*, vol. 3, pp. 4–6, January 1999.

[56] KLEIDER, J. E., MAALOULI, G., GIFFORD, S., and CHUPRUN, S., "Preamble and embedded synchronization for RF carrier frequency-hopped OFDM," *IEEE Journal on Selected Areas in Communications*, vol. 23, no. 5, pp. 920–931, 2005.

[57] KWON, O.-J. and HA, Y.-H., "Multi-carrier PAP reduction method using sub-optimal PTS with threshold," *IEEE Transactions on Broadcasting*, vol. 49, pp. 232–236, June 2003.

[58] LARSSON, E. G. and LI, J., "Preamble design for multiple-antenna OFDM-based WLANs with nullsubcarriers," *IEEE Signal Processing Letters*, vol. 8, pp. 285–288, November 2001.

[59] LEI, X., TANG, Y., LI, S., and LI, Y.-T., "A minimum clipping power loss scheme for mitigating the clipping noise in OFDM," in *Proc. IEEE Global Telecommunications Conference*, vol. 1, pp. 6–9, December 2003.

[60] LI, X. and CIMINI, L. J., "Effects of clipping and filtering on the performance of OFDM," *IEEE Communications Letters*, vol. 2, pp. 131–133, May 1998.

[61] LI, Y., CIMINI, L. J., and SOLLENBERGER, N. R., "Robust channel estimation for OFDM systems with rapid dispersive fading channels," *IEEE Transactions on Communications*, vol. 46, pp. 902–915, July 1998.

[62] LIM, D.-W., HEO, S.-J., NO, J.-S., and CHUNG, H., "A new PTS OFDM scheme with low complexity for PAPR reduction," *IEEE Transactions on Broadcasting*, vol. 52, pp. 77–82, March 2006.

[63] LO, H., LEE, D., and GANSMAN, J. A., "A study of non-uniform pilot spacing for PSAM," in *Proc. IEEE International Conference on Communications*, vol. 1, (New Orleans, LA), pp. 322–325, June 2000.

[64] LU, Q., GUI, L., and FANG, X. Z., "A new scheme to mitigate the OFDM high PAR problem by minimizing the signal's nonlinear distortion caused by HPA," *IEEE Transactions on Broadcasting*, vol. 52, pp. 576–578, December 2006.

[65] MA, X., GIANNAKIS, G. B., and OHNO, S., "Optimal training for block transmissions over doubly-selective fading channels," in *Proc. IEEE International Conference on Acoustics, Speech, and Signal Processing*, vol. 2, (Orlando, FL), pp. 1509–1512, 2002.

[66] MA, X., YANG, L., and GIANNAKIS, G. B., "Optimal training for MIMO frequency-selective fading channels," *IEEE Transactions on Wireless Communications*, vol. 4, pp. 453–466, March 2005.

[67] MAAS, S. A., *Nonlinear Microwave Circuits*. IEEE Press, 1997.

[68] MARKEL, J., "FFT pruning," *IEEE Transactions on Audio and Electroacoustics*, vol. 19, pp. 305–311, December 1971.

[69] MCKELLIPS, A. L., "Simple tight bounds on capacity for the peak-limited discrete-time channel," in *Proc. International Symposium on Information Theory*, (Chicago, IL), p. 348, 2004.

[70] MEHLFÜHRER, C. and RUPP, M., "Approximation and resampling of tapped delay line channel models with guaranteed channel properties," in *Proc. IEEE Intl. Conference on Acoustics, Speech and Signal Processing*, April 2008.

[71] MESTDAGH, D. J. G., SPRUYT, P., and BIRAN, B., "Analysis of clipping effect in DMT-based ADSL systems," in *Proc. IEEE International Conference on Communications*, (New Orleans, LA), pp. 293–300, May 1994.

[72] MOOSE, P. H., "A technique for orthogonal frequency division multiplexing frequency offset correction," *IEEE Transactions on Communications*, vol. 42, pp. 2908–2914, October 1994.

[73] MORELLI, M. and MENGALI, U., "A comparison of pilot-aided channel estimation methods for OFDM systems," *IEEE Transactions on Signal Processing*, vol. 49, pp. 3065–3073, December 2001.

[74] MUHONEN, K. J., KAVEHRAD, M., and KRISHNAMOORTHY, R., "Look-up table techniques for adaptive digital predistortion: a development and comparison," *IEEE Transactions on Vehicular Technology*, vol. 49, pp. 1995–2002, September 2000.

[75] MULLER, S. H. and HUBER, J. B., "A comparison of peak power reduction schemes for OFDM," in *Proc. IEEE Global Telecommunications Conference*, vol. 1, (Phoenix, AZ), pp. 1–5, November 1997.

[76] MULLER, S. H. and HUBER, J. B., "OFDM with reduced peak-to-average power ratio by optimum combination of partial transmit sequences," *Electronics Letters*, vol. 33, pp. 368–369, February 1997.

[77] NAGAI, K., "Pruning the decimation-in-time FFT algorithm with frequency shift," *IEEE Transactions on Acoustics, Speech, and Signal Processing*, vol. 34, pp. 1008–1010, August 1986.

[78] NEGI, R. and CIOFFI, J. M., "Pilot tone selection for channel estimation in a mobile OFDM system," *IEEE Transactions on Consumer Electronics*, vol. 44, pp. 1122–1128, August 1998.

[79] OCHIAI, H., "Performance analysis of peak power and band-limited OFDM system with linear scaling," *IEEE Transactions on Wireless Communications*, vol. 2, pp. 1055–1065, September 2003.

[80] OCHIAI, H. and IMAI, H., "Performance of the deliberate clipping with adaptive symbol selection for strictly band-limited OFDM systems," *IEEE Journal on Selected Areas in Communications*, vol. 18, pp. 2270–2277, November 2000.

[81] OCHIAI, H. and IMAI, H., "On the distribution of the peak-to-average power ratio in OFDM signals," *IEEE Transactions on Communications*, vol. 49, pp. 282–289, February 2001.

[82] OCHIAI, H. and IMAI, H., "Performance analysis of deliberately clipped OFDM signals," *IEEE Transactions on Communications*, vol. 50, pp. 89–101, January 2002.

[83] O'Hara, S., Chen, B., and Periard, J., "A bandwidth efficient peak power reduction scheme for multicarrier modulation using selected mapping," in *Proc. Conference on Information Sciences and Systems*, March 2003.

[84] Ohno, S., "Preamble and pilot symbol design for channel estimation in OFDM," in *IEEE International Conference on Acoustics, Speech and Signal Processing*, vol. 3, (Honolulu, HI), April 2007.

[85] Ohno, S. and Giannakis, G. B., "Optimal training and redundant precoding for block transmissions with application to wireless OFDM," *IEEE Transactions on Communications*, vol. 50, pp. 2113–2123, December 2002.

[86] Palomar, D. P., Cioffi, J. M., and Lagunas, M. A., "Joint tx-rx beamforming design for multicarrier MIMO channels: a unified framework for convex optimization," *IEEE Transactions on Signal Processing*, vol. 51, pp. 2381–2401, September 2003.

[87] Pollet, T., Bladel, M. V., and Moenaclaey, M., "BER sensitivity of OFDM systems to carrier frequency offset and wiener phase noise," *IEEE Transactions on Communications*, vol. 43, pp. 191–192, February 1995.

[88] Proakis, J. G., *Digital Communications*. New York, NY: McGraw-Hill, 2001.

[89] Qian, H., Raich, R., and Zhou, G. T., "On the benefits of deliberately introduced baseband nonlinearities in communication systems," *IEEE International Conference on Acoustics, Speech, and Signal Processing*, vol. 2, pp. 905–8, May 2004.

[90] Raich, R., *Nonlinear System Identification and Analysis with Applications to Power Amplifier Modeling and Power Amplifier Predistortion*. PhD thesis, Georgia Institute of Technology, May 2004.

[91] Raich, R., Qian, H., and Zhou, G. T., "Orthogonal polynomials for power amplifier modeling and predistorter design," *IEEE Transactions on Vehicular Technology*, vol. 53, pp. 1468–1479, September 2004.

[92] Raich, R., Qian, H., and Zhou, G. T., "Optimization of SNDR for amplitude limited nonlinearities," *IEEE Transaction on Communications*, vol. 53, pp. 1964–1972, November 2005.

[93] Rangarajan, S. R. and Srinivasan, S., "Generalised method for pruning an FFT type of transform," *IEE Proceedings-Vision, Image and Signal Processing*, vol. 144, pp. 189–192, August 1997.

[94] Roche, C., "A split-radix partial input/output fast fourier transform algorithm," *IEEE Transactions on Signal Processing*, vol. 40, pp. 1273–1276, May 1992.

[95] Rodrigues, M. R. D. and Wassell, I. J., "A novel coding strategy to improve the error probability performance of non-linearly distorted ofdm signals," in *Proc. IEEE Vehicular Technology Conference*, vol. 1, pp. 294–298, October 2003.

[96] Rodrigues, M. R. D. and Wassell, I. J., "SLM and PTS based on an IMD reduction strategy to improve the error probability performance of non-linearly distorted ofdm signals," in *Proc. IEEE Int. Conf. Communications*, vol. 2, pp. 857–861, June 2004.

[97] RODRIGUES, M. R. D. and WASSELL, I. J., "IMD reduction with SLM and PTS to improve the error-probability performance of nonlinearly distorted OFDM signals," *IEEE Transactions on Vehicular Technology*, vol. 55, pp. 537–548, March 2006.

[98] RUSSELL, M. and STUBER, G. L., "Interchannel interference analysis of OFDM in a mobile environment," *Proc. IEEE Vehicular Technology Conference*, pp. 820–824, July 1995.

[99] RYU, H.-G. and YOUN, K.-J., "A new PAPR reduction scheme: SPW (subblock phase weighting)," *IEEE Transactions on Consumer Electronics*, vol. 48, pp. 81–89, February 2002.

[100] SANZI, F. and SPEIDEL, J., "An adaptive two-dimensional channel estimator for wireless OFDM with application to mobile DVB-t," *IEEE Transactions on Broadcasting*, vol. 46, pp. 128–133, June 2000.

[101] SARI, H., KARAM, G., and JEANCLAUDE, I., "Transmission techniques for digital terrestrial TV broadcasting," *IEEE Communications Magazine*, vol. 33, pp. 100–109, February 1995.

[102] SCHMIDL, T. M. and COX, D. C., "Robust frequency and timing synchronization for OFDM," *IEEE Transactions on Communications*, vol. 45, pp. 1613–1621, December 1997.

[103] SHAMAI, S. and BAR-DAVID, I., "The capacity of average and peak-power-limited quadrature gaussianchannels," *IEEE Transactions on Information Theory*, vol. 41, pp. 1060–1071, July 1995.

[104] SHANNON, C. E., "A mathematical theory of communication," *Bell Sys. Tech. J.*, vol. 27, pp. 379–423, 6, 1948.

[105] SMITH, J. G., "The information capacity of amplitudeand variance-constrained scalar gaussian channels," *Inform. Contr.*, vol. 18, p. 203219, 1971.

[106] SORENSEN, H. V. and BURRUS, C. S., "Efficient computation of the DFT with only a subset of input or output points," *IEEE Transactions on Signal Processing*, vol. 41, pp. 1184–1200, March 1993.

[107] SREENIVAS, T. and RAO, P., "FFT algorithm for both input and output pruning," *IEEE Transactions on Acoustics, Speech, and Signal Processing*, vol. 27, pp. 291–292, June 1979.

[108] TAN, J. and STUBER, G. L., "Anti-jamming performance of multi-carrier spread spectrum with constant envelope," in *Proc. IEEE International Conference on Communications*, vol. 1, pp. 743–747, May 2003.

[109] TELLADO, J., *Multicarrier Modulation With Low PAR: Applications to DSL and Wireless*. Kluwer Academic Publishers, 2000.

[110] TONG, L., SADLER, B. M., and DONG, M., "Pilot-assisted wireless transmissions: general model, design criteria, and signal processing," *IEEE Signal Processing Magazine*, vol. 21, pp. 12–25, November 2004.

[111] TSIMBINOS, J. and LEVER, K. V., "Nonlinear system compensation based on orthogonal polynomial inverses," *IEEE Trans. on Circuits and Syst. I: Fundamental Theory and Applications*, vol. 48, no. 4, pp. 406–417, 2001.

[112] TUFVESSON, F., EDFORS, O., and FAULKNER, M., "Time and frequency synchronization for OFDM using PN-sequence preambles," in *Proc. IEEE Vehicular Technology Conference*, (Amsterdam, Netherlands), pp. 2203–2207, September 1999.

[113] VAN DE BEEK, J. J., EDFORS, O., SANDELL, M., WILSON, S. K., and BORJESSON, P. O., "On channel estimation in OFDM systems," in *Proc. IEEE Vehicular Technology Conference*, vol. 2, (Chicago, IL), pp. 815–819, July 1995.

[114] VAN NEE, R. D. J. and DE WILD, A., "Reducing the peak-to-average power ratio of OFDM," *Proc. IEEE Vehicular Technology Conference*, vol. 3, pp. 2072–2076, 1998.

[115] WANG, C.-L. and OUYANG, Y., "Low-complexity selected mapping schemes for peak-to-average power ratio reduction in OFDM systems," *IEEE Transactions on Signal Processing*, vol. 53, pp. 4652–4660, December 2005.

[116] WANG, X., TJHUNG, T. T., and WU, Y., "On the SER and spectral analyses of A-law companded multicarrier modulation," *IEEE Trans. on Veh. Techn.*, vol. 52, pp. 1408–1412, Sept. 2003.

[117] WANG, X., TJHUNG, T. T., and NG, C. S., "Reduction of peak-to-average power ratio of OFDM system using a companding technique," *IEEE Transactions on Broadcasting*, vol. 45, pp. 303–307, September 1999.

[118] WANG, Z. and GIANNAKIS, G. B., "Wireless multicarrier communications," *IEEE Signal Processing Magazine*, vol. 17, pp. 29–48, May 2000.

[119] WEINSTEIN, S. B. and EBERT, P. M., "Data transmission by frequency division multiplexing using the discrete fourier transform," *IEEE Trans. Comm. Technology*, vol. COM-19, pp. 282–289, October 1971.

[120] YANG, B., CAO, Z., and LETAIEF, K. B., "Analysis of low-complexity windowed DFT-based MMSE channel estimator for OFDM systems," *IEEE Transactions on Communications*, vol. 49, pp. 1977–1987, November 2001.

[121] YANG, L., CHEN, R. S., SIU, Y. M., and SOO, K. K., "PAPR reduction of an OFDM signal by use of PTS with low computational complexity," *IEEE Transactions on Broadcasting*, vol. 52, pp. 83–86, March 2006.

[122] YEH, Y.-H. and CHEN, S.-G., "DCT-based channel estimation for OFDM systems," in *Proc. IEEE International Conference on Communications*, vol. 4, pp. 2442–2446, June 2004.

[123] YOU, Y.-H., JEON, W.-G., PAIK, J.-H., and SONG, H.-K., "A simple construction of OFDM-CDMA signals with low peak-to-average power ratio," *IEEE Transactions on Broadcasting*, vol. 49, pp. 403–407, December 2003.

[124] ZHANG, Q., HAN, B. W., CHO, J. H., and WEI, S., "PAPR performance of IDFT-based uncoded OFDM signals with null subcarriers and transmit filtering," in *Proc.*

IEEE International Conference on Communications, vol. 10, (Istanbul), pp. 4636–4641, June 2006.

[125] ZHAO, C., *Distortion-Based Crest Factor Reduction Algorithms In Multi-Carrier Transmission Systems*. PhD thesis, Georgia Institute of Technology, December 2007.

[126] ZHIGLJAVSKY, A. A., *Theory of Global Random Search*. Kluwer Academic Publishers, 1991.

[127] ZHOU, G. T., "Peak-to-average power ratio reduction in OFDM: blind selected mapping for PSK inputs," in *Proc. IEEE International Conference on Acoustics, Speech and Signal Processing, 2006.*, pp. 293–296, 2006.

[128] ZHOU, G. T. and PENG, L., "Optimality condition for selected mapping in OFDM," *IEEE Transactions on Signal Processing*, vol. 54, pp. 3159–3165, August 2006.

[129] ZOU, W. Y. and WU, Y., "COFDM: An overview," *IEEE Transaction on Broadcasting*, vol. 41, pp. 1–8, March 1995.

VITA

Robert J. Baxley was born in Marietta, GA on September 1, 1982. In 2000 he started a B.S. in electrical engineering at the Georgia Institute of Technology, which he completed with highest honors in 2003. He completed his M.S. in electrical engineering from the same institution in 2005 winning the Sigma Xi Best Thesis award. Since 2005 he has been working towards the completion of his Ph.D. in electrical engineering with the support of the National Science Foundation Graduate Research Fellowship.